

Copyright
by
Seungnam Kim
2017

The Thesis Committee for Seungnam Kim

Certifies that this is the approved version of the following thesis:

**An Improved Full Wake Alignment Scheme for the Prediction of
Open/Ducted Propeller Performance in Steady and Unsteady Flow**

APPROVED BY

SUPERVISING COMMITTEE:

Spyridon A. Kinnas: Supervisor

Ben Hodges

**An Improved Full Wake Alignment Scheme for the Prediction of
Open/Ducted Propeller Performance in Steady and Unsteady Flow**

By

Seungnam Kim

THESIS

Presented to the Faculty of the Graduate School of
The University of Texas at Austin
in Partial Fulfillment
of the Requirements
for the Degree of

MASTER OF SCIENCE IN ENGINEERING

THE UNIVERSITY OF TEXAS AT AUSTIN
August 2017

“How long, Lord? Will you forget me forever?
How long will you hide your face from me?

How long must I wrestle with my thoughts
and day after day have sorrow in my heart?
How long will my enemy triumph over me?

Look on me and answer, Lord my God.
Give light to my eyes, or I will sleep in death,
and my enemy will say, ‘I have overcome him,’
and my foes will rejoice when I fall.

But I trust in your unfailing love;
my heart rejoices in your salvation.

I will sing the Lord’s praise,
for he has been good to me.”
(Psalm 13:1-6)

Dedicated to
my Lord and my family

Acknowledgements

I would like to express my sincere thanks to Prof. S. A. Kinnas for his enduring assistance and encouragement during my graduate study. He threw a fire in a young engineer's mind from South Korea to have a dream of becoming a global leader in the shipbuilding and offshore industry. He also has never let me forget the importance of delivering what is in an engineer's mind in very clear English.

I would also like to thank Prof. Ben Hodges for reading my thesis. I truly believe his comments on my thesis would become invaluable nutrition in my future research.

I would also like to thank the members of Ocean Engineering Group (OEG) for their endless help, warm companionship, and daily humors that have given me great energy to keep myself activated. I would especially thank Mr. Yiran Su for his priceless teaching on every Friday after the weekly group meeting. He has not hesitated to answer my questions on our daily research.

I would like to express my sincere appreciation to my brothers, Mr. Weikang Du, Chunlin Wu, and Zhihao Li. We have studied together, shared our opinions on research during lunch time together, played together, and most importantly we have got frustrated together at the unexpected research findings. They have definitely lightened up some pages in my life. Also, I want to thank Ms. Yunjun Wu and Ms. Xing Lu. Thanks to my warm people in Austin Korean Presbyterian Church for their love. I cannot imagine my life here in Austin without thinking of the days I shared my Lord's love with them.

This work was supported by the U.S. Office of Naval Research (Contract N00014-14-1-0303) and Phase VII of the "Consortium on Cavitation Performance of High Speed Propulsors" with the following current members: Kawasaki Heavy Industry Ltd., Rolls-Royce Marine AB,

Rolls-Royce Marine AS, SSPA AB, Andritz Hydro GmbH, Wärtsilä Netherlands B.V., Wärtsilä Norway AS, Wärtsilä CME Zhenjiang Propeller Co. Ltd., and Steerprop Ltd.

Abstract

An Improved Full Wake Alignment Scheme for the Prediction of Open/Ducted Propeller Performance in Steady and Unsteady Flow

by

Seungnam Kim, M.S.E.

THE UNIVERSITY OF TEXAS AT AUSTIN 2017

Supervisor: Spyridon A. Kinnas

For a long time, ducted propellers have been a viable alternative of propulsion; due to their higher efficiency at high thrust coefficients, less sensitivity to the ambient flow, and more robust mechanical layout than open propellers. Applications of ducted propellers can be found in many types of ships and offshore structures.

This thesis introduces several improvements on the wake alignment model in the panel method to predict the performance of ducted and open propellers. The full wake alignment, which aligns wake panels based on the local flow velocity, is improved with an emphasis on the consideration of general incoming flow. Previously, the full wake alignment model is restricted to the case in uniform inflow and now is extended to be able to handle non-uniform and non-axisymmetric inflow. Proper ways of improving the numerical algorithm in the full wake alignment scheme are investigated.

Wake alignment model for the ducted propeller is studied and improved with an emphasis on the duct paneling. In this thesis, two repaneling options on the duct and duct wake panels are introduced to improve the predicted propeller performance. Also, efforts have been given to the control points on the non-planar panels on the duct inner surface to predict the performance at lower advance ratios.

The full wake alignment is also applied to duct wake to represent the behavior of trailing vorticity after the trailing edge of the duct. The wake sheet representing the trailing vortex of the duct is improved by aligning it with the local flow velocity as in the case of the blade wake.

Correlations among the predicted results from the panel method and other methods, i.e. full-blown Reynolds Averaged Navier-Stokes (RANS) simulations, vortex lattice method (VLM), and experiments are presented.

Table of Contents

Acknowledgements.....	v
Abstract.....	vii
Table of Contents.....	ix
List of Figures.....	xii
List of Tables.....	xxi
Nomenclature.....	xxii
Latin Symbols.....	xxii
Greek Symbols.....	xxiii
Acronyms.....	xxiii
Computer Program Names.....	xxiv
Chapter 1 Introduction.....	1
1.1 Background.....	1
1.2 Objective.....	4
1.3 Overview.....	5
Chapter 2 Lower Order Panel Method for Hydrofoil and Propeller Problem.....	7
2.1 Two-Dimensional Inviscid Formulation.....	7
2.2 Numerical Implementation.....	13
2.3 Three-Dimensional Inviscid Formulation.....	14

Chapter 3 Full Wake Alignment	19
3.1 Steady Wake Alignment.....	19
3.1.1 Previous Research.....	19
3.1.2 Basic Idea.....	20
3.1.3 Alignment Algorithm.....	24
3.1.4 Inflow Consideration	30
3.2 Repaneling of the Duct and the Duct Wake.....	32
3.2.1 Algorithm.....	33
3.2.2 The Two Repaneling Options	33
3.2.3 Treatment of Control Point on the Duct Panel.....	37
3.2.4 Effect of Panel Adaptation on Loading Distribution over Blade.....	43
3.3 Duct Wake Alignment.....	47
3.3.1 Introduction.....	48
3.3.2 Algorithm.....	49
3.3.3 Numerical Results.....	53
3.4 Unsteady Wake Alignment	55
3.4.1 Introduction.....	55
3.4.2 Basic Algorithm	56
Chapter 4 Application to Ducted Propeller.....	70
4.1 Ducted Propeller with Square Blade Tip and Sharp Trailing Edge Duct.....	70

4.1.1	Lower Order Panel Method	71
4.1.2	Full Blown RANS Simulation	80
4.1.3	Correlations.....	82
Chapter 5 Application to Open Propeller.....		98
5.1	Steady Wake Alignment.....	99
5.1.1	Uniform Inflow	99
5.1.2	Non-uniform Inflow	110
5.2	Unsteady Wake Alignment	119
5.2.1	Uniform Inflow	119
5.2.2	Inclined Shaft Flow.....	122
Chapter 6 Conclusions and Recommendations.....		132
6.1	Conclusions	132
6.2	Recommendations	134
Bibliography		136
Vita.....		141

List of Figures

Figure 2.1 Hydrofoil in uniform flow.	8
Figure 2.2 Hydrofoil and trailing edge wake in uniform flow stream. $n +$ and t are the coordinates normal and tangential to the wake sheet respectively.....	10
Figure 2.3 Paneling of a 3-D blade and wake.	15
Figure 3.1 Key wake with local velocity vectors plotted on each nodal point of the wake	21
Figure 3.2 Open propeller with helical wake aligned with the uniform inflow.....	21
Figure 3.3 Helical inflow wake and the two components of the perturbation velocity, $u_{i,s}$ and $u_{i,n}$, induced along and normal to the inflow direction.	24
Figure 3.4 Schematic plot of a material line before (y_{in}) and after ($y_{in} + 1$) alignment in a pseudo unsteady alignment approach (note that the same denotation is used for the mean velocity in Figure 3.5).	25
Figure 3.5 Schematic plot of a vortex line before (X_{in}) and after ($X_{in} + 1$) alignment using FWA.	28
Figure 3.6 Flowchart of the iterative algorithm constructed in FWA scheme.....	29
Figure 3.7 Fully aligned wake panels using FWA in (a) uniform and (b, c) non-uniform inflow.	31
Figure 3.8 KA4-70 ducted propeller geometry (upper) and the duct cross section shape (lower).	32
Figure 3.9 Flow chart of FWA with duct and duct wake repaneling options.	34
Figure 3.10 Blade/duct wake from the first (left) and second (right) iteration in FWA with repaneling Option 1. Red circles clearly show duct and duct wake are not adapted to the blade	

wake in the second iteration. KA4-70 ducted propeller is used at the design advance ratio, $J_s=0.50$.
..... 35

Figure 3.11 Blade/duct wake from the first (left) and second (right) iteration in FWA with repaneling Option 2. Red circles clearly show duct and duct wake are adapted to the blade wake in the second iteration. KA4-70 ducted propeller is used at the design advance ratio, $J_s=0.50$... 35

Figure 3.12 ducted propeller attached to an offshore structure [32] which keeps its position in the ocean with the help of the ducted propeller and dynamic positioning system (DPS) [33]..... 37

Figure 3.13 Non-planar panels with contour (left)/without contour (right). Control points (red circle) are not on the same plane as the panel corners (blue circles). 38

Figure 3.14 Planar panels with contour (left)/without contour (right). Control points (red circle) are on the same plane as the panel corners (blue circles). 38

Figure 3.15 Wake and duct geometry of KA4-70 ducted propeller in three-dimensional plot (left) and two-dimensional plot (right) at $J_s=(a) 0.30$, (b) 0.50, and (c) 0.70. Duct wake is not presented here..... 40

Figure 3.16 Panel distributions on duct surface. Panels are adapted to the blade wake at $J_s=0.7$ (left), 0.5 (middle), and 0.3 (right). Duct geometries are taken from KA4-70 ducted propeller.. 41

Figure 3.17 Distortion of the wake panels due to the abnormally induced velocity at the low advance ratios..... 42

Figure 3.18 Replacement of the radial locations of the control points by stretching the non-planar panels on the duct..... 43

Figure 3.19 Panel distribution on the ducted propeller with square blade tip. Panels on the duct are adapted (lower) / not adapted (upper) with the blade tip. 45

Figure 3.20 Circulation distribution over the square tip blade with duct panels adapted to blade tip and not adapted to blade tip. KA4-70 ducted propeller is used at the design advance ratio, $J_s=0.50$.
..... 46

Figure 3.21 Geometry of the ducted propeller with cylindrical duct wake. 47

Figure 3.22 Penetration of the blade wake on the duct wake. 48

Figure 3.23 The paneling of the blade wake after resolving the problem of panel penetration. .. 49

Figure 3.24 Flow chart of FWA without duct wake alignment. 50

Figure 3.25 Flow chart of FWA with blade and duct wake alignment. 51

Figure 3.26 Flow chart of duct wake alignment using FWA. 52

Figure 3.27 Convergence history of the full wake alignment scheme applied to both the blade wake and the duct wake (only part of the propeller geometry is shown for clarity) at the (a) 1st, (b) 5th, and (c) last iteration out of 30 loops. Black solid lines on the right column figures mean the concentrated shedding vortex without diffusion effect in the panel method. KA4-70 ducted propeller is used at the design advance ratio, $J_s=0.50$ 54

Figure 3.28 Propeller subject to a general inflow, assumed to be effective wake. (x, y, z) and (x_s, y_s, z_s) denote the propeller fixed and the ship fixed coordinates respectively. This figure is adjusted from Figure 2.19 of [H. Lee 2002]. 57

Figure 3.29 Convection of the trailing wake strength in steady mode ($t = 0$) at the first iteration. Where $\Delta\phi_{w, 12}$ means the trailing wake strength on the 1st layer of the wake sheet from the hub at the 2nd iteration, for example. Different color means different strength. 60

Figure 3.30 Convection of the trailing wake strength in steady mode ($t = 0$) at the second iteration. Where $\Delta\phi_{w, 12}$ means the trailing wake strength on the 1st layer of the wake sheet from the hub at the 2nd iteration, for example. Different color means different strength. 61

Figure 3.31 Convection of the trailing wake strength in steady mode ($t = 0$) at the last iteration. Where $\Delta\phi w, 12$ means the trailing wake strength on the 1st layer of the wake sheet from the hub at the 2nd iteration, for example. Different color means different strength. 62

Figure 3.32 Convection of the trailing wake strength in unsteady mode at time step $t = \delta t$. Where $\Delta\phi w, 1\delta t$ means the trailing wake strength on the 1st layer of the wake sheet from the hub at time step $t = \delta t$, for example. Different color means different strength. 63

Figure 3.33 Convection of the trailing wake strength in unsteady mode at time step $t = 2\delta t$. Where $\Delta\phi w, 1\delta t$ means the trailing wake strength on the 1st layer of the wake sheet from the hub at time step $t = \delta t$, for example. Different color means different strength. 64

Figure 3.34 Convection of the trailing wake strength in unsteady mode at time step $t = 3\delta t$. Where $\Delta\phi w, 1\delta t$ means the trailing wake strength on the 1st layer of the wake sheet from the hub at time step $t = \delta t$, for example. Different color means different strength. 65

Figure 4.1 Convergence study of the predicted blade thrust and torque coefficients with a number of panels on the blade and duct. B(c60s20) and D(c160c'20), for example, represent 60×20 (chordwise×spanwise) panels on blade and 160×20 (chordwise×circumferentially) panels on the duct..... 72

Figure 4.2 Blade and duct wake geometries from FWA at (a) $J_s = 0.3$, (b) $J_s = 0.4$, (c) $J_s = 0.5$, (d) $J_s = 0.6$, and (e) $J_s = 0.7$. 100 panels are used to discretize both the blade wake and the duct wake. KA4-70 ducted propeller is tested..... 74

Figure 4.3 Unit direction vector of vortex segment and the velocity vector that is used to align the vortex segment. The angle between the two vector quantities are denoted as θ 75

Figure 4.4 Convergence of the blade/duct wake using 100 wake panels (streamwise direction) at the first iteration: KA4-70 ducted propeller, $J_s=0.5$, and $\Delta t = 6^\circ$. Velocity vectors are plotted on

the wake panels (upper) with the contour plots of the cross product magnitude, $V_{total, i \times Si}$ (lower). Only parts of wakes are plotted for clarity..... 76

Figure 4.5 Convergence of the blade/duct wake using 100 wake panels (streamwise direction) at the 10th iteration: KA4-70 ducted propeller, $J_s=0.5$, and $\Delta t = 6^\circ$. Velocity vectors are plotted on the wake panels (upper) with the contour plots of the cross product magnitude, $V_{total, i \times Si}$ (lower). Only parts of wakes are plotted for clarity..... 77

Figure 4.6 Convergence of the blade/duct wake using 100 wake panels (streamwise direction) at the 20th iteration: KA4-70 ducted propeller, $J_s=0.5$, and $\Delta t = 6^\circ$. Velocity vectors are plotted on the wake panels (upper) with the contour plots of the cross product magnitude, $V_{total, i \times Si}$ (lower). Only parts of wakes are plotted for clarity..... 78

Figure 4.7 Convergence of the blade/duct wake using 100 wake panels (streamwise direction) at the 30th iteration: KA4-70 ducted propeller, $J_s=0.5$, and $\Delta t = 6^\circ$. Velocity vectors are plotted on the wake panels (upper) with the contour plots of the cross product magnitude, $V_{total, i \times Si}$ (lower). Only parts of wakes are plotted for clarity..... 79

Figure 4.8 Gridding of blade, hub, and duct in RANS simulation (right) and the two-dimensional plane cutting through the propeller geometry with an angle of zero degree (left). 81

Figure 4.9 Schematic view of plotting wake sheet from the panel method on two-dimensional plane, which slices the center of propeller geometry in the $x - y$ direction..... 82

Figure 4.10 Two-dimensional contour plots of KA4-70 ducted propeller and shedding vortex with diffusion for advance ratios of (a) 0.3, (b) 0.4, and (c) 0.5..... 83

Figure 4.11 Correlations of two-dimensional contour plots of the shedding between the results from RANS simulations and panel method (black solid line) for the advance ratios of 0.4. 85

Figure 4.12 Correlations of two-dimensional contour plots of the shedding between the results from RANS simulations and panel method (black solid line) for the advance ratios of 0.5. 86

Figure 4.13 Predicted force performance of KA4-70 ducted propeller from the experiments and panel method. FWA is applied to both the duct/blade wake, but a cylindrical duct wake is assumed when the repaneling options are adopted. 87

Figure 4.14 Circulation distributions of KA4-70 ducted propeller from panel method with FWA on both blade wake and duct wake for the advance ratios from 0.3 to 0.7. Repaneling Option 2 is adopted here. 88

Figure 4.15 Matched (a) and Unmatched (b) panels between the duct inner side and the outer edge of blade wake from Option 1 and 2, respectively. 89

Figure 4.16 Convergence histories of the predicted thrust coefficients on the blade using FWA with the two repaneling options. The horizontal axis indicates the number of iterations in FWA. 90

Figure 4.17 Convergence histories of the predicted torque coefficients on the blade using FWA with the two repaneling options. The horizontal axis indicates the number of iterations in FWA. 91

Figure 4.18 Correlation of the pressure distributions between the results from RANS and panel method at several blade sections. The radial location of each section is indicated in the figure.. 94

Figure 4.19 Description of subdivided parts on duct. Hub geometry is not included in this figure. 95

Figure 4.20 Relative distribution of the blade wake and duct panels. Very close distance between those panels might cause the singular behavior in Option 1 (left) unless they are aligned as in Option 2 (right). 95

Figure 4.21 Correlation of the predicted circumferentially averaged pressure distribution on the duct between panel method (Option 1 and 2), RANS/VLM coupling method, and RANS simulation at $J_s=0.50$	96
Figure 4.22 Description of the strips which are adopted for the pressure plotting on the duct (upper) and the corresponding pressure distributions on each strip from Option 2 (lower left) and Option 1 (lower right).	97
Figure 5.1 Wake geometries aligned using FWA with 60 wake panels in uniform flow: $J_s = 1.14$	100
Figure 5.2 Wake geometries aligned using FWA with 80 wake panels in uniform flow: $J_s = 1.14$	101
Figure 5.3 Wake geometries aligned using FWA with 100 wake panels in uniform flow: $J_s = 1.14$	102
Figure 5. 4 Wake geometries aligned using FWA with 120 wake panels in uniform flow: $J_s = 1.14$	103
Figure 5.5 Wake geometries aligned using FWA with 140 wake panels in uniform flow: $J_s = 1.14$	104
Figure 5.6 Convergence of circulation distribution over blade with number of wake panels for DTMB 4661 propeller: $\Delta t = 6^\circ$ and $J_s = 1.14$, $UR = Vs^2 + (0.7n\pi D)^2$	105
Figure 5.7 Convergence of wake panels at the first iteration in full wake alignment with 80 panels.	106
Figure 5.8 Convergence of wake panels at the second iteration in full wake alignment with 80 panels.	107

Figure 5.9 Convergence of wake panels at the fifth iteration in full wake alignment with 80 panels.	108
Figure 5.10 Convergence of wake panels at the eighth iteration in full wake alignment with 80 panels.	109
Figure 5.11 DTMB 4661 propeller in axisymmetric inflow, which has its highest and lowest velocity at near hub and blade tip, respectively.	111
Figure 5.12 Convergence of wake panels at the second iteration in full wake alignment in axisymmetric inflow. Yellow arrow denotes the total velocity induced on the wake panel.	112
Figure 5.13 Convergence of wake panels at the 13th iteration in full wake alignment in axisymmetric inflow. Yellow arrow denotes the total velocity induced on the wake panel.	113
Figure 5.14 DTMB 4661 propeller in axisymmetric inflow, which has its highest and lowest velocity at the blade tip and near hub, respectively.	114
Figure 5.15 Convergence of wake panels at the second iteration in full wake alignment in axisymmetric inflow. Yellow arrow denotes the total velocity induced on the wake panel.	116
Figure 5.16 Convergence of wake panels at the 19 th iteration in full wake alignment in axisymmetric inflow. Yellow arrow denotes the total velocity induced on the wake panel.	117
Figure 5.17 Circulation distribution over blade using uniform and non-uniform inflow for DTMB 4661 propeller: $\Delta t = 6^\circ$ and $J_s = 1.14$, $UR = Vs^2 + (0.7n\pi D)^2$. Cases I & II correspond to non-uniform inflows as described in the text.	118
Figure 5.18 Circulation distribution on the blade predicted by steady and unsteady mode using DTMB 4661 propeller with 80 wake panels: $\Delta t = 6^\circ$ and $J_s = 1.14$	120
Figure 5.19 Thrust and torque coefficients predicted by steady and unsteady modes using DTMB 4661 propeller with 80 wake panels: $\Delta t = 6^\circ$ and $J_s = 1.14$	121

Figure 5.20 Wake geometry predicted by steady (red) and unsteady (blue) alignment modes using DTMB 4661 propeller with 80 wake panels: $\Delta t = 6^\circ$ and $Js = 1.14$. Only the two wake sheets are presented for clarity in the left figure..... 122

Figure 5.21 Experimental arrangement of 4661 propeller in inclined shaft flow, taken from Figure 5 of [Boswell et al. 1984]..... 123

Figure 5.22 Modeling of hub vortex cavitation, taken from Figure 5.1 of [H. Lee 2002]. 124

Figure 5.23 The projected view of aligned wake geometries for DTMB 4661 propeller with (a) Hub 5, (b) Hub 4, (c) Hub 2, and (d) Hub 1: $Js = 1.14$ and $\alpha = 10^\circ$ 126

Figure 5.24 Convergence of the predicted steady thrust and torque coefficients using DTMB 4661 propeller with number of wake panels for four different hub geometries: $\Delta t = 6^\circ$ and $Js = 1.14$.
..... 128

Figure 5.25 Unsteady and mean thrust and torque coefficients using DTMB 4661 propeller using four different hub geometries: $\Delta t = 6^\circ$ and $Js = 1.0$ 129

Figure 5.26 The first harmonic of the forces and moments acting on one blade for DTMB 4661 propeller. 131

List of Tables

Table 4.1 Parameter settings in RANS simulations and the computational time, adjusted from Table 4.1 of [H. Fan 2015].....	81
---	----

Nomenclature

Latin Symbols

C_f	Skin friction coefficient $C_f = \tau_{wall}/(0.5\rho U^2)$
C_p	Pressure coefficient $C_p = (P - P_0)/(0.5\rho n^2 D^4)$
D	Propeller diameter
G	Green's function
J	Advance ratio based on V_s , $J = V_s/(nD)$
K_Q	Torque Coefficient, $K_Q = Q/(\rho n^2 D^5)$
K_{TD}	Thrust coefficient due to the duct, $K_{TD} = T_D/(\rho n^2 D^4)$
K_{TP}	Thrust coefficient due to the blades, $K_{TP} = T_P/(\rho n^2 D^4)$
n	Propeller rotational frequency
Q	Torque on the propeller
R	Propeller radius
S_B	Body surface
S_W	Wake surface
T_D	Thrust on the duct
T_P	Thrust on the blades
u	Perturbation velocity
U_{in}	Local inflow velocity
V_s	Ship speed

Greek Symbols

α	Angle of attack
Γ	Circulation on blade sections
Δt	Time step size
ρ	Fluid density
ν	Fluid kinematic viscosity
ϕ	Perturbation potential
ϕ^{inv}	Inviscid perturbation potential
ϕ_{total}	Total potential
ω	Propeller angular velocity

Acronyms

2-D	Two dimensional
3-D	Three dimensional
BEM	Boundary element method
CFD	Computational fluid dynamics
CPU	Central processing unit
RANS	Reynolds-averaged Navier-Stokes
VLM	Vortex-lattice method

Computer Program Names

- PROPCAV A cavitating propeller potential flow solver based on BEM
- FLUENT A commercial RANS solver provided by ANSYS
- MPUF-3A A VLM based code for solving flow around propellers

Chapter 1

Introduction

1.1 Background

From Archimedes, who thought of the screw propellers, to the modern shipbuilding and offshore industries, propeller has been a primary propulsion system for vehicles interacting with fluid. People are living in the world where it is almost impossible to think of ships without propellers.

As a viable alternative of propulsion system, ducted propeller, which surrounds blades with a non-rotating nozzle, has been widely used in and out of the shipbuilding and offshore industries in modern days. Ducted propeller can produce higher efficiency than open propellers, particularly at high loading conditions and therefore is used on heavily loaded propellers or propellers with limited diameter. In the offshore industry, ducted propellers are highly important to keep the position of the floating offshore structures with the help of the dynamic positioning system (DPS) and azimuthal pods. Considering those mechanical structures use ducted propeller as their primary propulsion source to be stationary at a certain location in the ocean, predicting the accurate performance of the ducted propellers becomes crucial even at the design stage of those structures. The sturdy structure from the harsh circumstance of the ocean makes ducted propeller even more suitable as a primary propulsion system.

Prediction of the accurate performance of propellers has been of the greatest interest among engineering community related to the propulsion system. As the most popular numerical tool in the field of computational fluid dynamics (CFD), full-blown Reynolds Averaged Navier-Stokes

(RANS) simulation has been widely used to analyze the flow around propellers. Despite its relatively stable and accurate prediction of 3-D geometries involving propellers, RANS simulation turned out to be too expensive in terms of the computation time. Generating mesh grid even before starting the calculation requires lots of efforts, making RANS less viable in the early stage of propeller design.

On the other hand, panel methods can be a proper alternative numerical tool to RANS. Panel methods are often called Boundary Element Method (BEM) or Boundary Integral Method (BIM). BEM solves for the unknown quantities (velocities, deformations) on the *boundary* of the domain. Quantities inside the domain are determined in terms of the quantities on the boundary in BEM, while Finite Element Methods (FEM) or Finite Volume Method (FVM) melt in RANS discretizes the whole domain and solves for unknown quantities (velocity, deformations) defined at each cell or element. Compared to FVM or FEM, BEM is more versatile in that it is much easier to discretize the boundary than the whole domain. Also, BEM is much faster by using fewer panels, which means fewer unknowns are going to be solved.

Historically, many kinds of panel methods have been proposed since the surface source method by [Hess et al. 1964]. Later, [Hess et al. 1985] applied the surface source method to the marine propeller problem. However, when the thickness of the blade becomes small, the surface source method was not successful. [Koyama et al. 1986] applied a Morino type low order panel method to the marine propeller, however pressure distribution near the trailing edge of blade was excessively predicted due to the failure of Morino's Kutta condition. [J. Lee 1987] applied a pressure Kutta condition in an iterative way to satisfy the Kutta condition on 3-D trailing edge flow in steady state. He also carried out extensive reviews on the characteristics of the various panel methods. As a result, a low order panel method based on the perturbation potential turned

out to be robust and reliable with smaller computational effort. The Kutta condition was further investigated by [Kinnas and Hsin 1992] in unsteady flow around extreme propeller geometries by considering the convection of the trailing wake strength along the wake surface. More recently, panel method was extended to ducted propeller by [H. Fan 2015]. He applied the perturbation potential based lower order panel method to ducted propellers. [Kinnas et al. 2016] further improved the panel method for ducted propeller with an emphasis on the duct paneling and the wake alignment model.

Wake alignment model for the wake sheets behind the trailing edge of the blade or duct needs to be carefully taken into consideration for the accurate prediction of propeller performance in the panel method. The importance of wake alignment model is more addressed in the ducted propeller case due to very close distance between the outer edge of wake sheets and duct inner surface. Even for open propeller, the predicted loading on blade differs depending on the wake alignment model that the panel method uses, making wake alignment model as an attractive research topic. There have been lots of efforts on wake alignment model to predict the correct locations of shedding vortex. For uniform flow, [Kerwin and Lee 1978] firstly investigated the effect of wake geometry on the propeller forces. Then, a Vortex Lattice Method (VLM) was applied in axisymmetric inflow in an iterative way to generate the trailing wake of a propeller by [Greely and Kerwin 1982]. Within the same method, this modeling is further developed by [Kinnas and Pyo 1997] to predict the unsteady performance of a propeller subject to inclined inflow. The effect of inclined flow is considered by the geometric inclination of wake geometry including the effect of the radial the tangential velocities. The predicted unsteady forces and moments in terms of the first harmonic are compared with those measured in the experiments. Their correlations showed good agreement, although somewhat diverged toward the lower advance ratios. Beyond

the geometric inclination of the wake, [Keenan 1989] calculated the wake geometry using a VLM in unsteady flow. [H. Lee 2002] developed more reliable and robust wake alignment model for the accurate prediction of propeller performance using BEM. He extended the BEM to predict steady and unsteady geometry of the trailing wake of propellers. A numerical algorithm for the prediction of vortex roll-up and tip cavitation model is included in his work. [L. He 2010] extended a fully unsteady wake alignment algorithm, which was implemented into VLM to simulate unsteady propeller flow. In his work, the interaction between propeller and rudder is investigated in a fully unsteady manner by using ‘the numerical fence.’ The numerical singularity due to close distance between wake and rudder was prevented by surrounding the rudder surface with the numerical barrier. The interaction between propeller and rudder is considered iteratively by solving each problem and then including the unsteady effects of one part on the other. More recently, [Tian. Y and Kinnas 2012] introduced full wake alignment scheme, which aligns the trailing wake to the local velocity. In this thesis, the full wake alignment scheme by [Tian. Y and Kinnas 2012] is intensively investigated and improved to account for the various states of the incoming flow.

1.2 Objective

The goal of this thesis is on improving the full wake alignment scheme for the prediction of open and ducted propeller in steady and unsteady flow. To this end, the following cases are tested using current panel method with the improved wake alignment model:

- Steady state
 - Open propeller in uniform/non-uniform axisymmetric inflow
 - Ducted propeller in uniform inflow
- Unsteady state

- Open propeller in uniform inflow
- Open propeller in inclined shaft flow

For ducted propeller problem, repaneling process on the duct and the duct wake is developed to improve the accuracy and stability of the predicted performance. Also, the improved full wake alignment scheme is extended to the duct wake to represent the natural behavior of shedding vortex behind the duct trailing edge. Beyond the steady state, unsteady wake alignment model is also improved based on the algorithm, proposed by [H. Lee 2002; H. Lee and Kinnas 2004a, 2005b] for the open propeller.

Numerical results from the panel method with the improved wake alignment model are intensively correlated with the results from the experiments and VLM. Based on these comparisons, this thesis is expected to be a through stepping stone for the next step of the current panel method.

1.3 Overview

This thesis is composed of the following six chapters.

In Chapter 1, General introduction to this thesis is presented. Starting from the historical review on the panel method and wake alignment model, the objective and the overview of this thesis are presented.

In Chapter 2, 2-D inviscid formulation of lower order panel method is presented. After that, the panel method is extended to 3-D inviscid formulation.

In Chapter 3, wake alignment model is intensively investigated from steady state to unsteady state. The numerical algorithm in full wake alignment is detailly demonstrated. Based on the understanding on the algorithm, full wake alignment scheme is improved to take into consideration axisymmetric and unsteady inflow. The algorithm in repaneling process on the duct

and the duct wake is demonstrated with a special treatment on the control point on duct panel. The effect of duct panel adaptation to the blade tip is following with the improved loading distribution on the blade. The full wake alignment is also applied to duct wake. Flow charts which show wake alignment process before and after including duct wake alignment are presented. Toward the end of this chapter, unsteady wake alignment scheme is investigated with the consideration of time variations of the inflow on the propeller plane. The basic algorithm is expected to present how the panel method considers the unsteady effect.

In Chapter 4, wake alignment models which have been discussed in Chapter 3 are applied to open and ducted propellers. The numerical results from ducted propeller with square blade tip and sharp trailing edge duct are correlated with those from the experiments and full blown RANS simulations. Also, the predicted unsteady performance of the open propeller in inclined shaft flow are compared to the experimental measurements and the results from VLM.

Chapter 6 summarized all the works presented in this thesis by listing conclusions and is allocated for recommendations to preview the next steps for the current panel method to advance.

Chapter 2

Lower Order Panel Method for Hydrofoil and Propeller Problem

In this chapter, a summary of lower order panel method would be made based on the lecture note of boundary element method [Kinnas 2016]. This chapter starts with the introduction of the two-dimensional inviscid formulation of the panel methods in potential flows. Then, it will be extended to the three-dimensional case, which is straightforward once the application to two-dimensional potential flow is understood.

2.1 Two-Dimensional Inviscid Formulation

Consider a hydrofoil subject to an incoming flow, \vec{U}_{in} as shown in Figure 2.1. Assuming that the flow around the hydrofoil is inviscid and irrotational, the total velocity field \vec{V} can be expressed in terms of a scalar quantity, the total velocity potential, Φ , as follows:

$$\vec{V} = \nabla\Phi \quad (1)$$

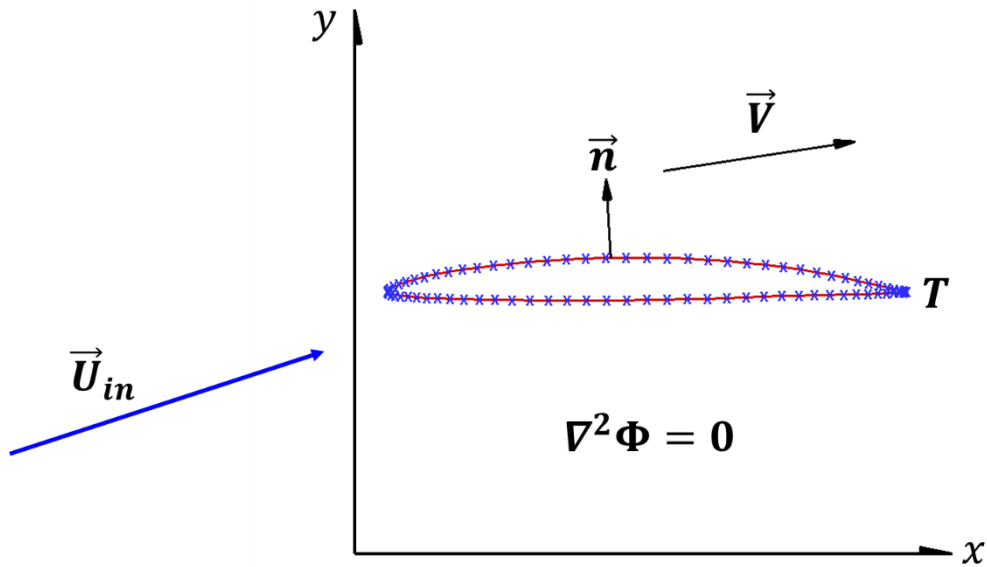


Figure 2.1 Hydrofoil in uniform flow.

The governing equation for Φ inside the fluid domain is:

$$\nabla^2 \Phi = 0 \quad (2)$$

, which means Φ is a harmonic function. The kinematic boundary conditions for Φ are:

$$\frac{\partial \Phi}{\partial n} = \vec{n} \cdot \nabla \Phi = 0 \quad ; \text{ on the foil surface,} \quad (3)$$

where \vec{n} is the normal vector on the foil surface pointing *into* the fluid, as shown in Figure 2.1.

The condition at infinity is:

$$\nabla \Phi \sim \vec{U}_{in} \quad ; \text{ at infinity.} \quad (4)$$

The Kutta condition for the case of hydrofoil is:

$$\nabla\Phi = \text{finite ; at the trailing edge } T. \quad (5)$$

It can be proven that Equation 2, subject to the Equations 3, 4, and 5 has a unique solution. It is the task of the analytical and the computational methods to determine that unique solution Φ . By applying the Green's third identity, the following equation holds:

$$\frac{\Phi_p}{2} = \int_{S_B} \left[\frac{\partial\phi_q}{\partial\mathbf{n}_q} G(p, q) - \phi_q \frac{\partial G(p, q)}{\partial\mathbf{n}_q} \right] ds \quad (6)$$

Equation (6) states that the value of the function ϕ_p at any point on the body B depends *only* on the values of ϕ_q and $\frac{\partial\phi_q}{\partial n_q}$ at any point q on the boundary of the body B . Moreover, the value of ϕ_p can be expressed as the superposition of the potentials due to distribution of sources and normal dipoles on the boundary of the body of strengths $\frac{\partial\phi_q}{\partial n_q}$ and $-\phi_q$ respectively. \mathbf{n}_q denotes the vector at the point q directing into the flow field.

$G(p, q)$ is the Green's function and It has the form of $\frac{\ln(r(p, q))}{2\pi}$ in two-dimensional problem and $-\frac{1}{4\pi r(p, q)}$ in three-dimensional problem. $r(p, q)$ denotes the distance between control point p and variable point q on the boundary.

Special care should be given to the branch wake surface S_W behind the hydrofoil, as shown in Figure 2.2. By considering the wake surface, Equation (6) renders:

$$\frac{\phi_p}{2} = \int_{S_B} \left[\frac{\partial \phi_q}{\partial \mathbf{n}_q} G(p, q) - \phi_q \frac{\partial G(p, q)}{\partial \mathbf{n}_q} \right] ds + \int_{S_W} \left[\frac{\partial \phi_q}{\partial \mathbf{n}_q} G(p, q) - \phi_q \frac{\partial G(p, q)}{\partial \mathbf{n}_q} \right] ds \quad (7)$$

where S_W denotes the surface of trailing edge wake.

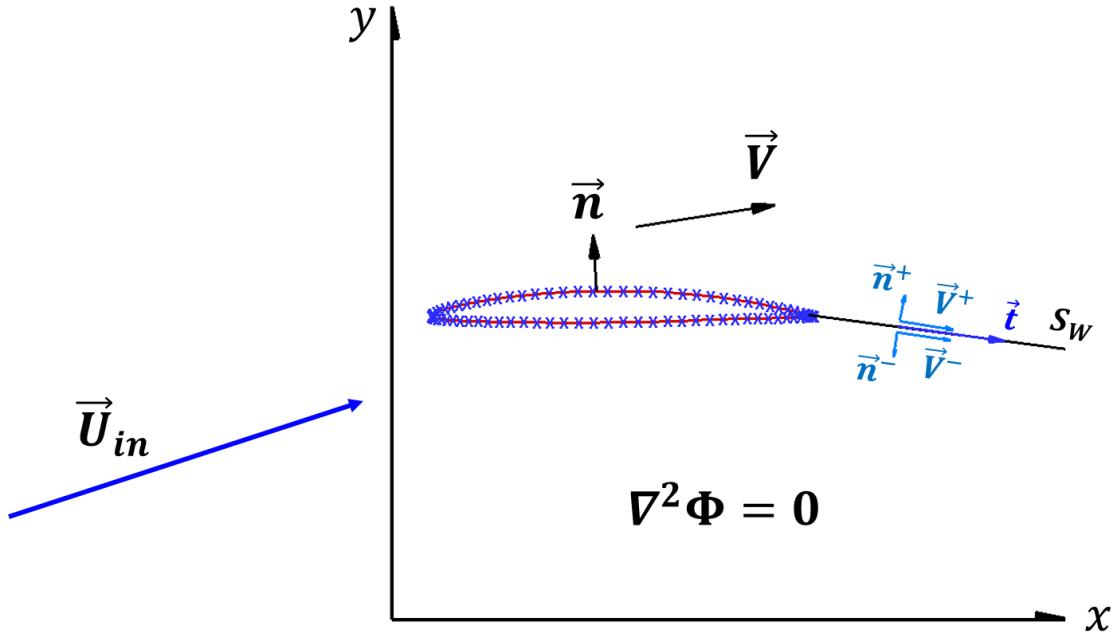


Figure 2.2 Hydrofoil and trailing edge wake in uniform flow stream. n^+ and t are the coordinates normal and tangential to the wake sheet respectively.

The second integral in Equation 7 can be written as:

$$\begin{aligned} & \int_{S_W} \left[\frac{\partial \phi_q}{\partial \mathbf{n}_q} G(p, q) - \phi_q \frac{\partial G(p, q)}{\partial \mathbf{n}_q} \right] ds \\ &= \int_{S_W} \left[\left(\frac{\partial \phi_q^+}{\partial \mathbf{n}_q^+} - \frac{\partial \phi_q^-}{\partial \mathbf{n}_q^-} \right) G(p, q) - (\phi_q^+ - \phi_q^-) \frac{\partial G(p, q)}{\partial \mathbf{n}_q^+} \right] ds \end{aligned} \quad (8)$$

where the superscripts + and – correspond to the upper and lower surface of S_W , respectively.

For the lower and the upper surface of S_W to stay together, we should have for the total fluid velocities on the two side of the wake sheet, \vec{V}^+ and \vec{V}^- :

$$\vec{V}^+ \cdot \vec{n}^+ = \vec{V}^- \cdot \vec{n}^+ = \frac{\partial \Phi^+}{\partial n^+} = \frac{\partial \Phi^-}{\partial n^+} = 0 \quad (9)$$

$$\vec{V}^+ \cdot \vec{t} = \vec{V}^- \cdot \vec{t} \quad (10)$$

where Φ is the total potential which consists of the potential associated to the incoming flow Φ_{in} and the perturbation potential ϕ as follows:

$$\Phi = \Phi_{in} + \phi \quad (11)$$

Therefore, the third term in Equation (9) can be written as:

$$\frac{\partial \Phi^+}{\partial n^+} = \frac{\partial \Phi^-}{\partial n^+} = \frac{\partial(\Phi_{in} + \phi^+)}{\partial n^+} = \frac{\partial(\Phi_{in} + \phi^-)}{\partial n^+} = \frac{\partial \phi^+}{\partial n^+} = \frac{\partial \phi^-}{\partial n^+} \quad (12)$$

And Equation (10) renders:

$$\frac{\partial \Phi^+}{\partial t} = \frac{\partial \Phi^-}{\partial t} \Rightarrow \frac{\partial(\Phi^+ - \Phi^-)}{\partial t} = 0 \quad (13)$$

Equation (13) means that the jump of the potential across the wake remains constant along the wake:

$$\Phi^+ - \Phi^- = \phi^+ - \phi^- = \Delta\phi_W \quad (14)$$

By using Equation (12) and (14), Equation (7) will finally become:

$$\frac{\phi_p}{2} = \int_{S_B} \left[\frac{\partial\phi_q}{\partial\mathbf{n}_q} G(p, q) - \phi_q \frac{\partial G(p, q)}{\partial\mathbf{n}_q} \right] ds - \int_{S_W} \Delta\phi_W \frac{\partial G(p, q)}{\partial\mathbf{n}^+} ds \quad (15)$$

From the kinematic boundary condition of the total potential Φ , the strength of the source potential can be easily obtained:

$$\frac{\partial\phi}{\partial\mathbf{n}} = -\vec{U}_{in} \cdot \vec{n} ; \text{ on the foil surface.} \quad (16)$$

Also, the Kutta condition can be shown that it reduces to Morino's condition [23]:

$$\Delta\phi_W = \phi_T^+ - \phi_T^- \quad (17)$$

where ϕ_T^+ and ϕ_T^- denote the potentials at the upper (suction) and the lower (pressure) side of the trailing edge of hydrofoil respectively. By using Equation (16), Green's formula for the hydrofoil problem finally becomes:

$$\frac{\phi_p}{2} = \int_{S_B} \left[(-\vec{U}_{in} \cdot \mathbf{n}_q) G(p, q) - \phi_q \frac{\partial G(p, q)}{\partial \mathbf{n}_q} \right] ds - \int_{S_W} \Delta \phi_W \frac{\partial G(p, q)}{\partial \mathbf{n}^+} ds \quad (18)$$

Equation (18) is a Fredholm integral equation of the second kind for the unknown ϕ . This analytic formulation will be solved for the unknown quantity, ϕ_p by using numerical implementation.

2.2 Numerical Implementation

Assuming that the hydrofoil in Figure 2.2 is discretized into N straight panels, and its wake into N_W straight panels, perturbation potential formulation of Equation (18) can be discretized into the following form:

$$\begin{aligned} \frac{\phi_j}{2} = & \sum_{i=1, i \neq j}^N (-\vec{U}_{in} \cdot \mathbf{n}_i) \int_{S_{B_i}} G(j, i) ds_i - \sum_{i=1, i \neq j}^N \phi_i \int_{S_{B_i}} \frac{\partial G(j, i)}{\partial \mathbf{n}_i} ds_i \\ & - \Delta \phi_W \sum_{k=1}^{N_W} \int_{S_{W_k}} \frac{\partial G(j, k)}{\partial \mathbf{n}_k} ds_k \end{aligned} \quad (19)$$

where j and i are control point and variable point at midpoint of panel j and panel i on hydrofoil respectively. k denotes variable point at midpoint of panel k on wake surface. S_{B_i} and S_{W_k} are the area of panel i and w on hydrofoil and wake surface, respectively. Equation (19) can be written into the form:

$$\sum_{i=1}^N A_{ji} \phi_i + W_j \Delta \phi_W = \sum_{i=1}^N (-\vec{U}_{in} \cdot \mathbf{n}_i) B_{ji} \quad (20)$$

where,

$$A_{ji} = \int_{S_{B_i}} \frac{\partial G(j, i)}{\partial \mathbf{n}_i} ds_i, j \neq i, A_{ii}$$

$$= \frac{1}{2} \text{ (dipole influence coefficient of panel } i \text{ on control point } j)$$

$$W_j = \sum_{k=1}^{N_w} \int_{S_{W_k}} \frac{\partial G(j, k)}{\partial \mathbf{n}_k} ds_k \text{ (dipole influence coefficient of wake panel } k \text{ on control point } j)$$

$$B_{ji} = \int_{S_{B_i}} G(j, i) ds_i \text{ (source influence coefficient of panel } i \text{ on control point } j).$$

2.3 Three-Dimensional Inviscid Formulation

Three-dimensional inviscid formulation is basically the same as two-dimensional formulation except for the consideration of the interaction between different strips. A three-dimensional geometry of a blade with its trailing wake is given in Figure 2.3. Assume that the blade and its wake are discretized into N and N_w panels in the chordwise and streamwise direction, respectively. Both geometries are discretized into M strips in spanwise direction.

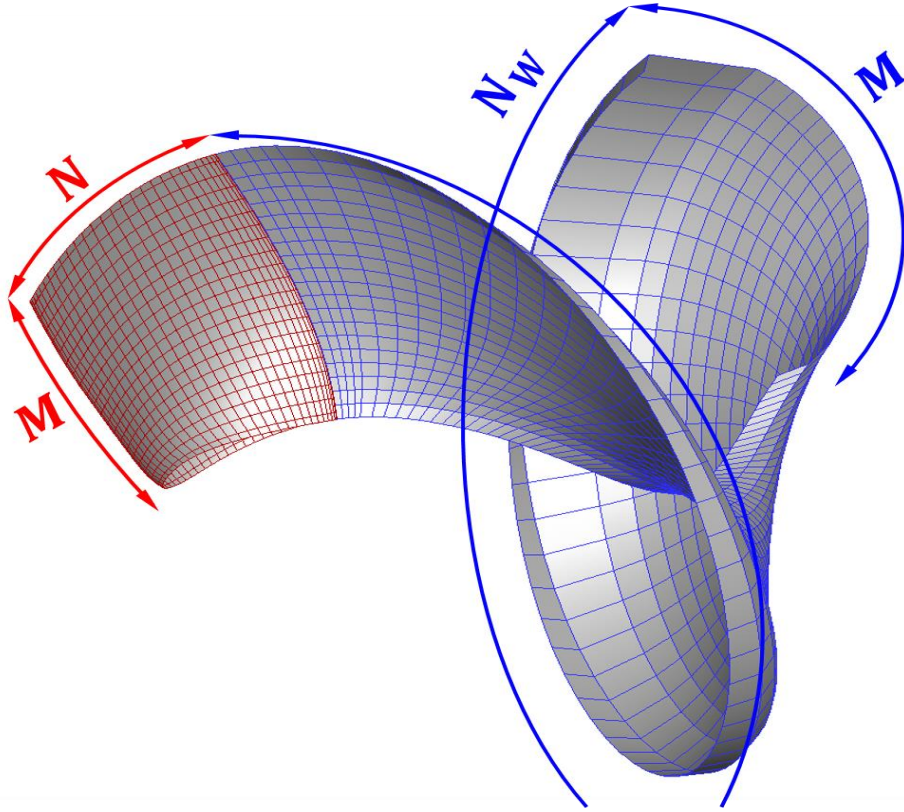


Figure 2.3 Paneling of a 3-D blade and wake.

To account for the interaction between different strips, the discretized form of Equation (21) should be written in a matrix form as:

$$\begin{aligned}
 & \begin{pmatrix} A^{11} & A^{12} & \dots & A^{1M} \\ A^{21} & A^{22} & \dots & A^{2M} \\ \vdots & \vdots & \ddots & \vdots \\ A^{M1} & A^{M2} & \dots & A^{MM} \end{pmatrix} \begin{pmatrix} \phi^1 \\ \phi^2 \\ \vdots \\ \phi^M \end{pmatrix} \\
 &= - \begin{pmatrix} W^{11} & W^{12} & \dots & W^{1M} \\ W^{21} & W^{22} & \dots & W^{2M} \\ \vdots & \vdots & \ddots & \vdots \\ W^{M1} & W^{M2} & \dots & W^{MM} \end{pmatrix} \begin{pmatrix} \Delta\phi_{W,1} \\ \Delta\phi_{W,2} \\ \vdots \\ \Delta\phi_{W,M} \end{pmatrix} \\
 &+ \begin{pmatrix} B^{11} & B^{12} & \dots & B^{1M} \\ B^{21} & B^{22} & \dots & B^{2M} \\ \vdots & \vdots & \ddots & \vdots \\ B^{M1} & B^{M2} & \dots & B^{MM} \end{pmatrix} \begin{pmatrix} S^1 \\ S^2 \\ \vdots \\ S^M \end{pmatrix}
 \end{aligned} \tag{21}$$

where \mathbf{A}^{PQ} is a matrix of size $N \times N$ which denotes the dipole influence coefficients of blade panels at strip Q on blade panels at strip P . It can be written as:

$$\mathbf{A}^{PQ} = [A_{ji}^{PQ}] = \begin{pmatrix} A_{11}^{PQ} & A_{12}^{PQ} & \cdots & A_{1N}^{PQ} \\ A_{21}^{PQ} & A_{22}^{PQ} & \cdots & A_{2N}^{PQ} \\ \vdots & \vdots & \ddots & \vdots \\ A_{N1}^{PQ} & A_{N2}^{PQ} & \cdots & A_{NN}^{PQ} \end{pmatrix}_{N \times N} \quad (22)$$

where A_{ji}^{PQ} is the dipole influence coefficient of panel i at strip Q on control point j at strip P .

$\boldsymbol{\phi}^P$ is a vector matrix of size $N \times 1$ which denotes the velocity potential at strip P which is in the form of:

$$\boldsymbol{\phi}^P = [\phi_i^P] = \begin{pmatrix} \phi_1^P \\ \phi_2^P \\ \vdots \\ \phi_N^P \end{pmatrix}_{N \times 1} \quad (23)$$

ϕ_i^P is the velocity potential on panel i of strip P .

\mathbf{W}^{PQ} is a matrix of size $N \times N_w$ which denotes the dipole influence coefficients of wake panels at strip Q on blade panels at strip P . It can be written as:

$$\mathbf{W}^{PQ} = [W_{ji}^{PQ}] = \begin{pmatrix} W_{11}^{PQ} & W_{12}^{PQ} & \cdots & W_{1N_w}^{PQ} \\ W_{21}^{PQ} & W_{22}^{PQ} & \cdots & W_{2N_w}^{PQ} \\ \vdots & \vdots & \ddots & \vdots \\ W_{N1}^{PQ} & W_{N2}^{PQ} & \cdots & W_{NN_w}^{PQ} \end{pmatrix}_{N \times N_w} \quad (24)$$

where W_{ji}^{PQ} is the dipole influence coefficient of wake panel i at strip Q on blade panel j at strip P .

$\Delta\phi_{W,P}$ is the trailing wake strength at wake strip P . Note that this is scalar quantity since the trailing wake strength is a constant along each strip in steady problem.

\mathbf{B}^{PQ} is a matrix of size $N \times N$ which denotes the source influence coefficients of blade panels at strip Q on blade panels at strip P . It can be written as:

$$\mathbf{B}^{PQ} = [B_{ji}^{PQ}] = \begin{pmatrix} B_{11}^{PQ} & B_{12}^{PQ} & \dots & B_{1N}^{PQ} \\ B_{21}^{PQ} & B_{22}^{PQ} & \dots & B_{2N}^{PQ} \\ \vdots & \vdots & \ddots & \vdots \\ B_{N1}^{PQ} & B_{N2}^{PQ} & \dots & B_{NN}^{PQ} \end{pmatrix}_{N \times N} \quad (25)$$

where B_{ji}^{PQ} is the source influence coefficient of blade panel i at strip Q on blade panel j at strip P .

\mathbf{S}^P is a vector matrix of size $N \times 1$ which denotes the source strength at strip P which is in the form of:

$$\mathbf{S}^P = [S_i^P] = \begin{pmatrix} S_1^P \\ S_2^P \\ \vdots \\ S_N^P \end{pmatrix}_{N \times 1} \quad (26)$$

S_i^P is the source strength on blade panel i of strip P .

Equation (21) is the final form of three-dimensional formulation of the panel method for the propeller problem in potential flow. It will be solved for the unknown velocity potentials, ϕ on the propeller boundary. Viscous/inviscid interactive method, which was introduced by [Yu 2012] and

[Purohit 2013], can be used to account for the viscous effects around two or three dimensional geometries. In this thesis, the panel method will remain within inviscid area.

Chapter 3

Full Wake Alignment

3.1 Steady Wake Alignment

To predict the propeller performance using panel method, accurate prediction of the blade trailing wake geometry is essential. Wake alignment scheme in steady state is important because it provides the bases with which unsteady wake alignment starts its first iteration. Also, the engineering community is more interested in the steady (mean) performance of the propulsion system. Therefore, this thesis starts its investigation into wake alignment scheme for steady state. Then, the investigation will continue into the unsteady state in Section 3.4.

3.1.1 Previous Research

There have been several wake alignment schemes suggested for the prediction of steady performance of propeller. [Kerwin 1981] developed a relatively simple wake alignment model, PSF-2 wake alignment scheme. Then, [Greeley et al. 1982] further developed this model for the analysis in steady flow. PSF-2 wake model assumes wake region into two parts, i.e. transitional wake and ultimate wake. In the transitional wake, PSF-2 model first aligns the most inner and outer shedding vortex lines based on the computed flow. Vortex lines in the middle are interpolated using those two end lines. Induced velocity from the propeller and the contraction of the transitional wake are considered to evaluate the axial, tangential, and radial location of the transitional wake. On the other hand, ultimate wake is assumed to be infinitely extended into upstream and downstream by [Loukakis 1971]. [Tian. Y 2012] showed that proper wake alignment model can improve the predicted propeller performance particularly at the low advance ratio and

introduced a pseudo-unsteady wake alignment scheme (full wake alignment scheme, or simply FWA). [Kinnas et al. 2015] extended this scheme for ducted propellers by including the duct-induced velocities in the FWA. In the case of ducted propeller, as will be discussed in the later section in detail, wake alignment model is critical because the blade trailing wake influences loading distribution over the duct in very close distance. This influence becomes even more significant in a zero-gap and square-tip ducted propeller case [Kinnas et al. 2015]. Similar methods were also applied by [Baltazar et al. 2013, 2015], who included a reduction in the pitch of the blade wake at its tip to account for the boundary layer over the duct inner surface.

In this chapter, a lot of efforts have been given to improve FWA for open and ducted propeller in steady flow. FWA can also be applied to the unsteady wake alignment, which aligns the wake at each time step by using the aligned wake from steady state. Unsteady wake alignment is put aside for a moment and will be intensively investigated in the following section, based on the knowledge of the steady state.

3.1.2 Basic Idea

One of the biggest merits of the FWA is that it represents shedding vortex from trailing edge of the blade (or, simply wake) as a material surface. In other words, the locations of four corners of the wake panels are determined based on the local flow velocity, as shown in Figure 3.1. To locate the corner points at the accurate positions, the local flow velocity in the fluid domain needs to be carefully evaluated.

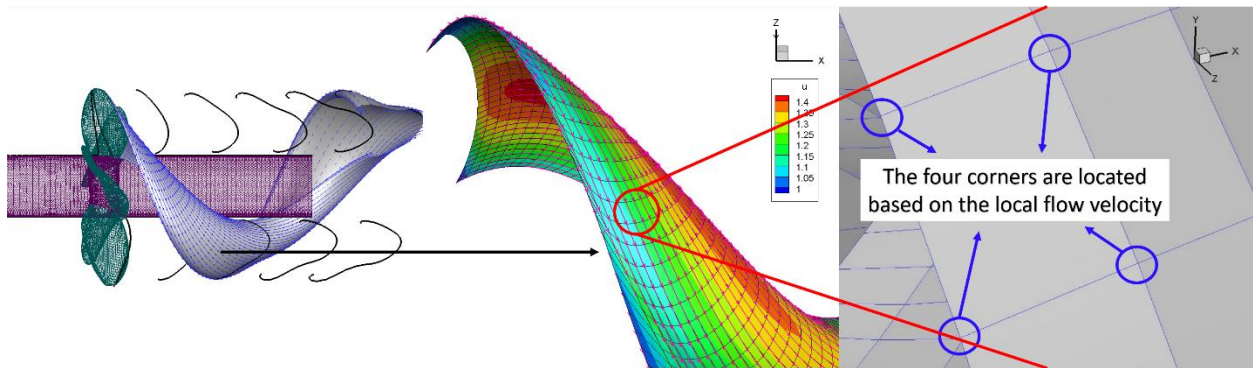


Figure 3.1 Key wake with local velocity vectors plotted on each nodal point of the wake

FWA model starts its alignment by considering the incoming flow with its rotational component around propeller. The dominant inflow would be along helices with constant pitch when uniform inflow is assumed. The helices represent the wake panels, which are aligned based on only the uniform inflow without considering the perturbation velocity due to the propeller geometry. The helical wake panels are shown in Figure 3.2.

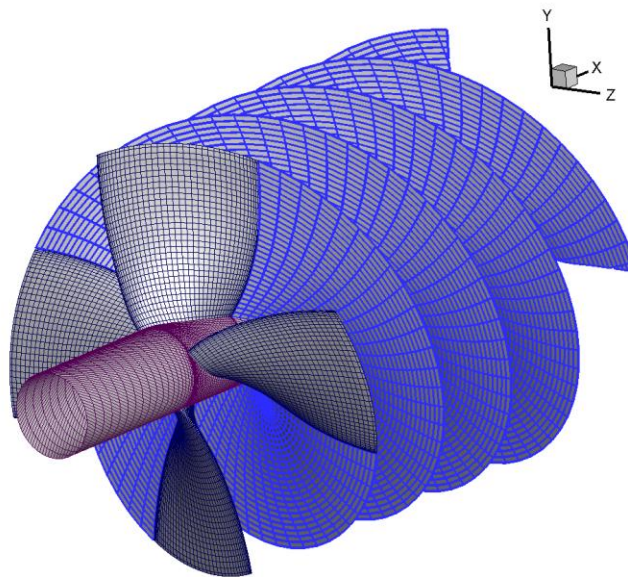


Figure 3.2 Open propeller with helical wake aligned with the uniform inflow.

The perturbation velocity is evaluated at each nodal point on the wake panels, same as the inflow. Then, the mean perturbation velocity, $\hat{\mathbf{u}}_i$ is evaluated between $i-1$ th and i th nodes to calculate the perturbation velocity induced at i th node.

$$\hat{\mathbf{u}}_i = \frac{1}{2}(\mathbf{u}_{i-1} + \mathbf{u}_i) \quad (3.1)$$

This mean velocity is added up to the inflow to perturb the helical wake. To this end, the mean perturbation velocity is decomposed into the two directions by using the inner product; one along the inflow direction, $\hat{u}_{i,s}$ and the other normal to the inflow direction, $\hat{\mathbf{u}}_{i,n}$. The former would be added up to the inflow velocity since both are in the same direction (note that $\hat{u}_{i,s}$ is the inner product of the mean perturbation velocity onto the inflow direction).

$$\begin{aligned} \hat{u}_{i,s} &= \hat{\mathbf{u}}_i \cdot \mathbf{s}_i \\ \hat{\mathbf{u}}_{i,n} &= \hat{\mathbf{u}}_i - \hat{u}_{i,s}\mathbf{s}_i \end{aligned} \quad (3.2)$$

Where \mathbf{s}_i is the unit direction vector on a vortex segment which connects the $i-1$ th to the i th point. Considering that the mean perturbation velocity is decomposed based on the inflow direction, having the correct helical wake which represents the direction of uniform inflow is very important. The algorithm that FWA uses to generate the helical wake is as follows.

Consider the two consecutive points in a cylindrical coordinate system with subscripts $i-1$ and i .

$$\begin{aligned}
x_i &= x_{i-1} + \frac{RJ_s\Delta\theta}{\pi} \\
r_i &= r_{i-1} \\
\theta_i &= \theta_{i-1} + \Delta\theta
\end{aligned} \tag{3.3}$$

Where x_i , r_i , and θ_i are the axial, the radial, and the tangential coordinates. R is the radius of the propeller, J_s is the advance ratio, and $\Delta\theta$ is the parameter that determines the grid size of wake in streamwise direction. With the local velocity and the value of $\Delta\theta$, the axial length of a wake panel is determined. Reducing the value of $\Delta\theta$ will cause the increase in the number of wake panels to keep the wake length fixed in streamwise direction. Equation (3.3) can also be expressed in the local Cartesian coordinate system with subscripts i and $i - 1$:

$$\Delta\mathbf{s}_i = \begin{pmatrix} \frac{RJ_s\Delta\theta}{\pi} \\ r_{i-1}[\cos(\theta_{i-1} + \Delta\theta) - \cos\theta_{i-1}] \\ r_{i-1}[\sin(\theta_{i-1} + \Delta\theta) - \sin\theta_{i-1}] \end{pmatrix} \tag{3.4}$$

$$\mathbf{s}_i = \frac{\Delta\mathbf{s}_i}{|\Delta\mathbf{s}_i|} \tag{3.5}$$

where R is the blade radius, J_s is the advance ratio, and r_i and θ_i are the radial and the tangential coordinates of the i th node on wake. $\Delta\mathbf{s}_i$ is the vortex segment (the edge size of a wake panel in streamwise direction) connecting the $i-1$ th to the i th point in Cartesian coordinate system. The essence of FWA is to fix the length of vortex segment, $\Delta\mathbf{s}_i$ in the inflow direction and then to align the vortex line with the two velocity components: $\hat{\mathbf{u}}_{i,s}$ and $\hat{\mathbf{u}}_{i,n}$. In other words, vortex lines (strips

of wake panels) are firstly generated based on the inflow, and then the vortex lines are perturbed by the perturbation velocities.

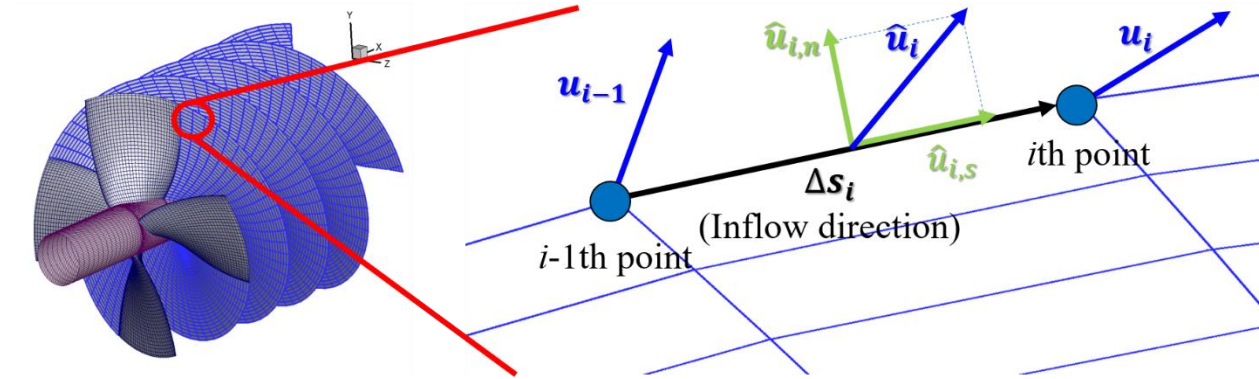


Figure 3.3 Helical inflow wake and the two components of the perturbation velocity, $\hat{u}_{i,s}$ and $\hat{u}_{i,n}$, induced along and normal to the inflow direction.

3.1.3 Alignment Algorithm

To derive the alignment algorithm, a pseudo unsteady alignment approach, which was introduced to simulate the leading edge vortex (LEV) for delta wings with sharp leading edge by [Tian and Kinnas 2011], is adopted. As drawn in Figure 3.4, consider a material line placed in a velocity field in the x and y directions:

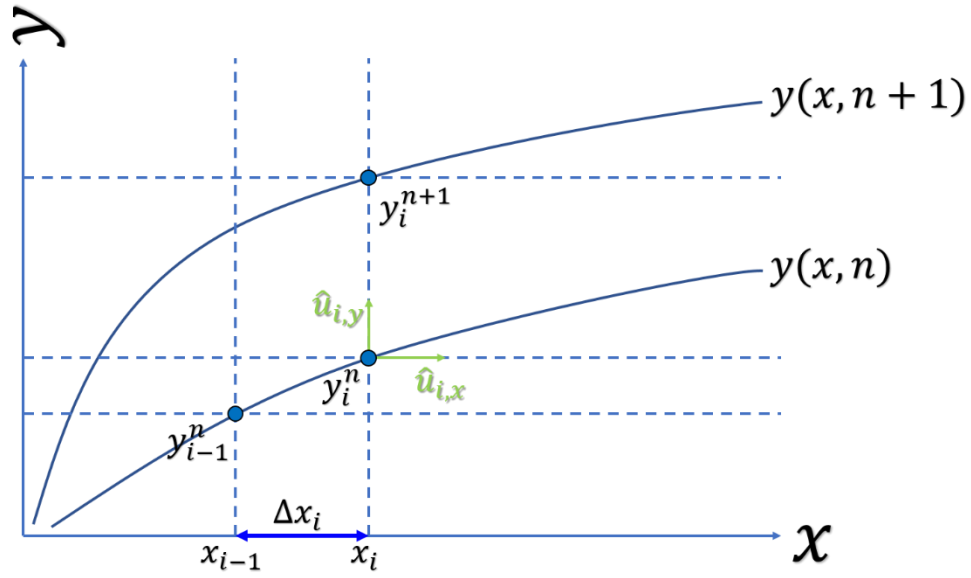


Figure 3.4 Schematic plot of a material line before (y_i^n) and after (y_i^{n+1}) alignment in a pseudo unsteady alignment approach (note that the same denotation is used for the mean velocity in Figure 3.5).

In the two-dimensional case, as shown in Figure 3.4, the x and y directions are analogous to the inflow direction and the direction normal to inflow in the propeller problem, respectively. Also, Δx_i is analogous to Δs_i in Figure 3.3 and here indicates the vortex segment connecting $i-1$ th point to i th point in the x direction.

From the material line, we have

$$y = y(x, t) \tag{3.6}$$

$$u_y = \frac{Dy}{Dt} = \frac{\partial y}{\partial t} + u_x \frac{\partial y}{\partial x} \tag{3.7}$$

$$\frac{\partial y}{\partial t} = q_y - q_x \frac{\partial y}{\partial x} \tag{3.8}$$

Equation (3.8) can be discretized using the Euler-Explicit scheme for the unsteady terms and finite difference scheme for the slopes. Then, we get:

$$\begin{aligned}
y_i^{n+1} &= y_i^n + \frac{\Delta t}{2} \left[(u_{i-1,y}^n + u_{i,y}^n) - (u_{i-1,x}^n + u_{i,x}^n) \frac{y_i^n - y_{i-1}^n}{x_i^n - x_{i-1}^n} \right] \\
&= y_i^n + \Delta t \left[\hat{u}_{i,y} - \hat{u}_{i,x} \frac{y_i^n - y_{i-1}^n}{x_i^n - x_{i-1}^n} \right] \\
&= \left(\frac{\Delta t}{\Delta x_i} \hat{u}_{i,x} \right) \frac{\hat{u}_{i,y} \Delta x_i}{\hat{u}_{i,x}} + \left(1 - \hat{u}_{i,x} \frac{\Delta t}{\Delta x_i} \right) y_i^n + \hat{u}_{i,x} \frac{\Delta t}{\Delta x_i} y_{i-1}^n
\end{aligned} \tag{3.9}$$

where $\hat{u}_{i,x} = \frac{1}{2}(u_{i-1,x}^n + u_{i,x}^n)$, $\hat{u}_{i,y} = \frac{1}{2}(u_{i-1,y}^n + u_{i,y}^n)$, and $\Delta x_i = x_i^n - x_{i-1}^n$. Defining $\Delta t_i^* = \frac{\Delta x_i}{\hat{u}_{i,x}}$,

and $\beta = \frac{\Delta t}{\Delta t_i^*}$, we rewrite (3.9) as follows:

$$\begin{aligned}
y_i^{n+1} &= \hat{u}_{i,y} \Delta t + \left(1 - \frac{\Delta t}{\Delta t_i^*} \right) y_i^n + \frac{\Delta t}{\Delta t_i^*} y_{i-1}^n \\
&= \beta \hat{u}_{i,y} \Delta t_i^* + (1 - \beta) y_i^n + \beta y_{i-1}^n
\end{aligned} \tag{3.10}$$

$$\begin{aligned}
z_i^{n+1} &= \hat{u}_{i,z} \Delta t + \left(1 - \frac{\Delta t}{\Delta t_i^*} \right) z_i^n + \frac{\Delta t}{\Delta t_i^*} z_{i-1}^n \\
&= \beta \hat{u}_{i,z} \Delta t_i^* + (1 - \beta) z_i^n + \beta z_{i-1}^n
\end{aligned} \tag{3.11}$$

Notice that the alignment Equations (3.10) and (3.11) are derived based on the two-dimensional plane under horizontal inflow. The idea behind this approach is that the vortex segment has the fixed length of Δx_i and the vertical coordinates, i.e. y or z are changed along the line which is normal to the vortex segment. Numerically, Equations (3.10) and (3.11) behave like an upwind scheme since the vortex segment is in the direction of the dominant inflow.

Unlike the alignment procedure in the two-dimensional problem which is quite straight forward, three-dimensional problem, such as the flow around a propeller, requires the alignment scheme to consider a rotational component of the inflow. Defining $\Delta t_i^* = \frac{|\Delta \mathbf{s}_i|}{\left(\hat{u}_{i,swprop} \frac{\Delta \theta}{|\mathbf{s}_i|} + 1\right)} = \frac{|\Delta \mathbf{s}_i|}{\left(\hat{u}_{i,swprop} + 1\right)}$ and $\beta = \frac{\Delta t}{\Delta t_i^*}$, we can obtain the final expression for the wake alignment scheme for the

propeller wake:

$$\begin{aligned} \mathbf{X}_i^{n+1} &= \hat{\mathbf{u}}_{i,n} \Delta t + \left(1 - \frac{\Delta t}{\Delta t_i^*}\right) \mathbf{X}_i^n + \frac{\Delta t}{\Delta t_i^*} (\mathbf{X}_{i-1}^n + \Delta \mathbf{s}_i) \\ &= \beta \hat{\mathbf{u}}_{i,n} \Delta t_i^* + (1 - \beta) \mathbf{X}_i^n + \beta (\mathbf{X}_{i-1}^n + \Delta \mathbf{s}_i) \end{aligned} \quad (3.12)$$

where superscript n denotes the coordinates at n th time step, with \mathbf{X}_i being the vector from the origin to the point i on wake sheet. Based on Equation (3.12), the helical inflow wake will be aligned into the two directions, i.e. the inflow direction and the direction normal to the inflow. The basic idea is the same as two-dimensional problem except that the vortex segment is placed on a helix in this case. It would be interesting to compare Figure 3.5 below with Figure 3.4 to understand how the alignment scheme in the simple two-dimensional case is transformed into the three-dimensional propeller problem.

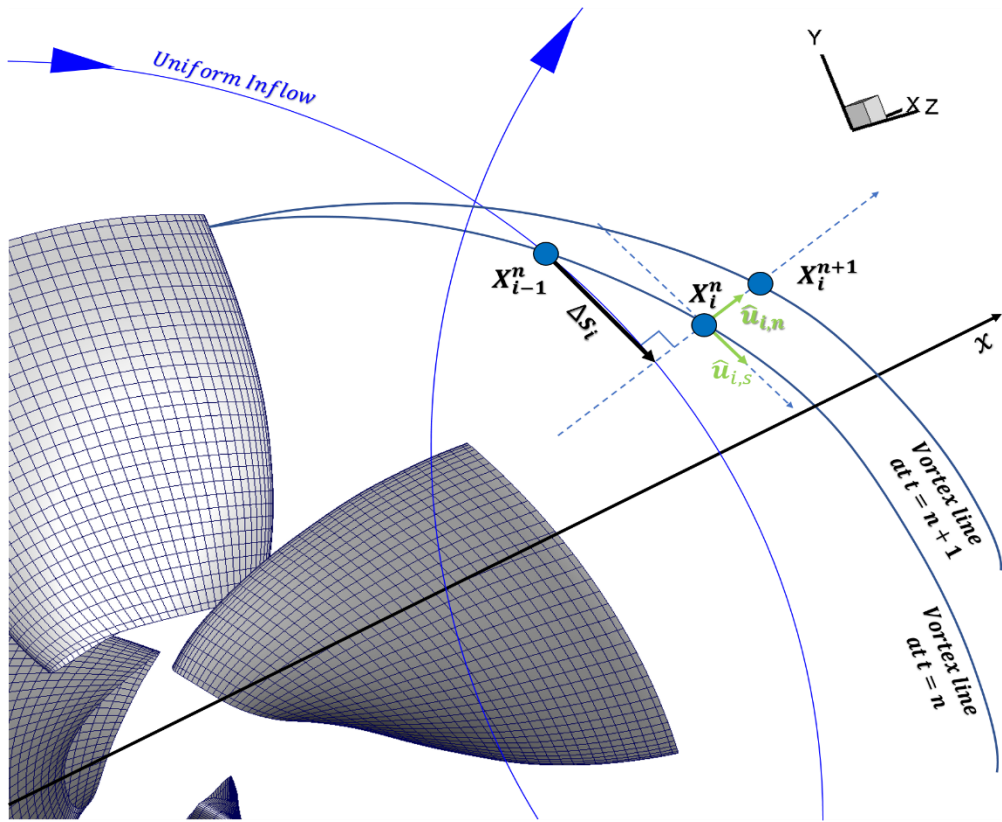


Figure 3.5 Schematic plot of a vortex line before (X_i^n) and after (X_i^{n+1}) alignment using FWA.

The FWA is basically based on the iterative method to reach a fully aligned steady wake. For the first *outer* iteration, the panel method generates a helical wake based on the inflow. Blade and hub are generated before wake is formed. In the case of the ducted propeller case, panels on the duct and duct wake are adapted to the helical wake before starting the outer iteration. With these initial geometries, the potential equation is solved to evaluate the potentials over the discretized propeller body. Once the potentials are calculated, FWA starts the *inner* iterations to align the blade wakes. During these inner iterations, the potentials do not change. However, the velocity components, i.e. inflow and the perturbation velocity evaluated at wake panels keep changing since the wake panels are repeatedly updated until the inner iteration reaches the maximum iteration number. The inner iteration is also terminated if the convergence criterion regarding the wake geometry is satisfied.

Due to the movements of the wake panels during the inner iterations, the perturbation velocity induced on the wake is reevaluated. Once the inner iteration terminates with the firstly aligned wake for the next outer iteration, the FWA begins the next outer iteration to solve the potential equation based on the influence coefficients from the updated wake. This process will be repeated until the outer iteration reaches its maximum iteration number or a converged blade force is achieved. If the repaneling process on the duct is included, influence coefficients from the repaneled the duct and the duct wake should also be reevaluated. Since the repaneling process is conducted along with FWA algorithm, the repaneling process remains to be discussed in Section 3.2. Figure 3.6 summarizes the iterative steps built in FWA.

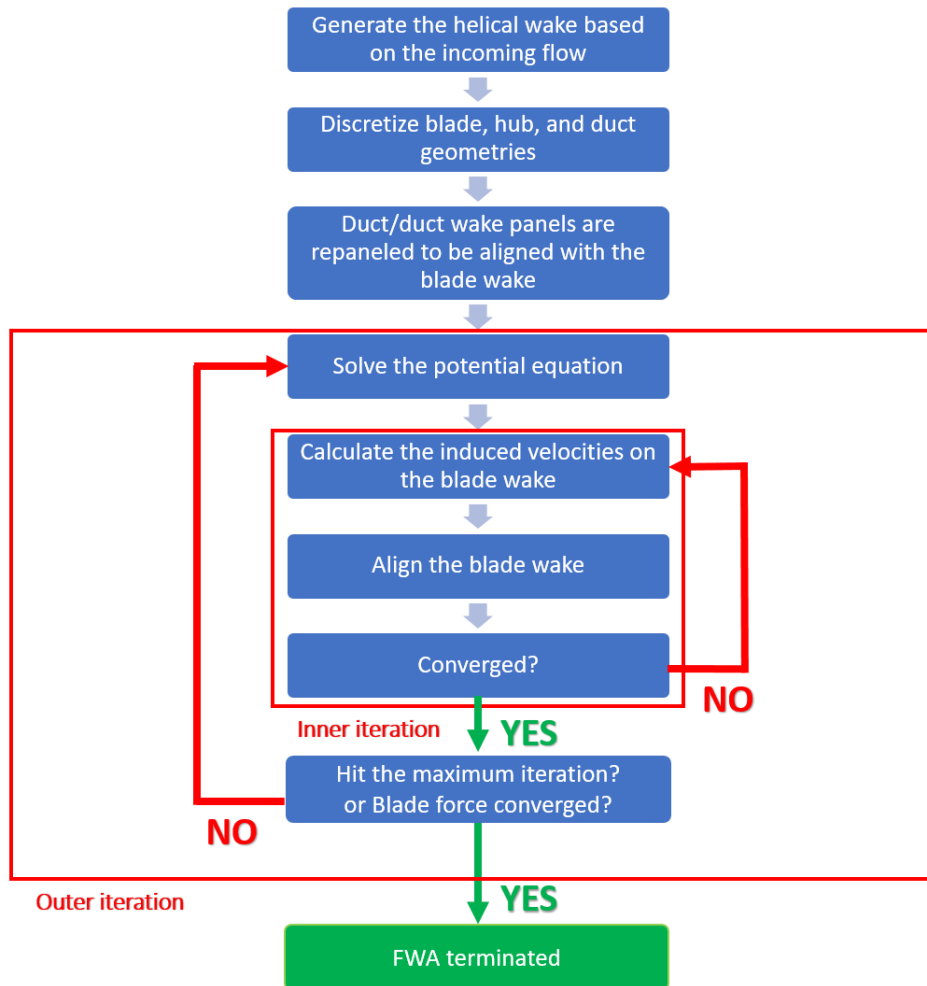


Figure 3.6 Flowchart of the iterative algorithm constructed in FWA scheme.

3.1.4 Inflow Consideration

The FWA scheme assumes uniform inflow. To handle the case with non-uniform inflow, the helical shape of the inflow wake should be changed according to the inflow profile, which can be non-uniform. To this end, the algorithm generating the inflow wake needs to be modified such that it can consider the information on the incoming flow. Therefore, the vortex segment connecting the $i-1$ th and the i th points in the Cartesian system should be generated based on Equation (3.13) instead of Equation (3.4).

$$\Delta \mathbf{s}_i = \widehat{U}_{in_i} * \Delta t = \begin{pmatrix} \frac{1}{2} (\overline{U}_{x_{i-1}} + \overline{U}_{x_i}) * \Delta t \\ \frac{1}{2} (\overline{U}_{y_{i-1}} + \overline{U}_{y_i}) * \Delta t \\ \frac{1}{2} (\overline{U}_{z_{i-1}} + \overline{U}_{z_i}) * \Delta t \end{pmatrix} \quad (3.13)$$

where \widehat{U}_{in_i} denotes the mean inflow velocities evaluated using the inflow velocities at the $i-1$ th and the i th nodal points on the wake panels.

Different from Equation (3.4), which finds the i th point on the helice with a constant radius of r_{i-1} , Equation (3.13) calculates the i th point based on the local inflow velocity which is evaluated at each nodal point. The inflow velocities are evaluated based on the interpolation of effective wake, which is given in the form of harmonics as an input data. Once the inflow wake is generated based on Equation (3.13), rest of the alignment algorithm is the same as the case in uniform inflow. Figure 3.7 shows the fully aligned wake from the panel method using FWA in uniform and non-uniform inflow. The non-uniform inflow cases are somewhat extreme, but presented here to clearly show the difference in the aligned wake based on the different inflow profiles. Note that the effect

of hub on the wake is not considered here. In other words, the perturbation velocity from hub is not included in the velocity that FWA uses to align the wake. This is why the wake panels very near the hub have curling.

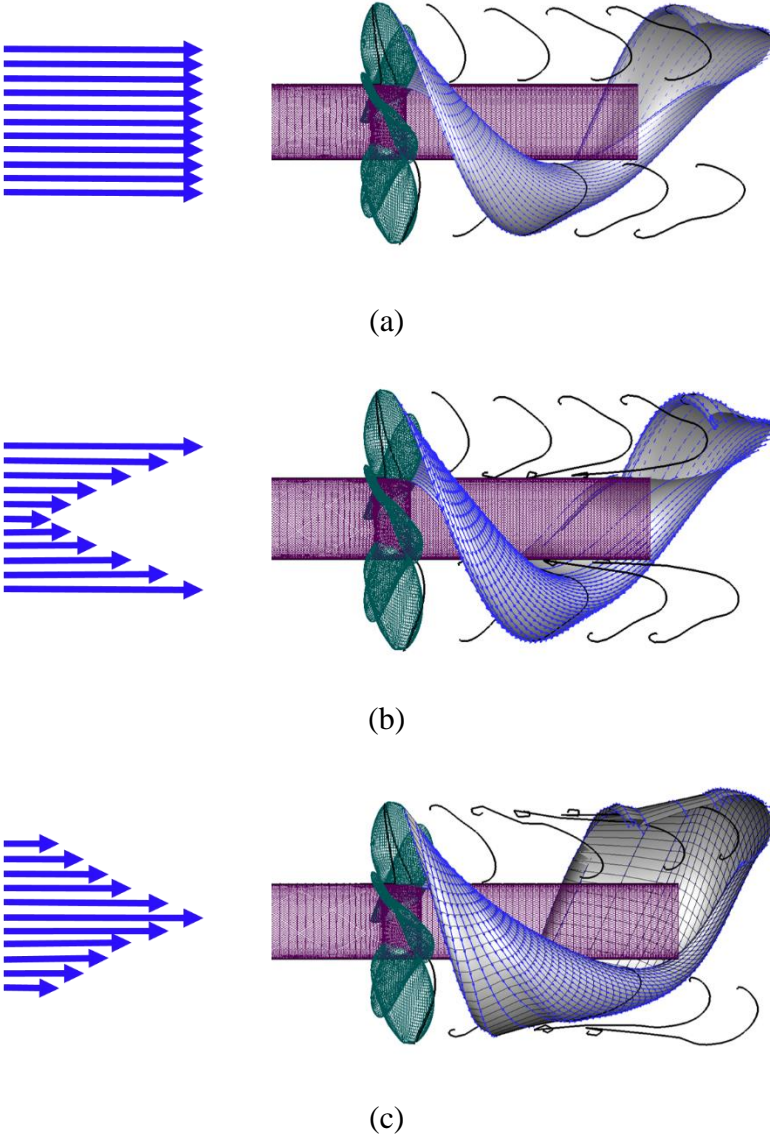


Figure 3.7 Fully aligned wake panels using FWA in (a) uniform and (b, c) non-uniform inflow.

3.2 Repaneling of the Duct and the Duct Wake

In this section, FWA is applied to ducted propeller with an emphasis on the duct paneling. Numerical results in this section show that proper paneling on the duct improve not only the stability of FWA scheme but also the predicted loading on the blade (especially, toward the blade tip). The performance prediction of a square-tip ducted propeller is addressed with the effects of panel distribution on both the duct and the duct wake. As shown in Figure 3.8, the square tip KA4-70 ducted propeller inside the 19Am sharp-trailing-edge duct is used in this study. An infinite hub is adopted and a sealed gap is assumed between the blade tip and the duct inner side.

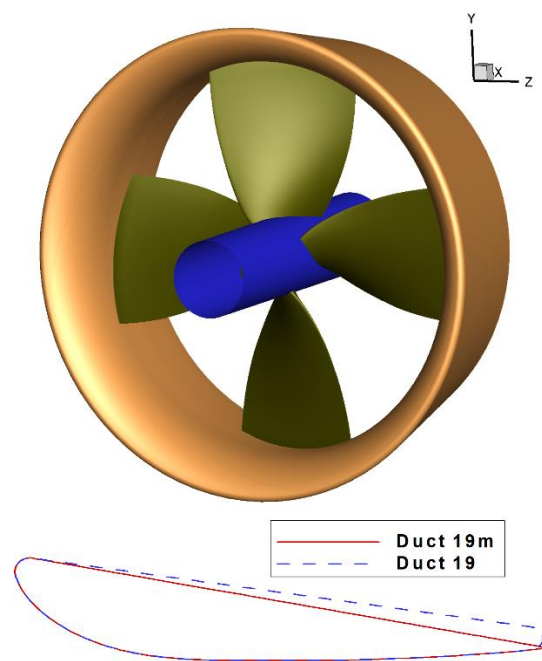


Figure 3.8 KA4-70 ducted propeller geometry (upper) and the duct cross section shape (lower).

3.2.1 Algorithm

In the present method, a helical wake is used for the blade (based on the advance ratio), and the panels on the duct and duct wake are adapted according to the helical blade wake. Based on the solution from this initial propeller geometry, inner iterations (the same denotation defined in section 3.1.3 is used to be consistent throughout this thesis) within FWA are conducted to align the blade wake. During these inner iterations, the panels on the duct and its wake, as well as the potentials on the duct and its wake and on the blade and its wake *do not* change. During the inner iterations, only the shape of the blade wake is modified based on the FWA scheme. The velocities induced by the blade and its wake and the duct and its wake on the blade wake are reevaluated at the beginning of each inner iteration. Once the inner iterations have reached convergence (again, in terms of the wake geometry), the outer iterations begin. Before starting a new outer iteration, FWA is required to determine a repaneling option among the following two repaneling options.

3.2.2 The Two Repaneling Options

(a) Option 1: The duct and the duct wake panels are not modified, i.e. they are kept the same as the initial geometries, which are repaneled based on the helical blade wake. The blade wake panels keep changing throughout the iterations in FWA.

(b) Option 2: At the beginning of each outer iteration, the duct and the duct wake panels are adapted to the blade wake panels, which are updated from the last inner iteration.

In both options above, the potentials on the blade, hub, and duct are reevaluated at each outer iteration. Note that in Option 1 the panels on the duct and its wake do not change but the potentials on the blade, hub, and duct are changing since the blade wake has been updated. A

variation of Option 1 was introduced by [H. Fan 2015]. Figure 3.9 summarizes the procedure of FWA including the two repaneling options.

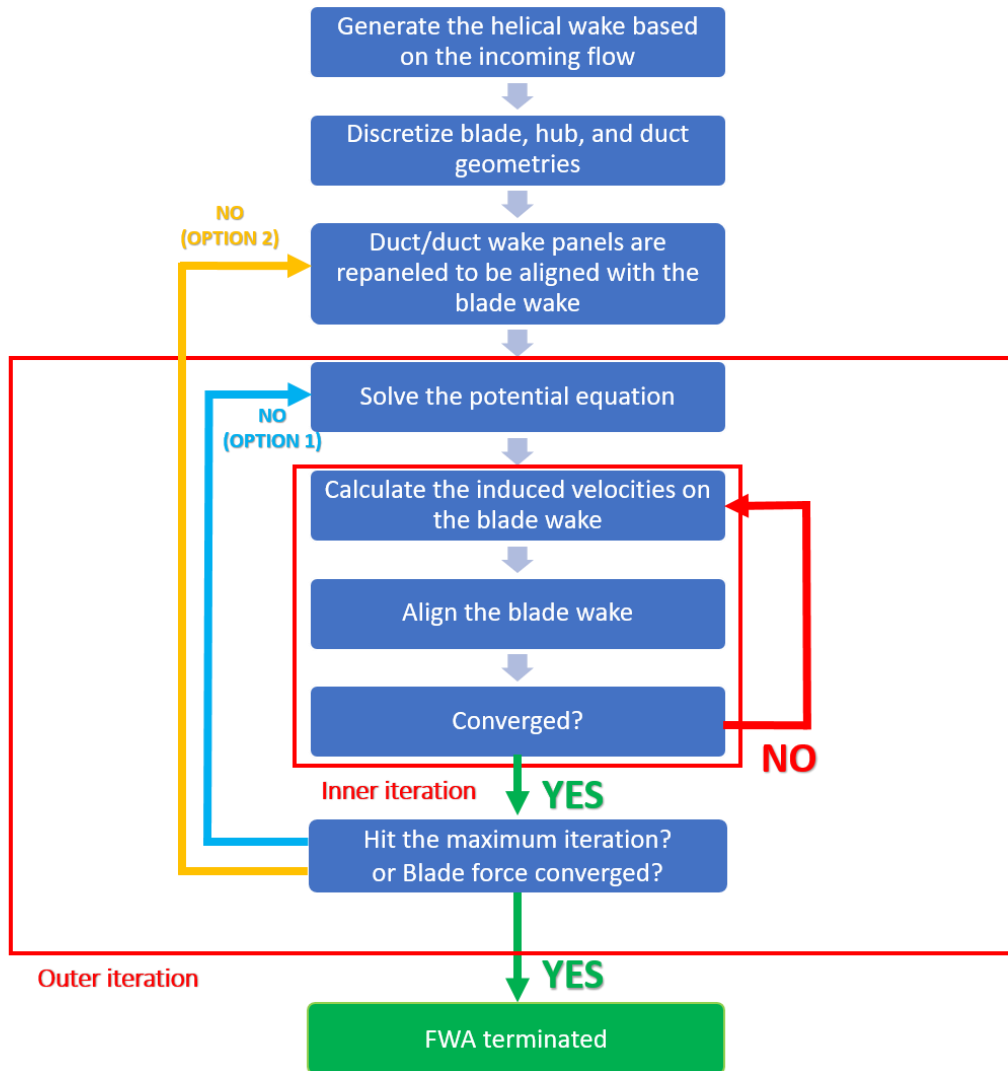


Figure 3.9 Flow chart of FWA with duct and duct wake repaneling options.

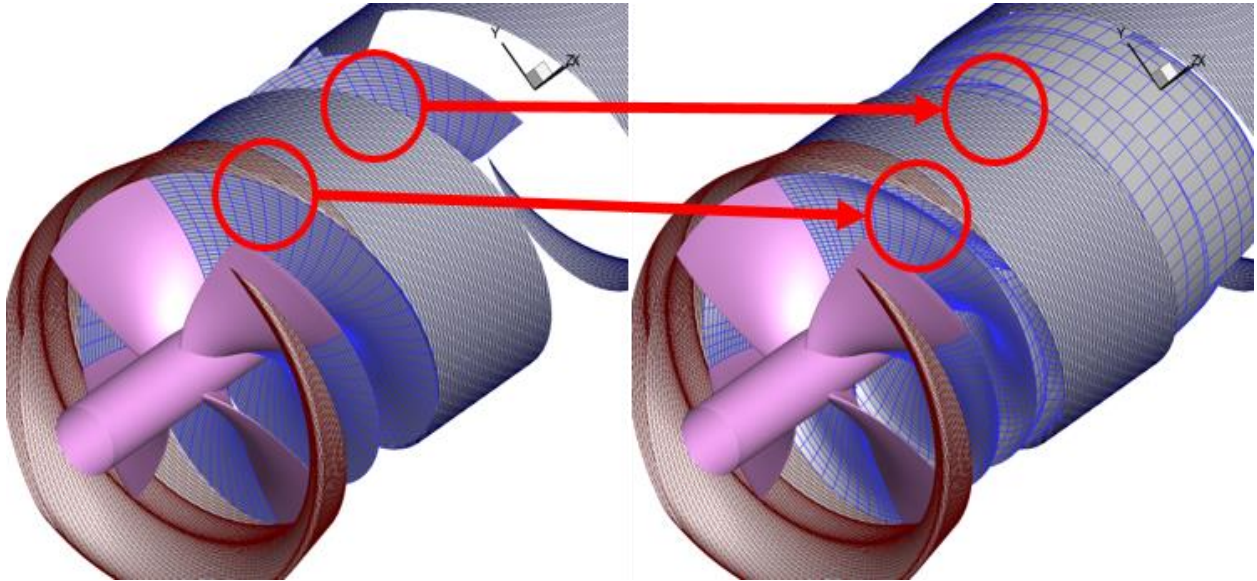


Figure 3.10 Blade/duct wake from the first (left) and second (right) iteration in FWA with repaneling Option 1. Red circles clearly show duct and duct wake are *not* adapted to the blade wake in the second iteration. KA4-70 ducted propeller is used at the design advance ratio, $J_s=0.50$.

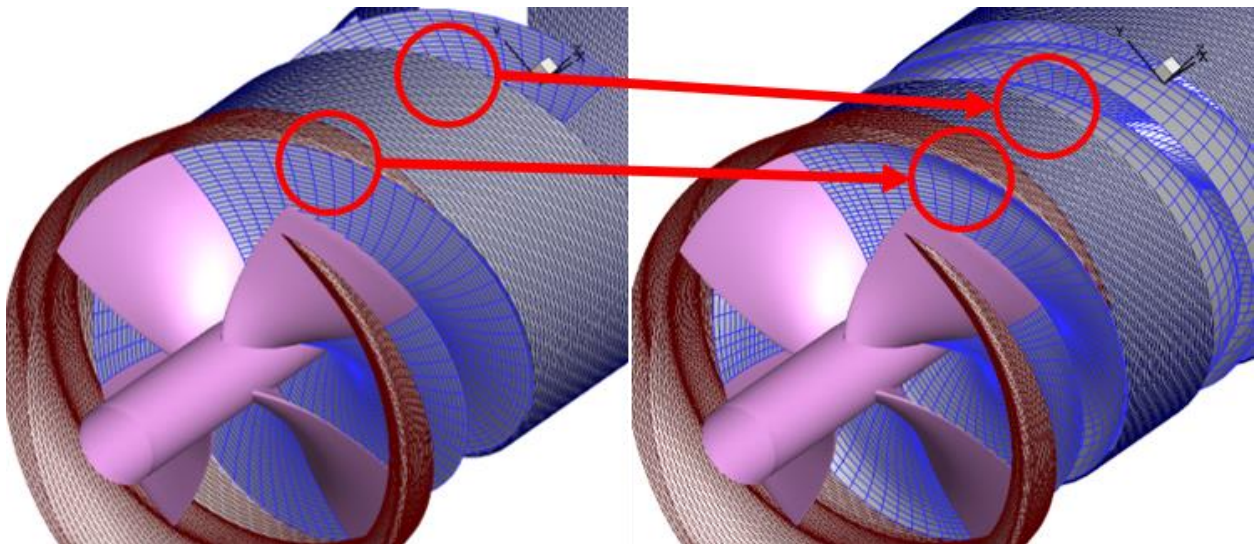


Figure 3.11 Blade/duct wake from the first (left) and second (right) iteration in FWA with repaneling Option 2. Red circles clearly show duct and duct wake are adapted to the blade wake in the second iteration. KA4-70 ducted propeller is used at the design advance ratio, $J_s=0.50$.

At the end of an inner iteration loop (just before a new outer iteration begins), the outer edge of the blade wake might intersect the duct inner surface or the duct wake. Duct wake here is assumed to be a cylinder, which starts from the duct trailing edge. If the intersection happens, the outer edge of the blade wake is forced in the radial direction to be located at the duct inner surface or the duct wake surface. The intersection might happen because the natural behavior of the shedding vortex from the trailing edge of the duct is ignored by assuming the cylindrical shape of the duct wake, which is unrealistic in the real case. The best way of resolving this issue is to align the duct wake using FWA as in the case of the blade wake. This has been done, and FWA applied to the duct wake is investigated later in section 3.3 in detail.

Penetration problem between the outer edge of the blade wake and the duct inner surface requires a different treatment from what is used for the penetration between the blade wake and the duct wake. This is because duct geometry is set to be the wall with the wall boundary condition, which does not allow for an alignment scheme to change the outline of the duct. When the aligned blade wake happens to penetrate this wall, therefore, wake panels are geometrically redistributed to avoid the singularities due to the penetration. To this end, cubic spline interpolation is used to approximate the duct inner surface, then if the aligned wake falls above the approximated surface, the exceeded part will be cut off by the surface. To keep the same number of wake panels in spanwise direction after the truncation, panels are redistributed on the remaining part of the wake.

The effects of the repaneling options on the performance predictions of the ducted propellers are presented in Chapter 4. Correlations with the results from the experiments and RANS simulations are investigated to validate the results from the panel method.

3.2.3 Treatment of Control Point on the Duct Panel

Considering most of the offshore structures use ducted propeller as their primary propulsion source to be stationary at a specific location in the ocean, predicting the performance of ducted propellers in the lower advance ratio becomes important.

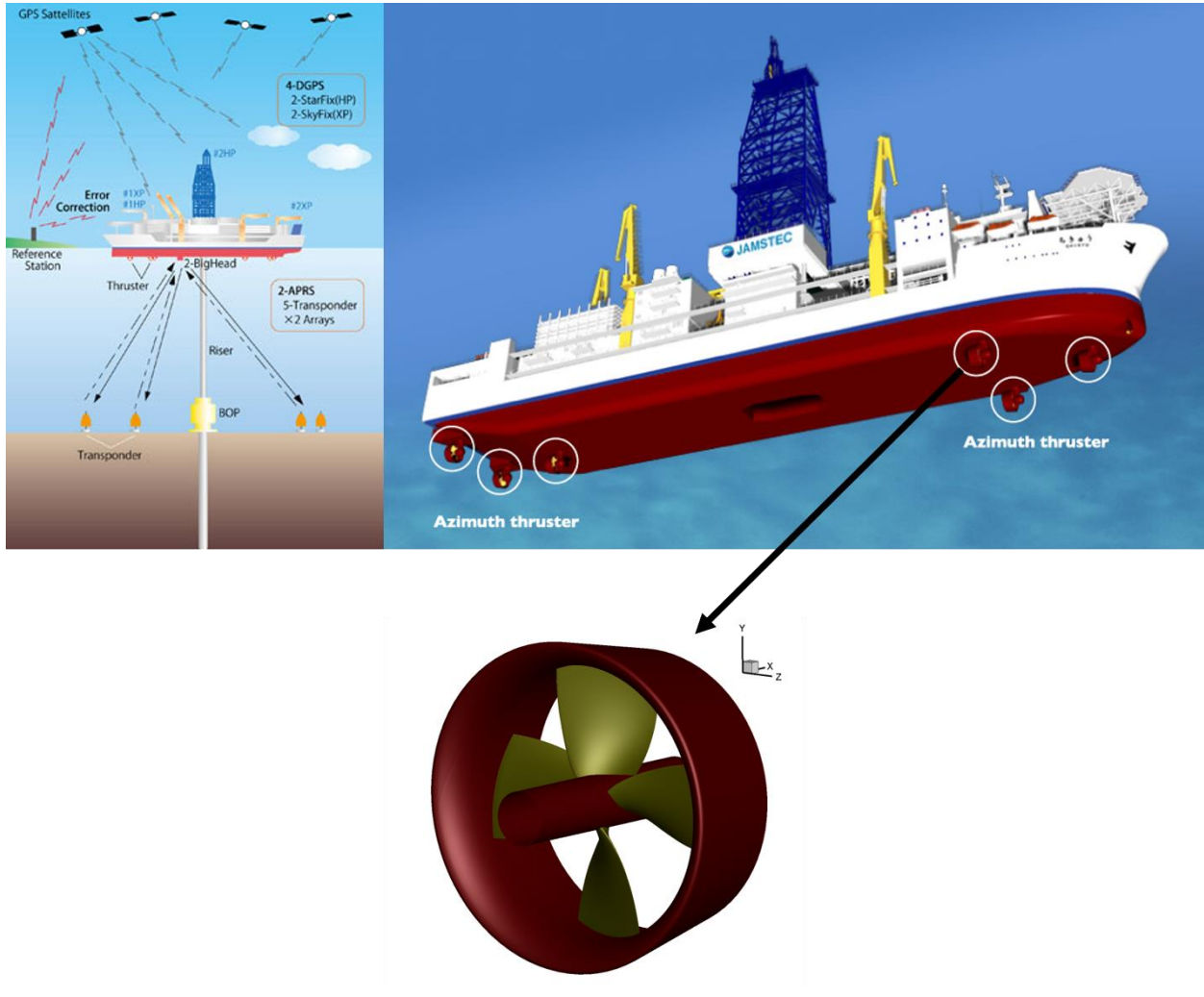


Figure 3.12 ducted propeller attached to an offshore structure [32] which keeps its position in the ocean with the help of the ducted propeller and dynamic positioning system (DPS) [33].

In order to predict the reasonable results using repaneling Option 2, especially at the low advance ratios, careful attention needs to be given to the control points on the non-planar panels.

The locations of the control points on the planar panels, which have its four corners on the same plane, are located at the same plane as the corner points (Figure 3.14). However, in the case of non-planar panels, control points are not located at the same plane as the corner points (Figure 3.13).

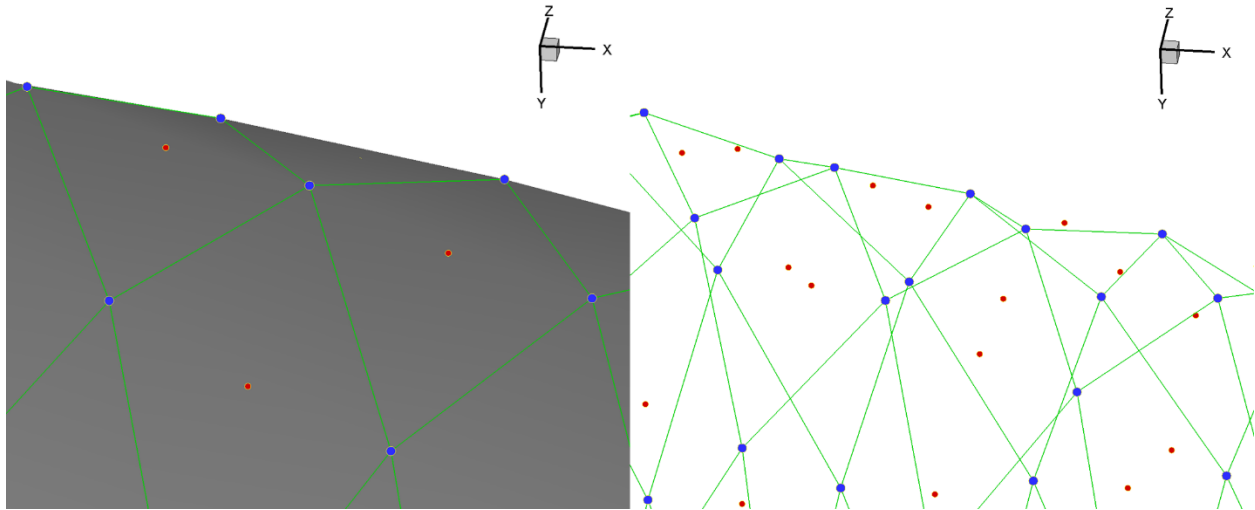


Figure 3.13 Non-planar panels with contour (left)/without contour (right). Control points (red circle) are not on the same plane as the panel corners (blue circles).

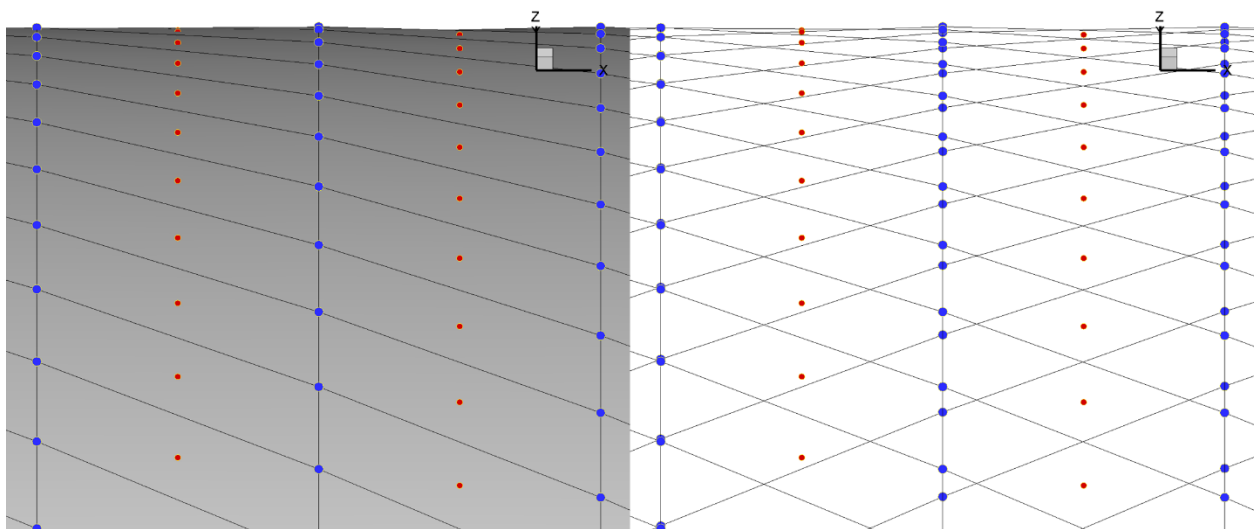


Figure 3.14 Planar panels with contour (left)/without contour (right). Control points (red circle) are on the same plane as the panel corners (blue circles).

If the locations of the control points on duct panels are wrongly evaluated due to the non-planarity of the duct panels, the control points can get closer to the outer edge of wake panels in the radial directions. If the distance between a control point and wake panels become too close, abnormal velocities are induced on the wake panels when evaluating the perturbation velocity from duct. As a result, wake panels get severely distorted, leading to the crash of wake alignment scheme.

Figure 3.15 shows ducted propellers with the aligned wake at several advance ratios, i.e. $J_s=0.3, 0.5,$ and 0.7 . The only half and a quarter of the propeller geometry and wake are presented respectively for clarity. As shown, in the case of the lower advance ratios, blade wakes do not advance farther to downstream from blade than the case with the higher advance ratios. Therefore, duct panels become compact and should rotate further to the circumferential direction to be adapted to the wake panels which are compact in the axial direction. As a result, duct panels become non-planar panels, as shown in Figure 3.16. The ‘twisted’ duct panels produce wrong locations of the control points which might get closer to the outer edge of blade wake. Figure 3.17 summarizes how the singular behaviors happen to the wake panels due to the wrong position of the control points on the duct panels.

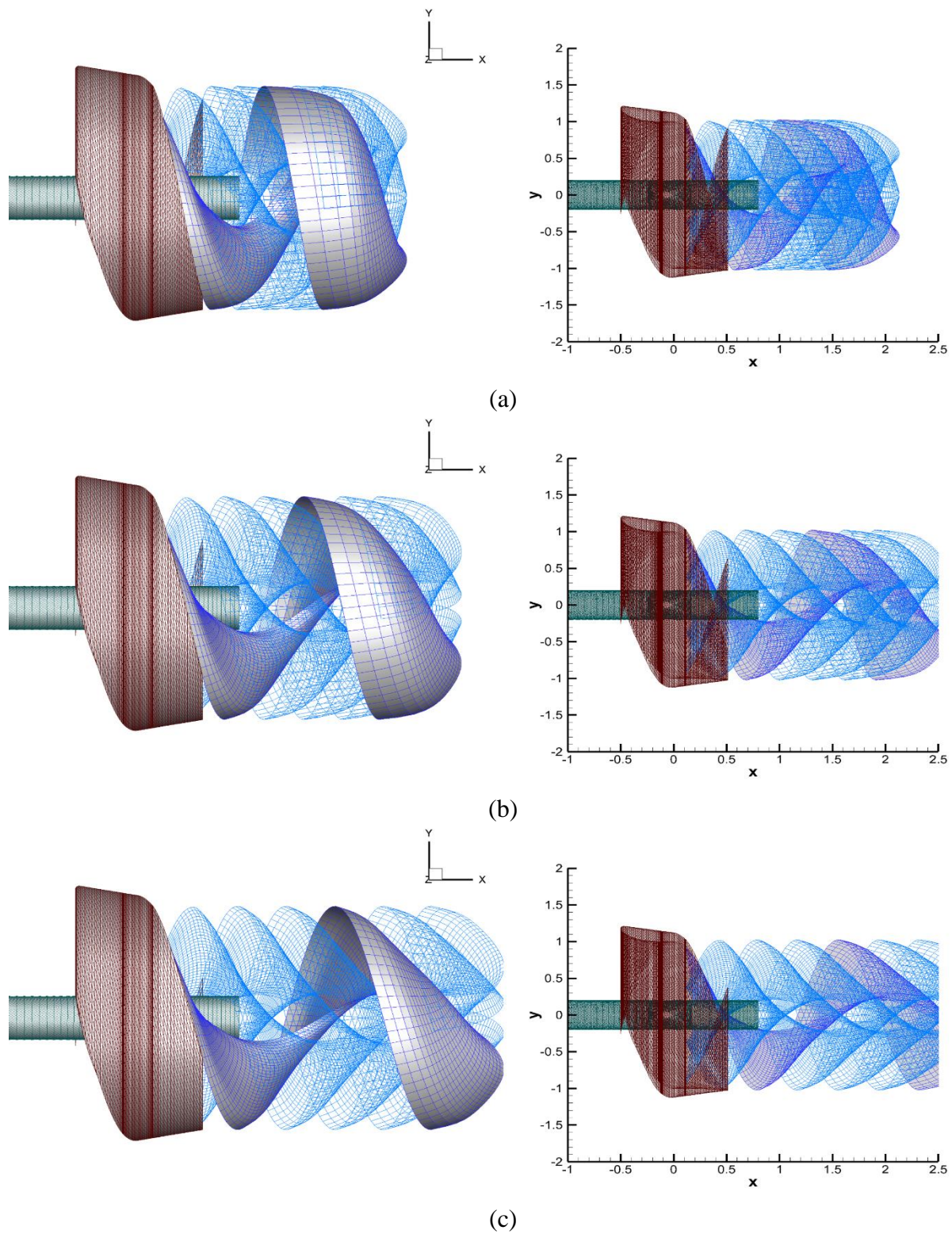


Figure 3.15 Wake and duct geometry of KA4-70 ducted propeller in three-dimensional plot (left) and two-dimensional plot (right) at $J_s=(a)$ 0.30, (b) 0.50, and (c) 0.70. Duct wake is not presented here.

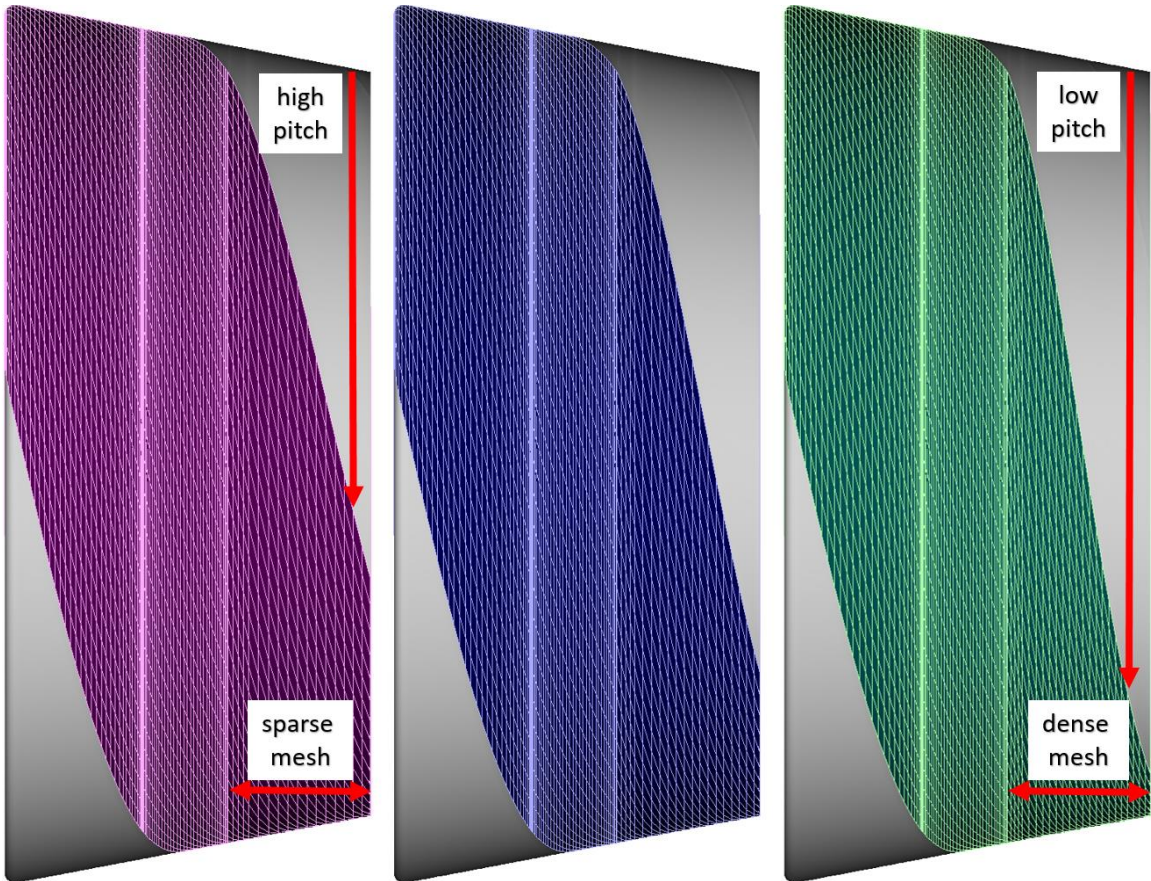


Figure 3.16 Panel distributions on duct surface. Panels are adapted to the blade wake at $J_s=0.7$ (left), 0.5 (middle), and 0.3 (right). Duct geometries are taken from KA4-70 ducted propeller.

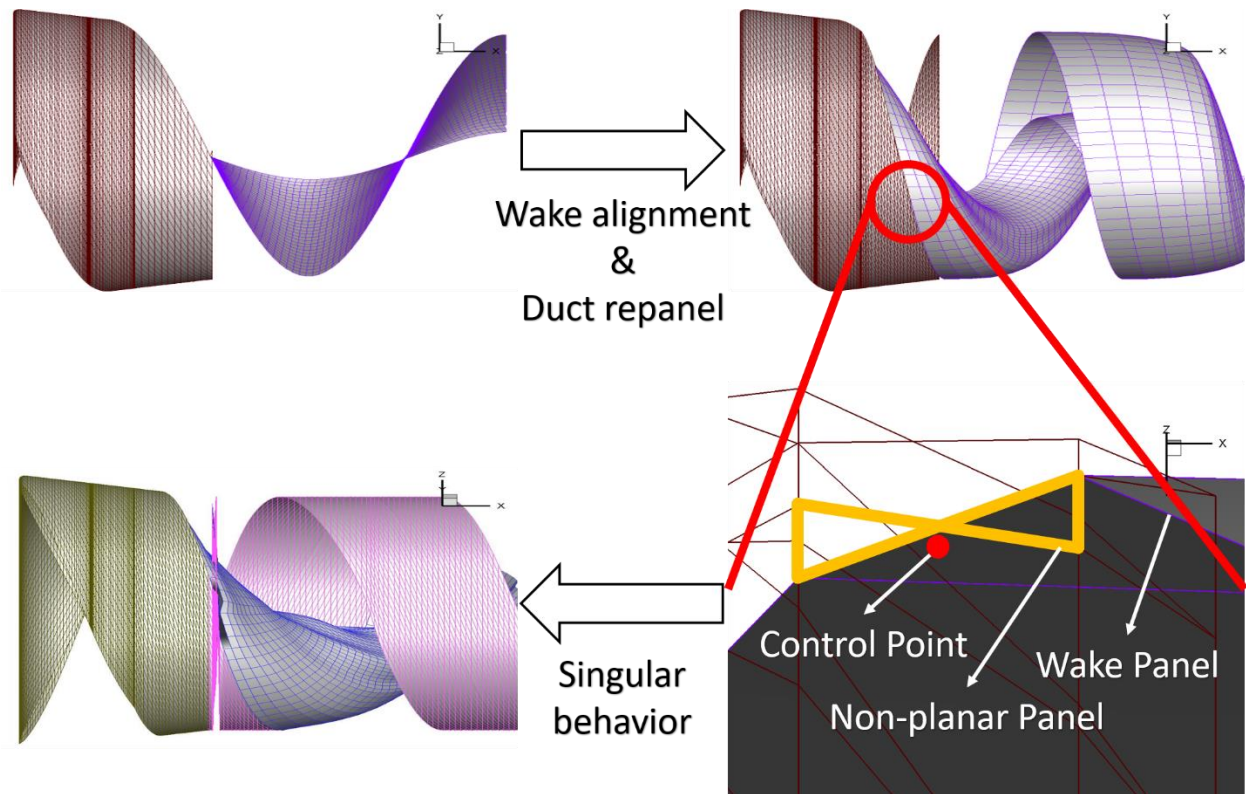


Figure 3.17 Distortion of the wake panels due to the abnormally induced velocity at the low advance ratios.

To resolve this problem, the non-planar panels are forced to become planar panels before evaluating the locations of the control points at the centroid of each panel. Among the four corner points on a non-planar panel, the circumferential offset of the two points on downstream side are forced in circumferential direction to be the same locations as their counter points on the other side. In other words, one side of a non-planar panel is rotated into the rotating direction of the blade. Although each point might have different radial locations depending on the outline of duct surface, it helps to find proper locations of a control point by changing the non-planar panel into ‘stretched’ panel on duct surface. By replacing the radial coordinates of control points on the non-planar panel with the one evaluated on a stretched panel, the singular behaviors on the blade wake can be effectively avoided. As a result, this treatment improved the convergence of repaneling

Option 2 such that it can produce more stable convergence history of propeller performance at the low advance ratio, compared to the other choice, Option 1. It will be more addressed by comparing the results from the panel method using both repaneling options with those from the experiments in Chapter 5.

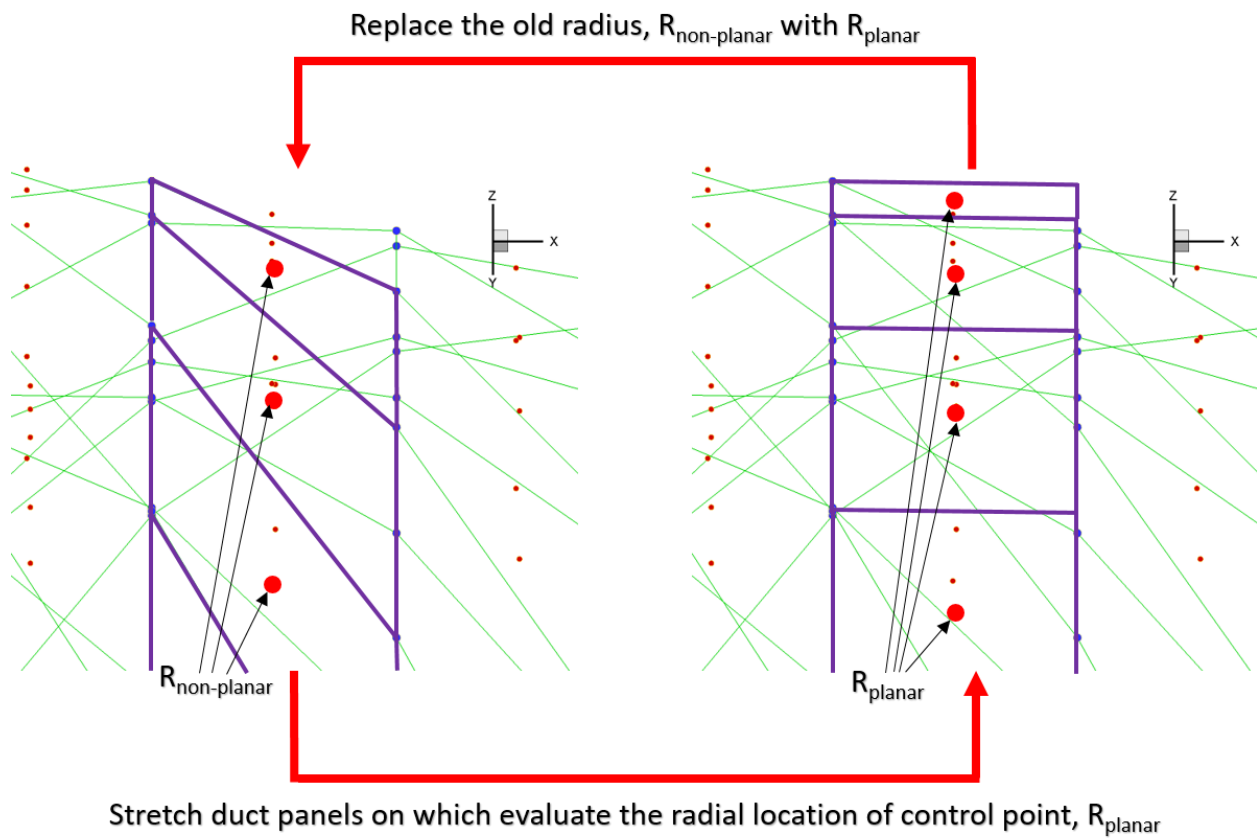


Figure 3.18 Replacement of the radial locations of the control points by stretching the non-planar panels on the duct.

3.2.4 Effect of Panel Adaptation on Loading Distribution over Blade

As mentioned earlier, the results from the current panel method are improved if blade/blade wake adapted grid on the duct/duct wake is used. In addition to the panel alignment between the blade wake and the duct inner side, panel alignment between blade tip and duct inner side is also

important to produce the correct loading distribution over the blade, especially toward the blade tip. For a square tip blade case with zero gap, in which blade tip touches duct inner side along the chord, panel matching or mismatching between the two geometries end up with different circulation distributions around the blade tip. Figure 3.19 demonstrates the adapted and not adapted grids on the duct, and the resulting circulations are presented in Figure 3.20. It is worthwhile to note the apparent drop of the circulation close to the tip in case duct panels are not adapted with the blade tip. The circulation from the blade adapted grid on the duct appears to resemble more that due to the wall effect of the duct inner surface. Even though zero gap is assumed here, gap model can be implemented in the future as done by [S. H. Chang and Kinnas 2012].

When the repaneling process was firstly introduced by [H. Fan 2015], his method went through the two steps. In other words, two separate calculations were made without the interface which connects and interacts between those two runs. For the first step, neither the duct panels nor the duct wake panels were aligned to the blade wake, and the pitch of the duct panels was set to be the same as the blade pitch with full cosine panel spacing along the chordwise direction. The same spacing was also assumed to the duct wake. FWA was used to generate the fully aligned wake, and the aligned wake is saved for the next step, in which he solved the potential equation using PSF-2 type wake alignment scheme. Instead of using the simplified form of the blade wake from PSF-2, the wake he used in the second step was from the previously saved data in the first step. Pitch of the duct was assumed to be constant, and neither the blade panels nor the blade wake panels were adapted to the duct panels. Due to the panel mismatching between the blade and the duct inner side, circulation distribution on the blade showed the drop around the blade tip, similar to the result in Figure 3.20.

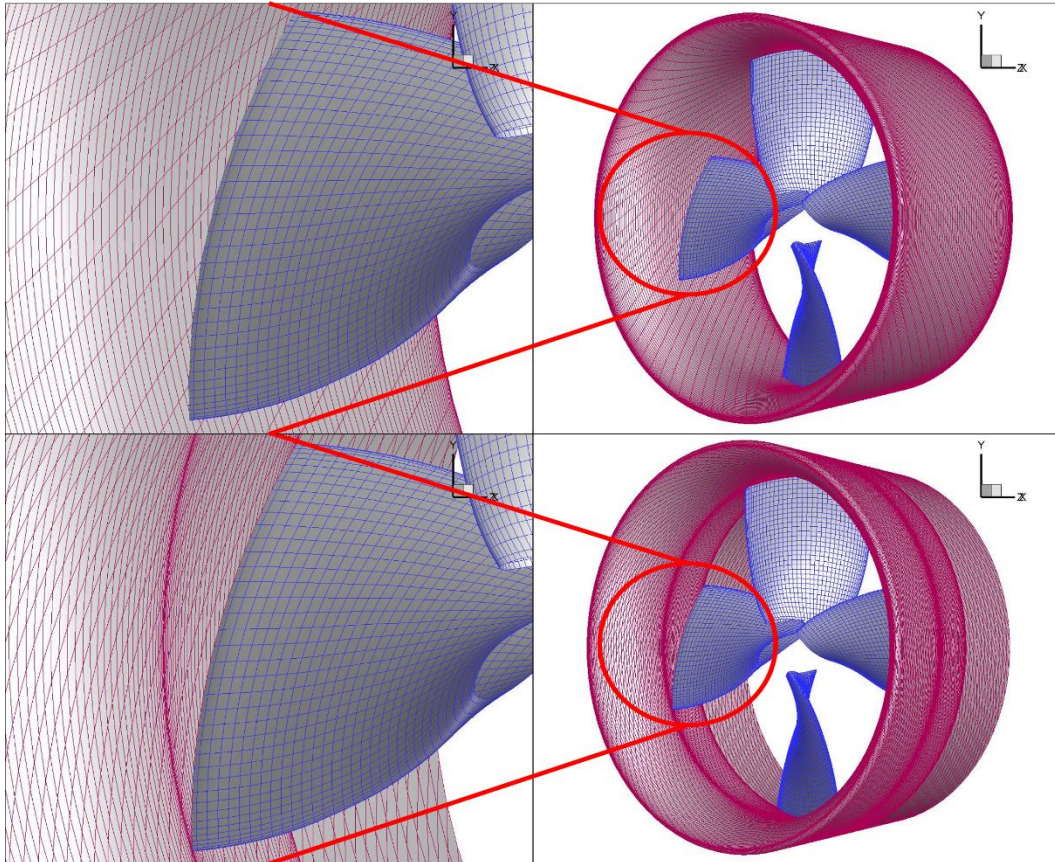


Figure 3.19 Panel distribution on the ducted propeller with square blade tip. Panels on the duct are adapted (lower) / not adapted (upper) with the blade tip.

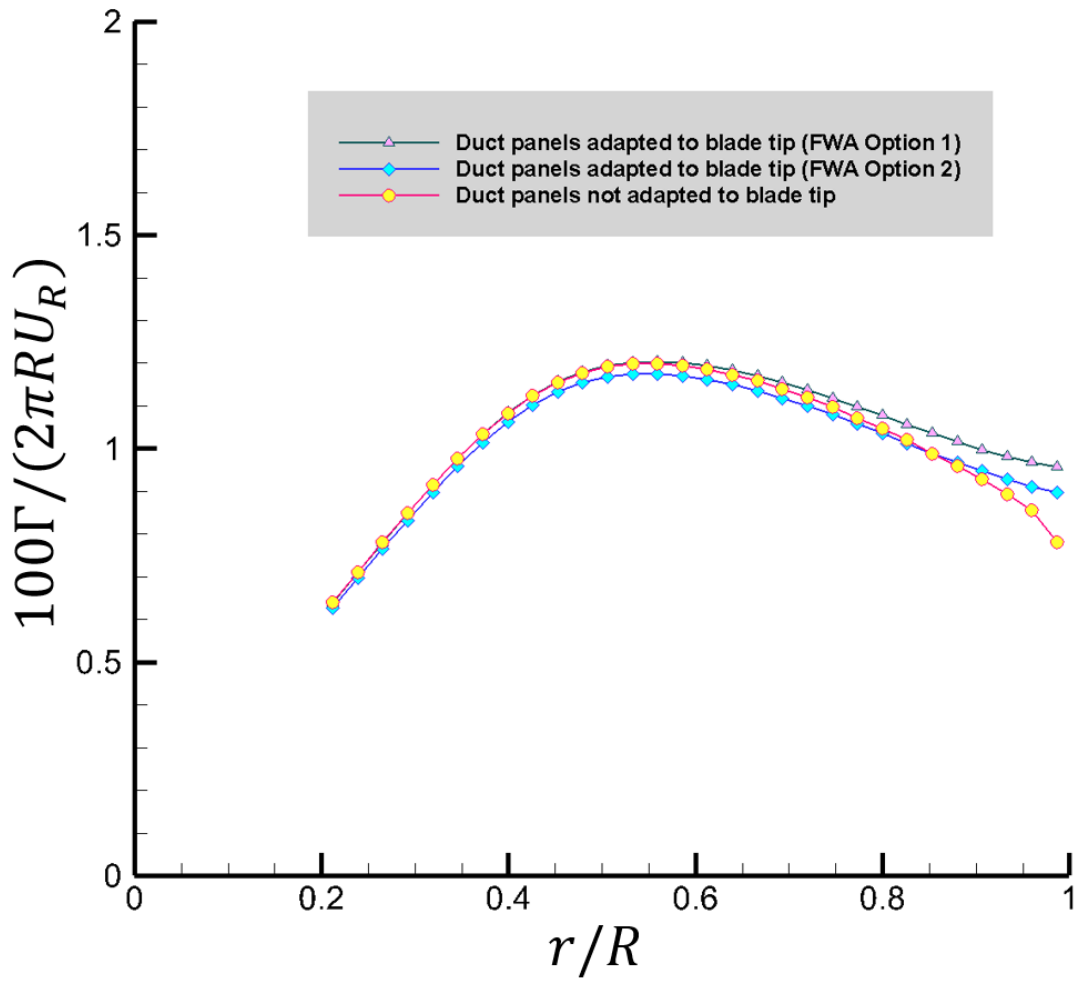


Figure 3.20 Circulation distribution over the square tip blade with duct panels adapted to blade tip and not adapted to blade tip. KA4-70 ducted propeller is used at the design advance ratio, $J_s=0.50$.

3.3 Duct Wake Alignment

In this section, FWA is applied to the duct wake in the same way of aligning the blade wake. Although the previous panel method has been improved for the prediction of the ducted propeller performance, the wake alignment scheme in the previous method was based on a cylindrical geometry of duct wake. Given that the free vortex sheets shed from the trailing edge of a duct are the material surface, which should be aligned based on the local flow velocity, the uniform shape of the duct wake was unnatural and somewhat artificial.

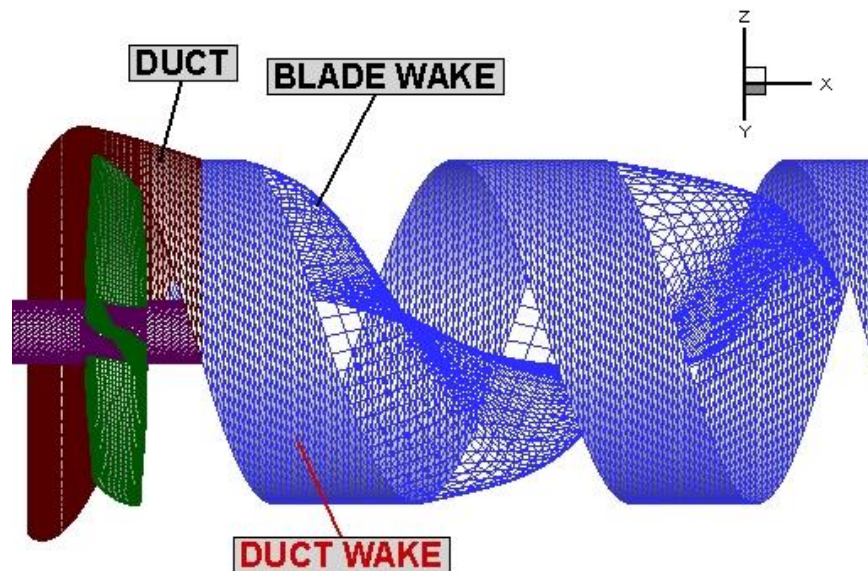


Figure 3.21 Geometry of the ducted propeller with cylindrical duct wake.

In this section, the wake sheets of the trailing vortex of the duct will be improved by aligning it with the local flow velocity as in the case of the blade wake. The results from RANS simulations will be presented in Chapter 4 for the correlations with those from the panel method. Also, in the

same chapter, the experimental measurements are also adopted for the validation of the predicted blade forces from the panel method.

3.3.1 Introduction

To properly predict the performance of the ducted propellers, a wake alignment scheme is also required to duct wake. Within the previous panel method, FWA has produced better performance of the ducted propeller compared to the other wake alignment model, such as PSF-2. However, the FWA, in the previous case, has only been applied to the blade wake. In other words, the effects of the duct wake on the blade wake were based on the uniform distribution of the duct wake. With the cylindrical distribution of the wake panels, physical behavior of the trailing vortex of the duct wake could not be well represented. Although the stiffened form of the duct wake has minor effects on the predicted results due to its interval from the blade where control points are located, blade wake after the trailing edge of the duct needs to be post processed to prevent penetrations between the blade wake and the duct wake. The penetration between the blade wake and duct wake before and after the post processing are presented in Figure 3.22 and 3.23.

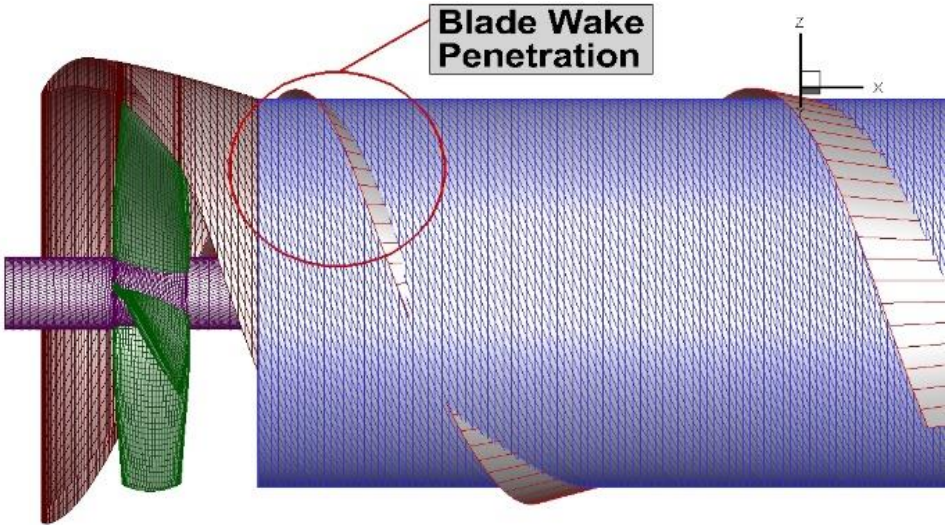


Figure 3.22 Penetration of the blade wake on the duct wake.

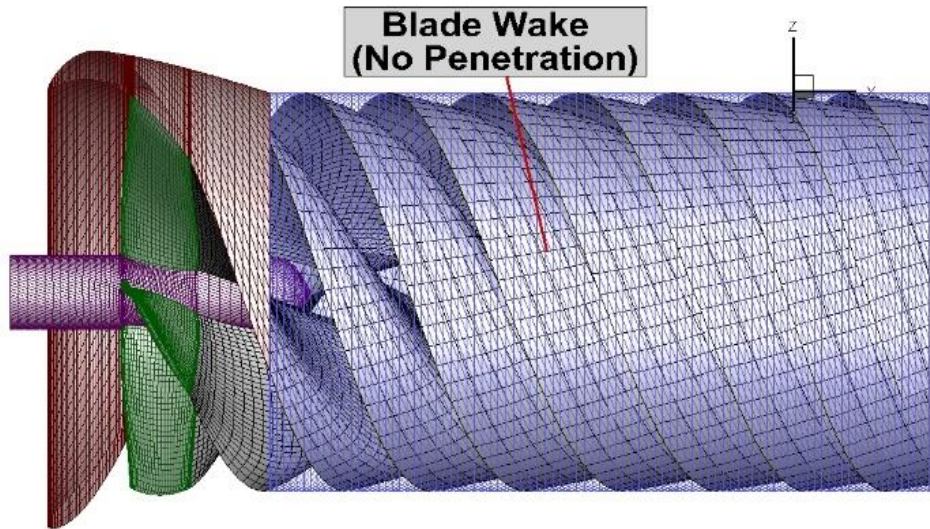


Figure 3.23 The paneling of the blade wake after resolving the problem of panel penetration.

Ideally, the wake sheets of the trailing vortex of the duct also need to be aligned with the local flow velocity same as the blade wake by considering the effects of the hub, blade/blade wake, duct, and duct wake itself. Therefore, the same algorithm of FWA in blade wake is also applied to duct wake within the framework of a low-order panel method. The numerical implementation of the alignment scheme is focused on the steady performance of duct wake.

3.3.2 Algorithm

Before aligning the duct wake, the effects of the blade, duct and blade wake on the duct wake are considered in terms of the induced velocity. The interactions between the blade wake and duct wake will cause the duct wake to curl near the tip of the blade wake. This curling will be more investigated with the results in Chapter 4. Since aligning duct wake is mainly affected by the blade wake due to the close distance between each other, duct wake alignment is conducted after the blade wake is generated at each iteration in FWA. Figure 3.25 describes the general flow chart of the FWA scheme in case the alignment on duct wake is included. Figure 3.24 describes the same

case, but the alignment on duct wake is not included. Note that when FWA is applied to both the blade wake and duct wake, only repaneling Option 2 is adopted to improve the convergence of the predicted results. Repaneling process on the duct wake is conducted such that the first strip of the duct wake sheet is forced to be aligned to the duct trailing edge, but the rest part of the duct wake sheet is determined by FWA.

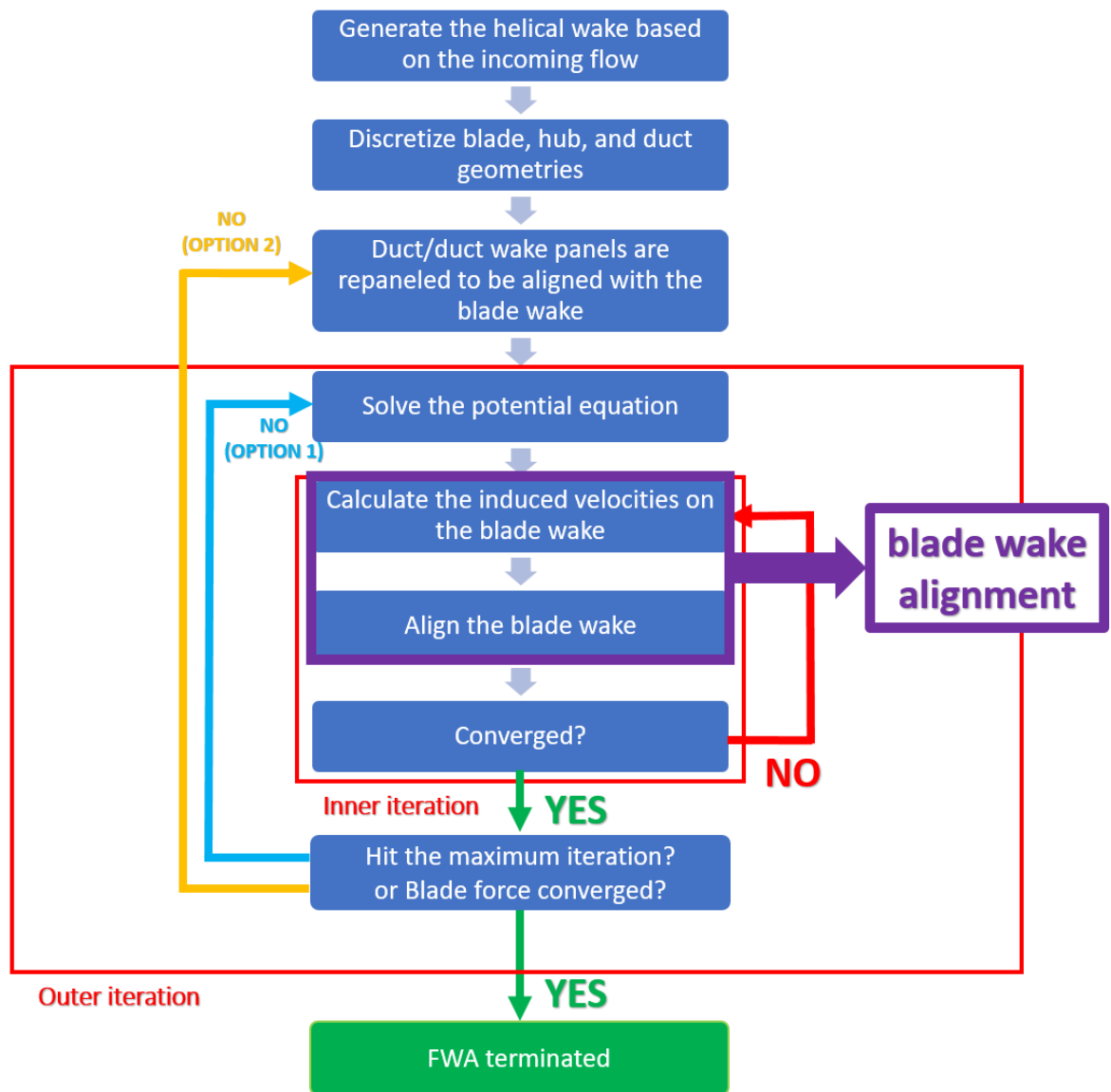


Figure 3.24 Flow chart of FWA without duct wake alignment.

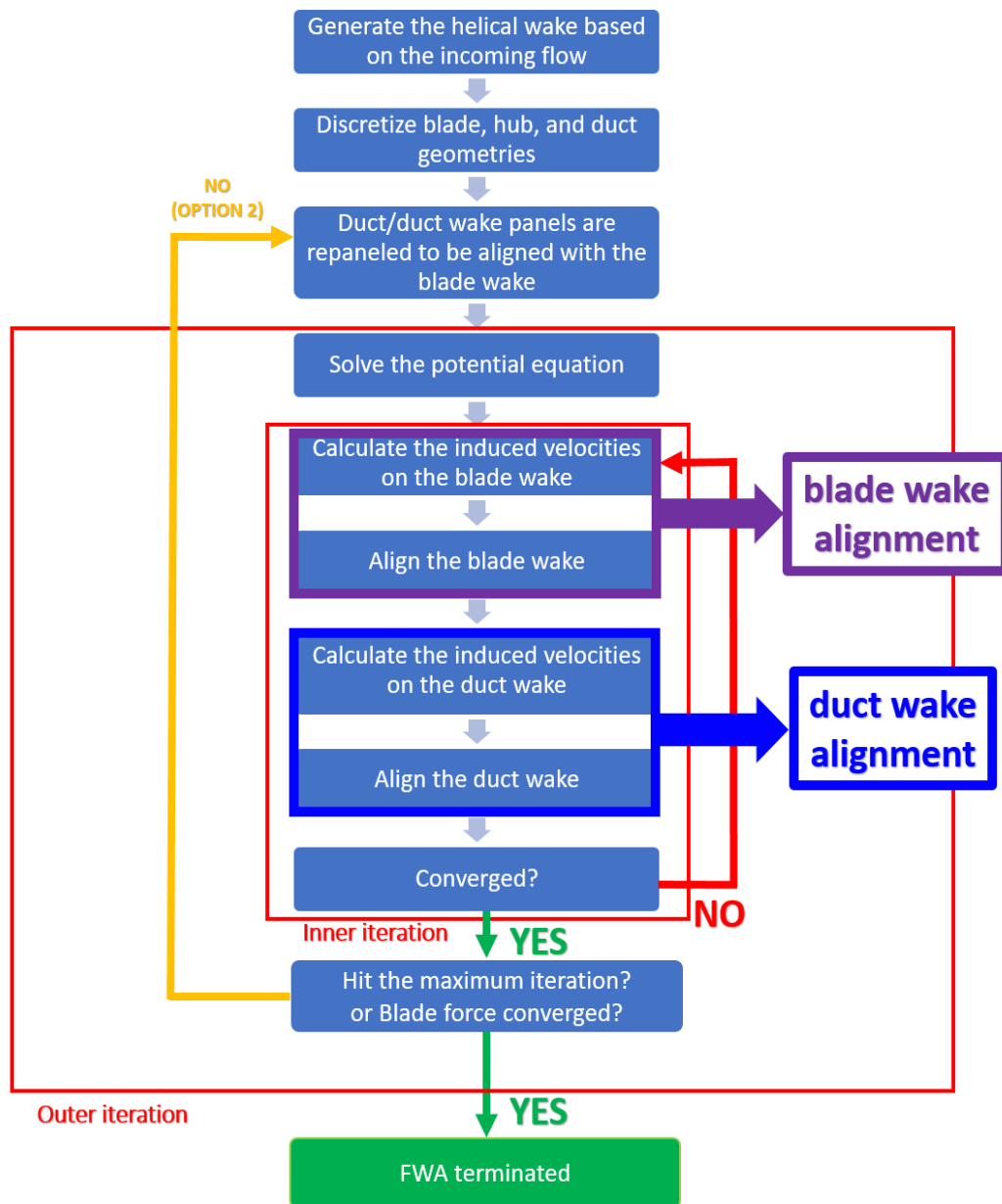


Figure 3.25 Flow chart of FWA with blade and duct wake alignment.

For each iteration, both the blade wake and the duct wake are aligned based on the wake geometries at the current iteration step, which means both wakes are affecting each other and being aligned at the same time step. It produces better correlation of their relative positions around the

tip of blade wake than the case which aligns both wakes based on the wake geometries from the previous time step.

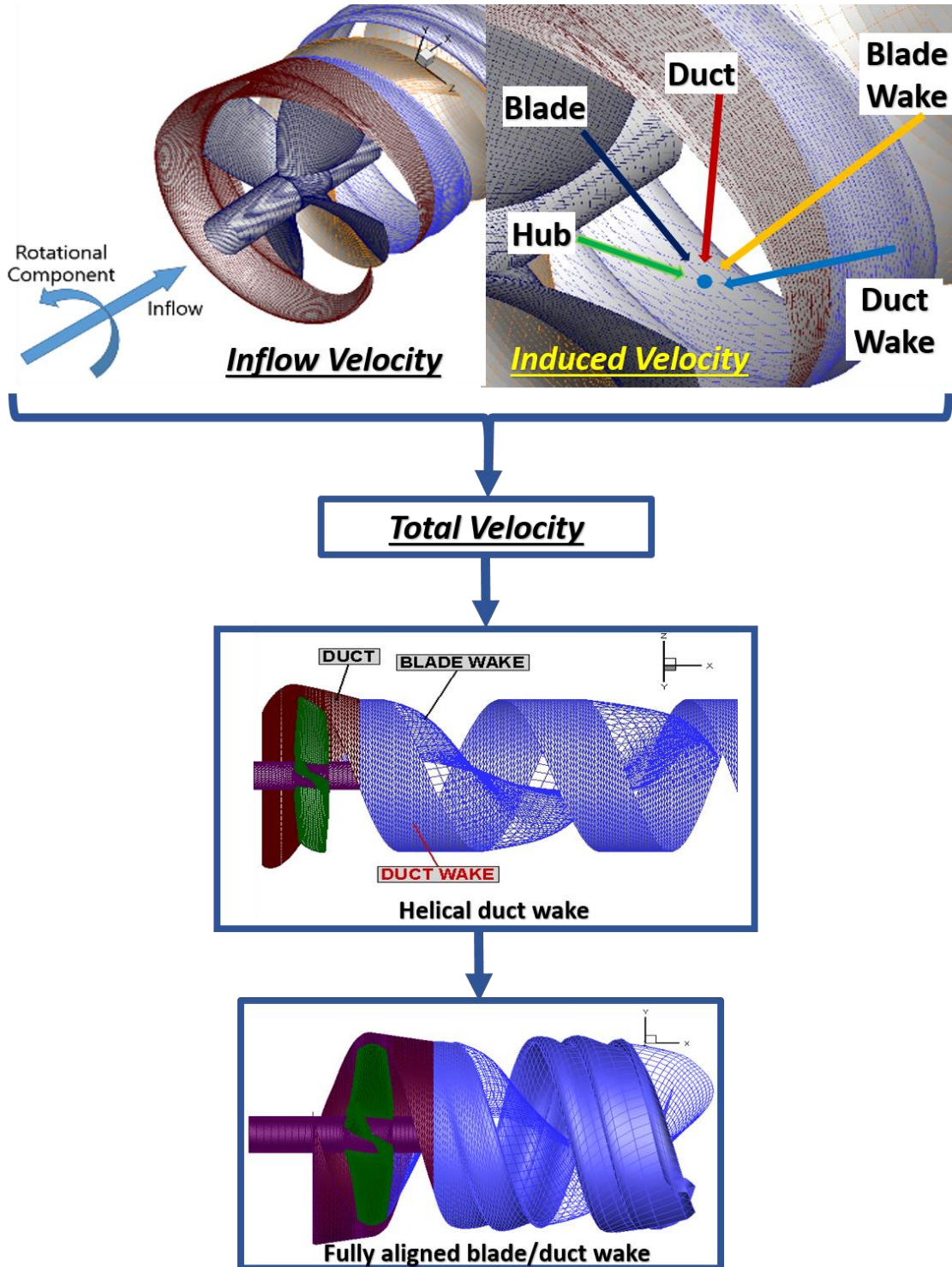


Figure 3.26 Flow chart of duct wake alignment using FWA.

3.3.3 Numerical Results

In the panel method, vortex shed from both the duct and the blade trailing edge is represented by the distribution of the wake panels. Since the planar panels cannot represent the diffusion effects of the shedding vortex in the panel method, the diffused shedding vortex will be replaced by the concentrated vortex. Then, the concentrated vortex will be placed on the wake panels, which are to be distributed based on the local flow velocity by FWA.

Since FWA is based on the iterative method, it will take several iterations for the aligned wake to reach fully converged shape. Figure 3.27 presents the convergence history of the wake panels during the wake alignment scheme applied on both the duct wake and the blade wake in the design advance ratio of 0.50. Two-dimensional plots based on the planes cutting through the center of propeller geometry are also presented to show the detailed distribution of the wake panels during the iterations in FWA.

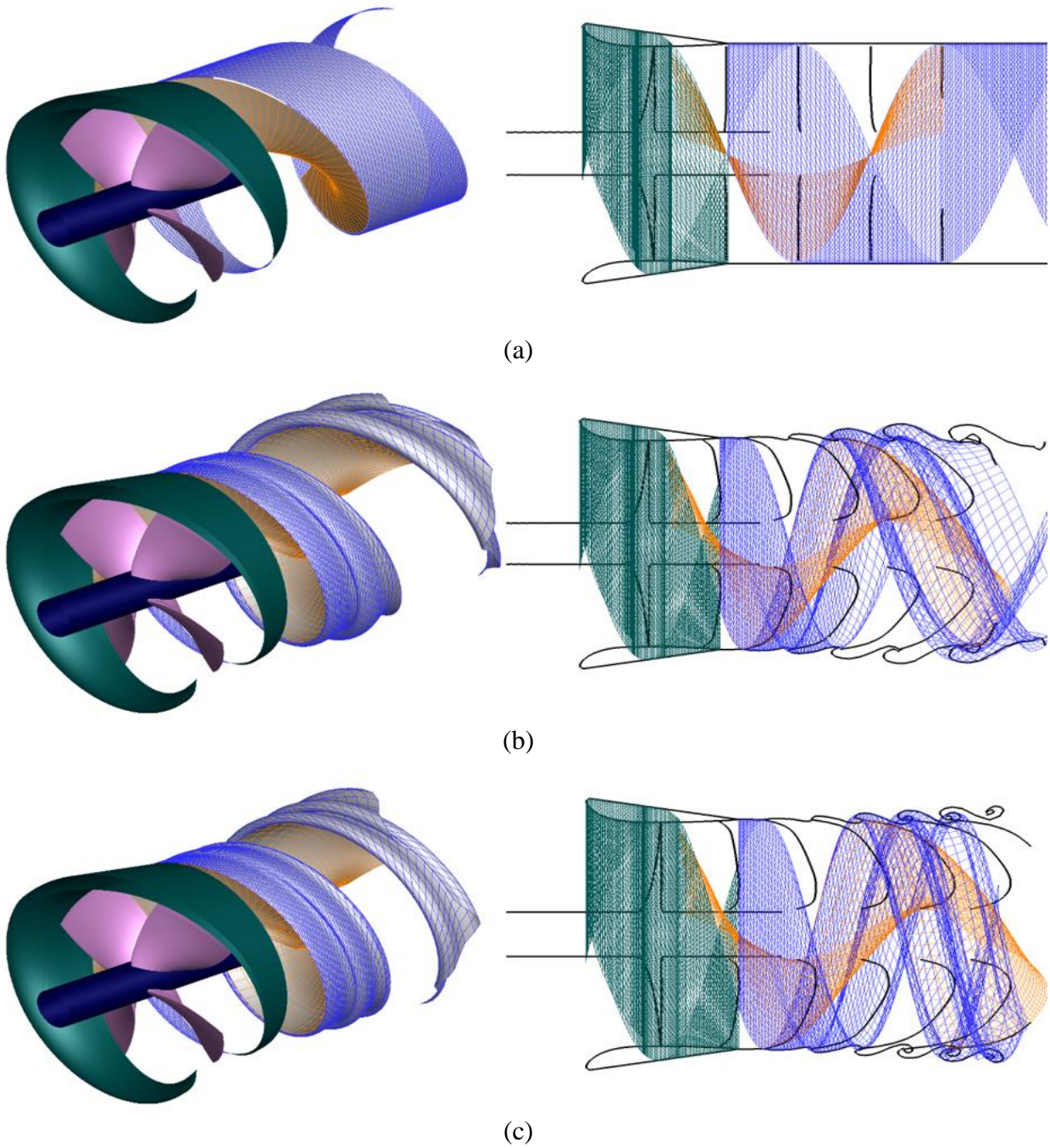


Figure 3.27 Convergence history of the full wake alignment scheme applied to both the blade wake and the duct wake (only part of the propeller geometry is shown for clarity) at the (a) 1st, (b) 5th, and (c) last iteration out of 30 loops. Black solid lines on the right column figures mean the concentrated shedding vortex without diffusion effect in the panel method. KA4-70 ducted propeller is used at the design advance ratio, $J_s=0.50$.

As it can be seen from the figures above, FWA starts its first iteration based on the helical and cylindrical shapes for the blade wake and duct wake, respectively. Then, the iteration will continue until the wake reaches its converged shape based on the predefined convergence criteria. The correlation of the wake distributions between the results from the panel method and RANS simulations are shown in Chapter 4.

3.4 Unsteady Wake Alignment

3.4.1 Introduction

The topic of this section begins with a question on the limitation of steady wake alignment. Steady wake alignment scheme is a quite appropriate option for the cases in axisymmetric inflow due to its fast and stable calculations. However, in the case of unsteady flow such as the inclined shaft flow or even more general effective wake, unsteady wake alignment scheme is required to take into account the variation of incoming flow with time. Although steady wake alignment scheme can also be used for unsteady problems, it turned out to be too time-consuming to apply steady scheme to all the time steps of unsteady simulation. Considering that one revolution consists of 60-time steps (in most cases), and an unsteady problem needs to be calculated through several revolutions until reaching the converged results, calculating time might become a severe numerical problem. Therefore, a new alignment scheme, which is oriented to the unsteady problem, needs to be developed for the panel method to go beyond the time independent problem.

The hub effect on wake panels will be discussed not only in uniform flow but also in the inclined flow. As the wall effect of the duct to the outer edge of wake panels, hub geometry is also supposed to have the same effect to the wake near the hub. From uniform flow, which is relatively

free from the interaction between the wake and hub, focus of this section will be shifted into the penetration issue between the wake and hub in the inclined flow.

3.4.2 Basic Algorithm

In this section, a summary of unsteady wake alignment model, introduced by [H. Lee 2002] is made. Several assumptions in his work have been modified to account for FWA in unsteady state. The basic algorithm of potential flow assumptions in inviscid and irrotational flow will be revisited to derive the induced velocity on the wake surface. Then, the numerical method, which is implemented to compute the aligned wake geometry will be introduced in a progressive manner. The basic philosophy behind steady alignment model is also valid in unsteady state except for the consideration of time dependent variables.

Consider a propeller subject to a non-axisymmetric inflow $\vec{U}_{eff}(x, r, \theta)$, which is assumed to be the effective wake including the interaction of the vorticity with the propeller. When the propeller rotates at a constant angular velocity, $\vec{\omega}$, the total velocity relative to the propeller becomes

$$\vec{U}_{in}(x, y, z, t) = \vec{U}_{eff}(x, r, \theta - \omega t) + \vec{\omega} \times \vec{x}(x, y, z) \quad (3.14)$$

where $r = \sqrt{(y^2 + z^2)}$ and $\theta = \tan^{-1}\left(\frac{z}{y}\right)$.

The modeled propeller geometry in Cartesian coordinate system is shown in Figure 3.28, adjusted from Figure 2.19 of [H. Lee 2002]. Although the conical bulb and the cylindrical tip vortex (S_T) are presented in the figure, those tip vortex geometries are not considered in this study.

It is because the main emphasis of this section is on the wake alignment model than the effect of the tip vortex on the propeller performance.

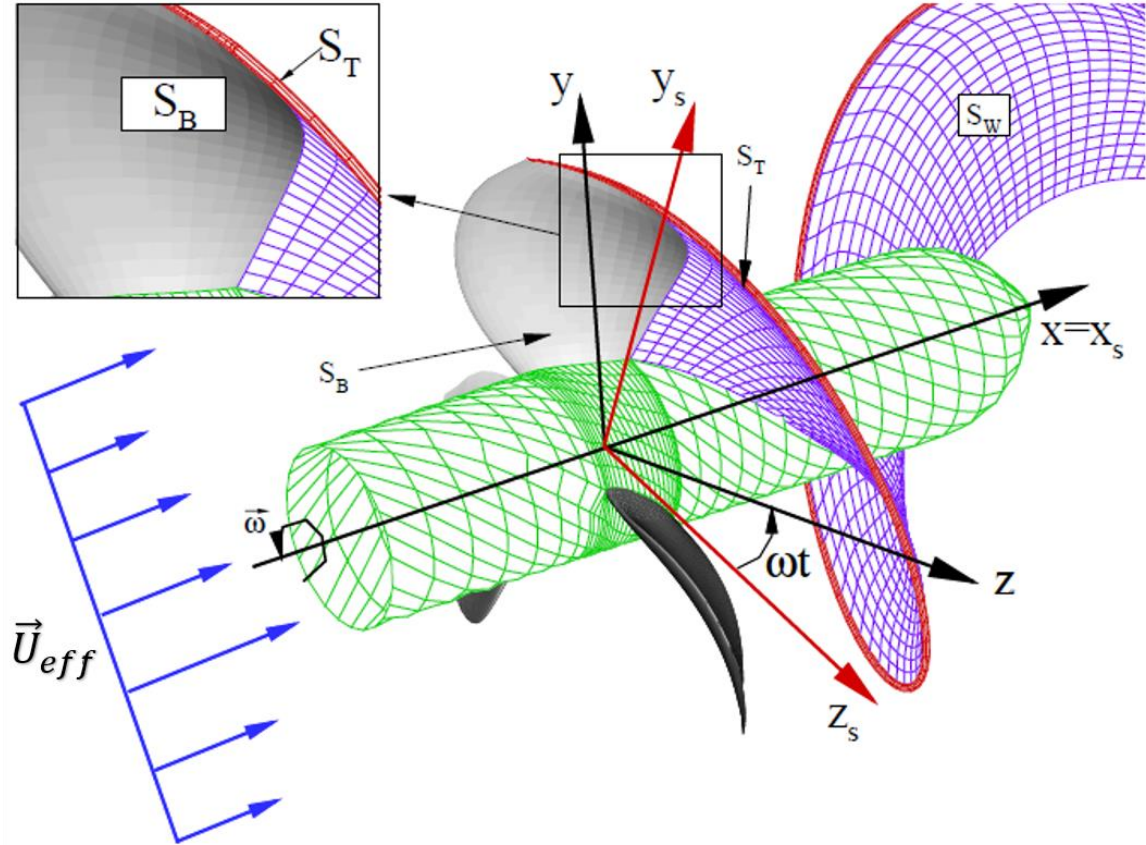


Figure 3.28 Propeller subject to a general inflow, assumed to be effective wake. (x, y, z) and (x_s, y_s, z_s) denote the propeller fixed and the ship fixed coordinates respectively. This figure is adjusted from Figure 2.19 of [H. Lee 2002].

The potential ϕ_p at an arbitrary point, p , on the discretized propeller geometry at time t can be expressed by the Green's third identity.

$$\begin{aligned}
 2\pi\phi_p(t) = & \iint_{S_B} \left[\phi_q(t) \frac{\partial}{\partial n_q(t)} \left(\frac{1}{R(p; q)} \right) - \frac{\partial \phi_q(t)}{\partial n_q(t)} \left(\frac{1}{R(p; q)} \right) \right] dS \\
 & + \iint_{S_w} \Delta \phi_w(r_q, \theta_q, t) \frac{\partial}{\partial n_q(t)} \left(\frac{1}{R(p; q)} \right) dS
 \end{aligned} \tag{3.15}$$

where ϕ_q denotes the potential at the variant point q , which has the distance $R(p; q)$ between the field point p . n_q denote the unit normal vector at point q pointing out of fully wetted propeller surface S_B , and $\Delta\phi_w$ is the potential jump across the wake surface S_w .

Equation (3.15) states that the perturbation potential ϕ_p at time t on the propeller surface can be expressed as the superposition of the potentials due to source and dipole distributions on the propeller, and due to dipoles on the wake. From the kinematic boundary condition, which means the flow must be tangent to the propeller surface, the source strength can be determined as follows:

$$\frac{\partial\Phi}{\partial n} = \frac{\partial\phi}{\partial n} + \vec{U}_{in} \cdot \vec{n} = \vec{n} \cdot \nabla\Phi = 0 ; \text{ on propeller surface} \quad (3.16)$$

where Φ is the total velocity potential, and \vec{n} is the normal vector on the propeller surface pointing into the fluid domain. Therefore,

$$\frac{\partial\phi}{\partial n} = -\vec{U}_{in} \cdot \vec{n} \quad (3.17)$$

From the Kutta condition,

$$\nabla\phi = \text{finite} ; \text{ at the trailing edge of blade} \quad (3.18)$$

Equation (3.18) can be proved that reduces to Morino's condition [Morino and Kuo 1974]:

$$\Delta\phi_w = \phi^+ - \phi^- \quad (3.19)$$

where ϕ^+ and ϕ^- mean the velocity potentials on the suction and the pressure side of the blade trailing edge respectively and are known by solving Equation (3.15).

Different from steady state, the dipoles on the wake are convected along the wake surface with angular velocity $\vec{\omega}$ to satisfy the force free condition on the wake surface [Kinnas and Hsin 1992]. In steady state, the trailing wake strength $\Delta\phi_w$ is constant along the circumferential direction and time invariant, but $\Delta\phi_w$ in unsteady state behaves as a function of the r and θ directions of the blade trailing edge in the cylindrical coordinates. Figure 3.29 through Figure 3.34 show the convection of the trailing wake strength in steady and unsteady state, respectively. Note that only 5 panels are used to represent the blade in spanwise direction for clarity.

$t = 0$

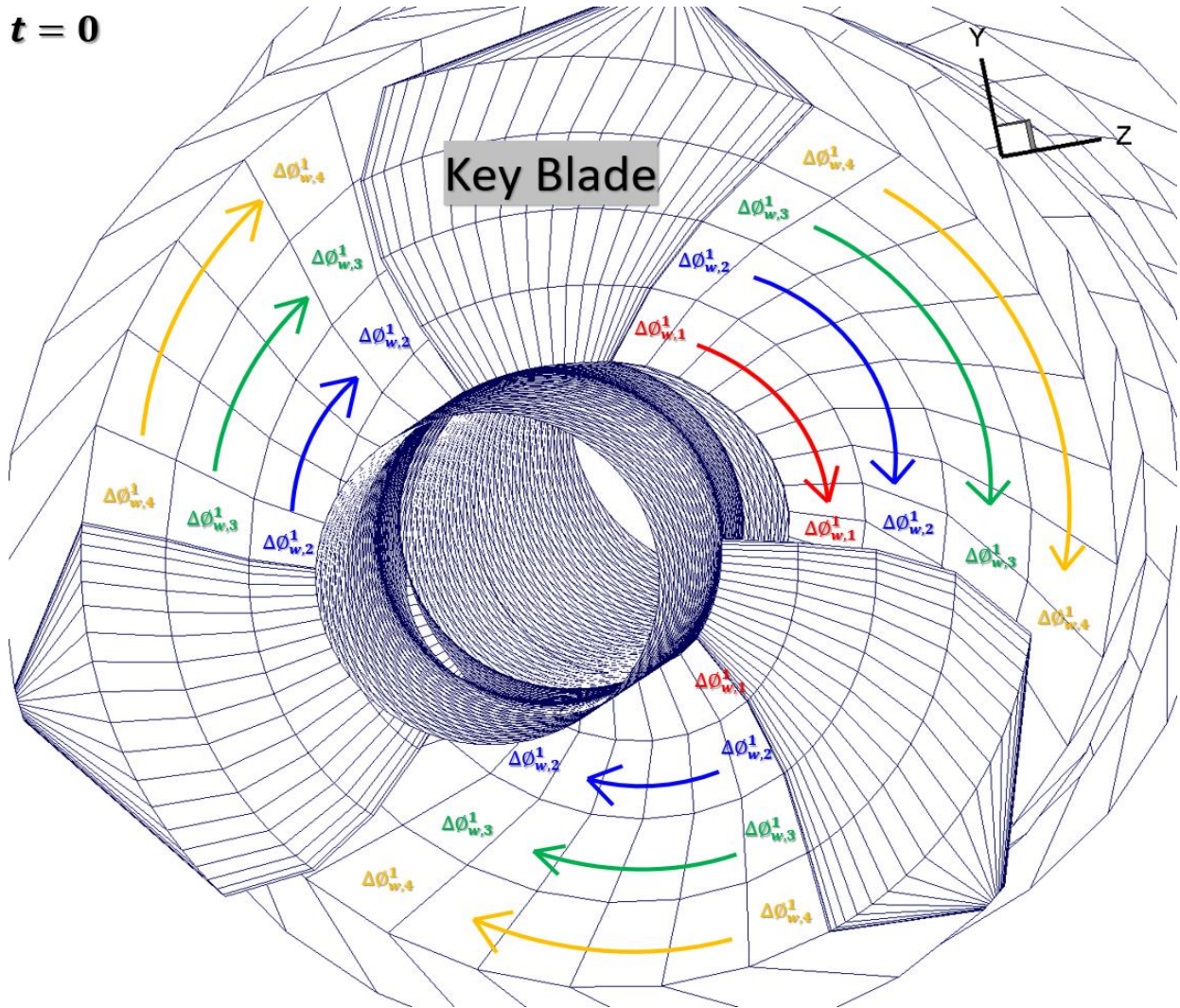


Figure 3.29 Convection of the trailing wake strength in steady mode ($t = 0$) at the first iteration. Where $\Delta\phi_{w,1}^2$ means the trailing wake strength on the 1st layer of the wake sheet from the hub at the 2nd iteration, for example. Different color means different strength.

$t = 0$

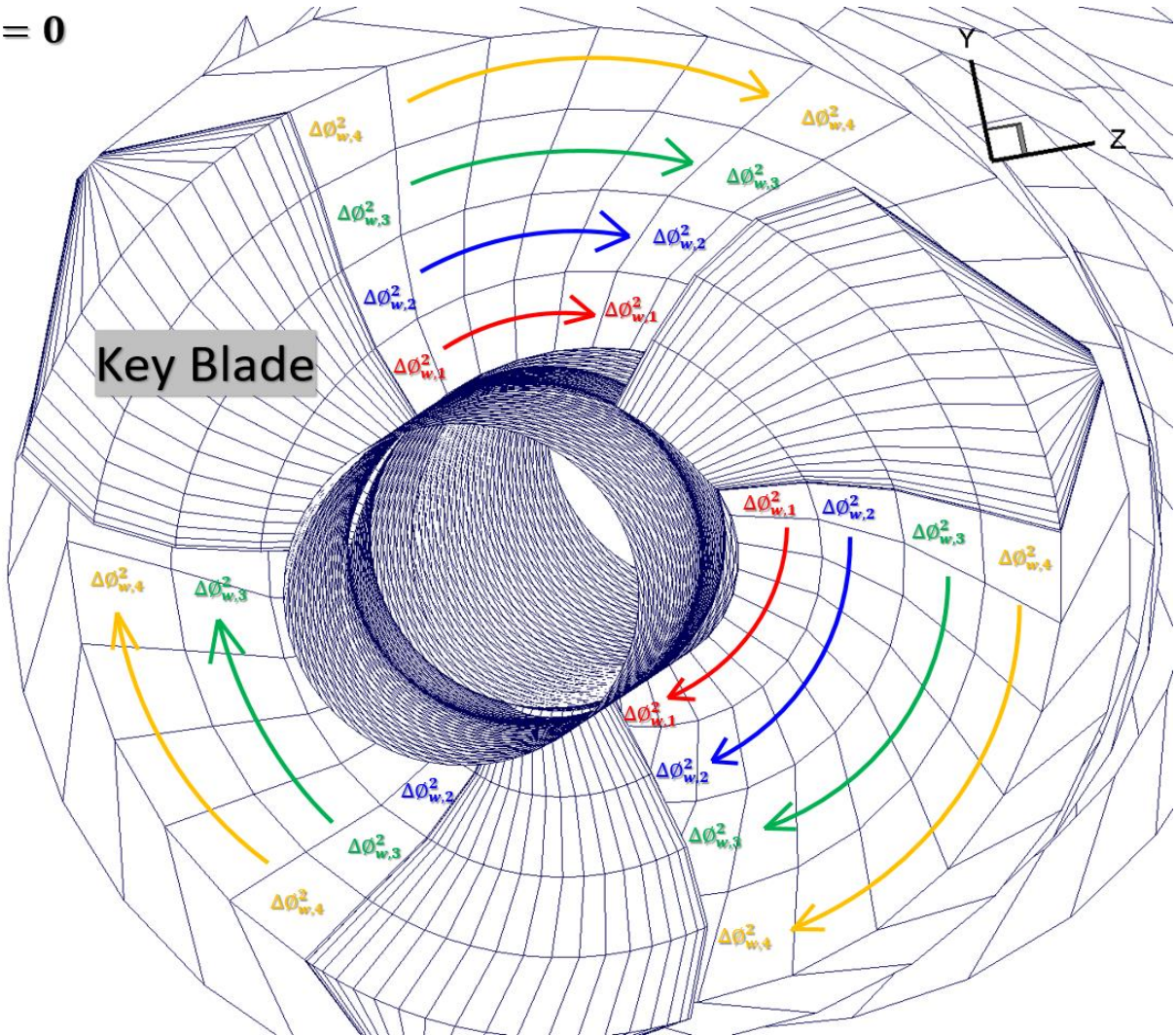


Figure 3.30 Convection of the trailing wake strength in steady mode ($t = 0$) at the second iteration. Where $\Delta\phi_{w,1}^2$ means the trailing wake strength on the 1st layer of the wake sheet from the hub at the 2nd iteration, for example. Different color means different strength.

$t = 0$

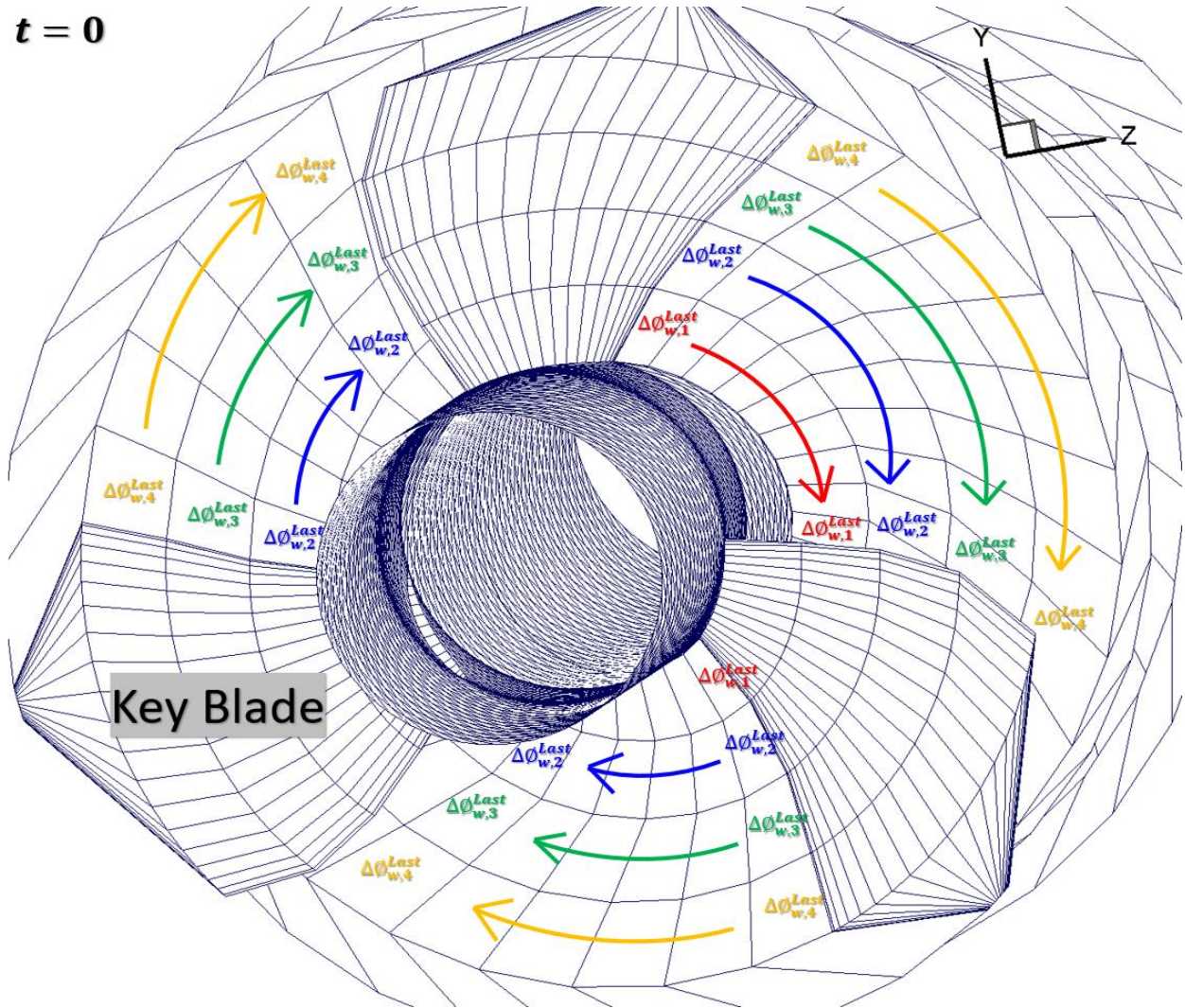


Figure 3.31 Convection of the trailing wake strength in steady mode ($t = 0$) at the last iteration. Where $\Delta\phi_{w,1}^2$ means the trailing wake strength on the 1st layer of the wake sheet from the hub at the 2nd iteration, for example. Different color means different strength.

$t = \delta t$

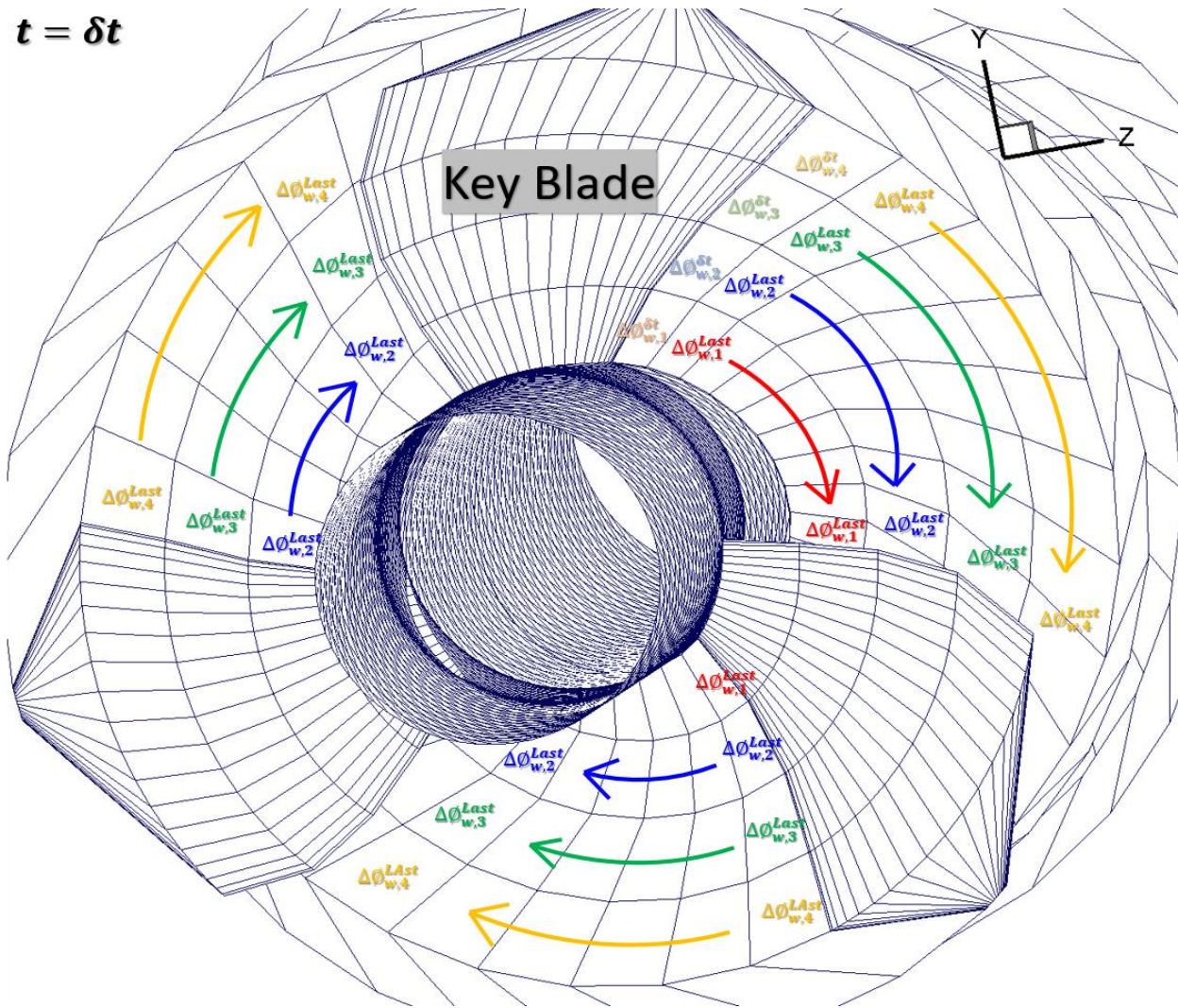


Figure 3.32 Convection of the trailing wake strength in unsteady mode at time step $t = \delta t$. Where $\Delta\phi_{w,1}^{\delta t}$ means the trailing wake strength on the 1st layer of the wake sheet from the hub at time step $t = \delta t$, for example. Different color means different strength.

$t = 2\delta t$

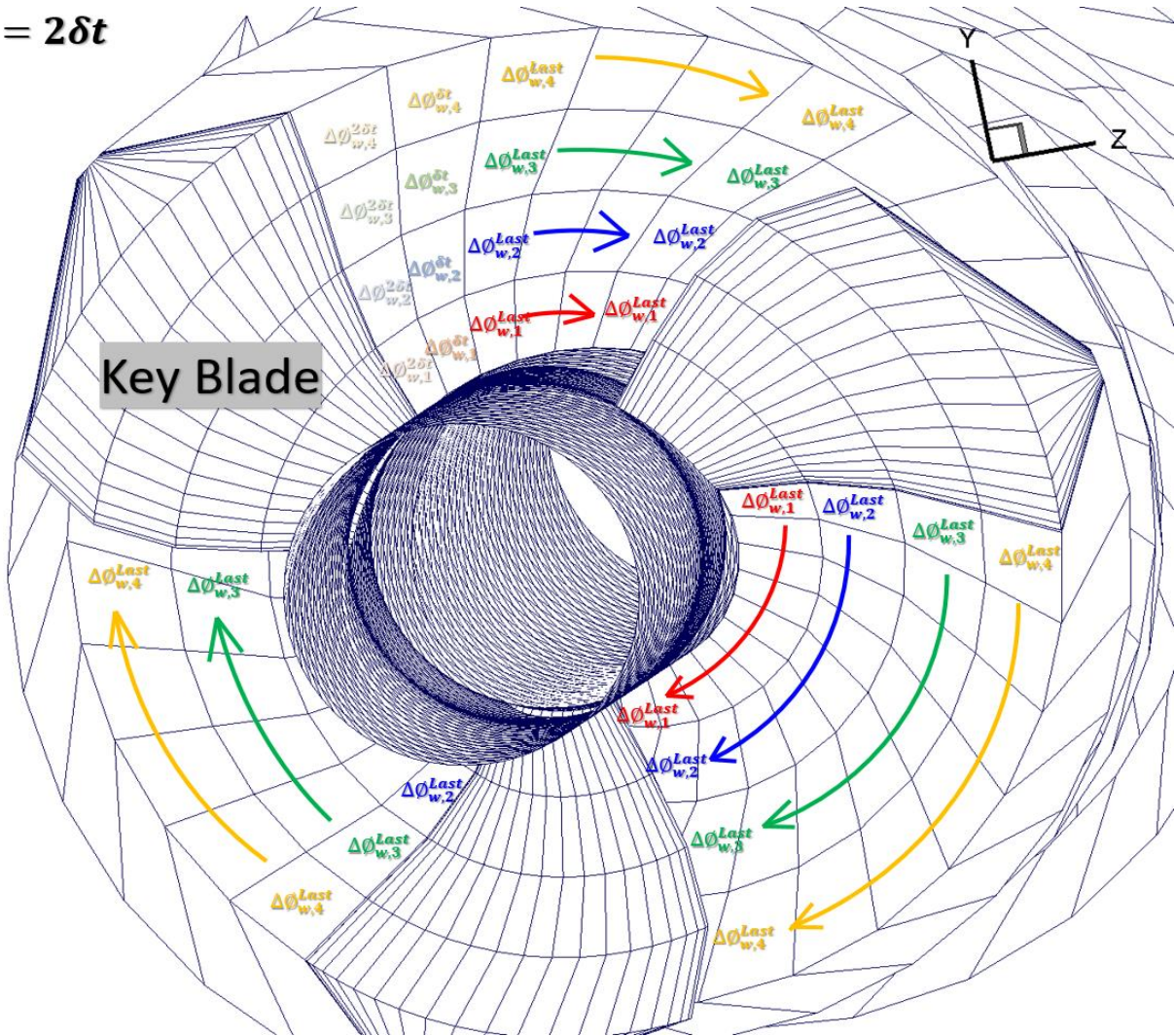


Figure 3.33 Convection of the trailing wake strength in unsteady mode at time step $t = 2\delta t$. Where $\Delta\phi_{w,1}^{\delta t}$ means the trailing wake strength on the 1st layer of the wake sheet from the hub at time step $t = \delta t$, for example. Different color means different strength.

$t = 3\delta t$

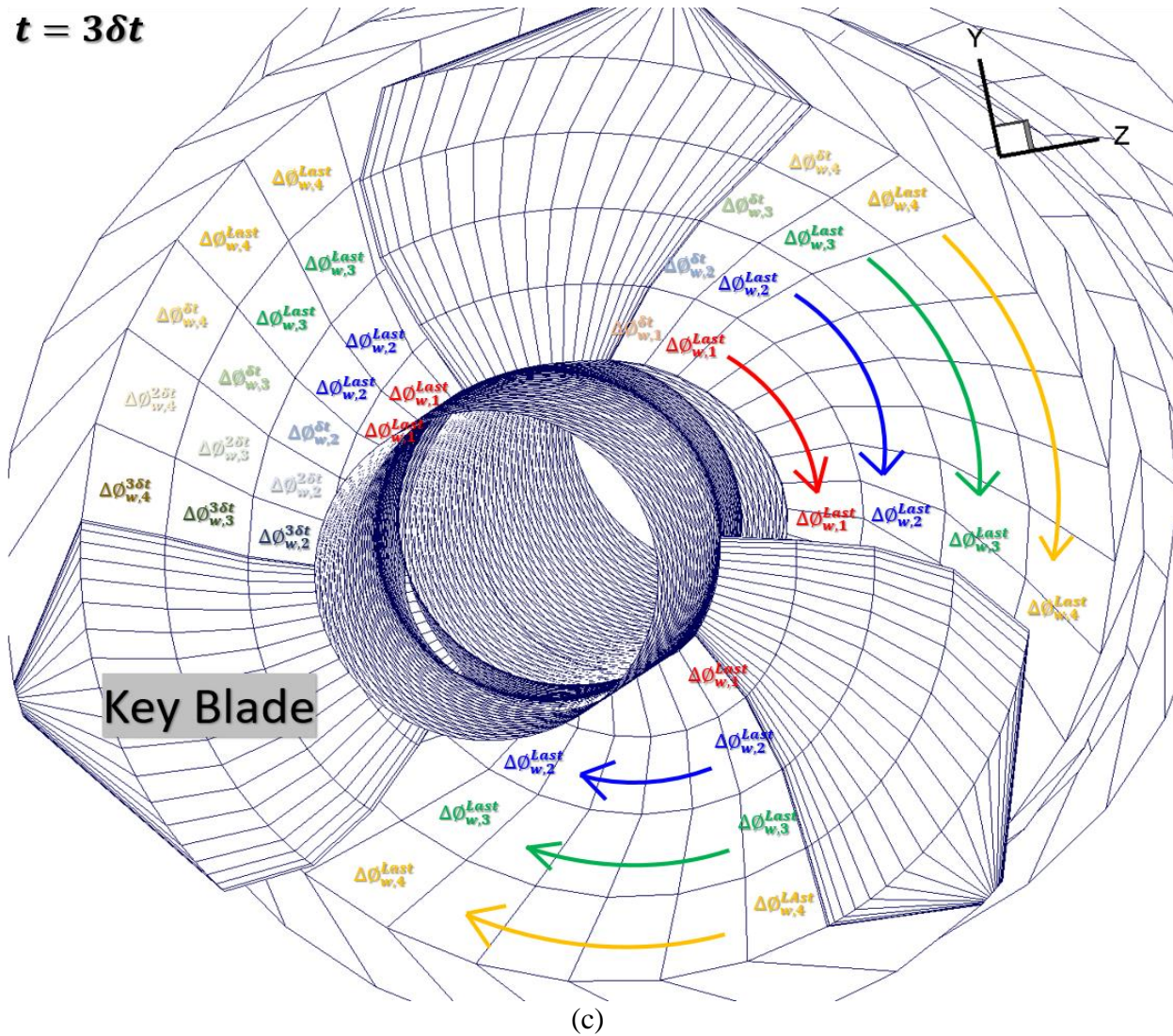


Figure 3.34 Convection of the trailing wake strength in unsteady mode at time step $t = 3\delta t$. Where $\Delta\phi_{w,1}^{\delta t}$ means the trailing wake strength on the 1st layer of the wake sheet from the hub at time step $t = \delta t$, for example. Different color means different strength.

Once the velocity potentials are determined by solving Equation (3.15), the dipole strength ($\phi_q(t)$) and the source strengths ($\frac{\partial\phi_q(t)}{\partial n_q(t)}$) on the propeller surface are known. the perturbation velocity on the wake panels at time step t can be calculated from the Green's formula by taking the gradient of Equation (3.15). Note the time and space dependency of the dipole strength on each strip on the wake surface in Equation (3.16).

$$\begin{aligned}\vec{u}_i(t) = & \frac{1}{4\pi} \iint_{S_B} \left[\phi_q(t) \nabla \frac{\partial}{\partial n_q(t)} \left(\frac{1}{R(p; q)} \right) - \frac{\partial \phi_q(t)}{\partial n_q(t)} \nabla \left(\frac{1}{R(p; q)} \right) \right] dS \\ & + \frac{1}{4\pi} \iint_{S_w} \Delta \phi_w(r_q, \theta_q, t) \nabla \frac{\partial}{\partial n_q(t)} \left(\frac{1}{R(p; q)} \right) dS\end{aligned}\quad (3.20)$$

The total velocity ($\vec{V}_{total}(x, y, z, t)$) induced on the wake surface is the sum of the inflow velocity, $\vec{U}_{in}(x, y, z, t)$, and the perturbation velocity, $\vec{u}_i(x, y, z, t)$.

$$\vec{V}_{total}(x, y, z, t) = \vec{U}_{in}(x, y, z, t) + \vec{u}_i(x, y, z, t) \quad (3.21)$$

Based on the total velocity, the unsteady wake alignment model implements the following algorithm to align the wake panels in unsteady state.

❖ *MODE 1: steady alignment mode ($t = 0$)*

1. Solve the steady Boundary Value Problem (BVP) using PSF-2 wake alignment model, which considers the induced velocity from the propeller and the contraction of the transitional wake.
2. Calculate the induced velocities on the wake surface based on the BVP solutions, which are already known by solving Equation (3.15). The effects of blade, hub, and wake itself are considered in terms of the perturbation velocity.
3. Calculate the inflow velocities at the same nodal points on the wake surface as step 2 by considering only the zeroth harmonic coefficients of the effective wake. The circumferential variation of the effective wake is expressed in terms of the harmonic coefficients. The inflow velocity is added up to the perturbation velocity from step 2 to calculate the total velocity.

4. The full wake alignment model, discussed in Section 3.1 is implemented to find the fully aligned wake coordinates using the total velocities. The time step size, δt , of the shedding vortex is determined using the angular velocity (radian per unit time) of propeller and the angular increment of the discretized wake sheet, $\delta\theta$.

$$\delta t = \frac{\delta\theta}{\omega} = \frac{\delta\theta}{2\pi n} \quad (3.22)$$

5. Solve the BVP again to update the solutions by using the newly aligned wake from step 4. Once the BVP solved, steps from 2 to 4 are implemented again. This process is repeated until the difference of the wake geometries between the two consecutive iterations falls below the previously defined criterion.

6. Save the converged wake geometry and the BVP solutions from the last iteration, with which the unsteady alignment mode starts its first iteration as follows.

❖ *MODE 2: unsteady alignment mode ($t \geq 0$)*

1. Set the wake from the last iteration of steady alignment mode as the initial wake for all time step locations.

2. Solve the unsteady BVP and update the solutions at the current time step location. Solutions are solved only for the key blade.

3. Calculate the induced velocities on the key wake based on the updated BVP solutions. The effects of all blades, their wakes, and hub are considered in terms of the perturbation velocities.

4. Calculate the inflow velocities on the key wake. All the harmonic coefficients are considered to account for the circumferential variation of the effective wake. Then, the induced velocities are added up to the inflow velocities to calculate the total velocities.

5. Find the locations of wake sheet by aligning it with the total velocity. The FWA is *not* implemented in unsteady alignment mode, although it can be used for the unsteady problems.

Instead, the new coordinates at n th strip are determined in a manner of trapezoidal rule:

$$\begin{aligned}
 x_n &= x_{n-1} + \frac{1}{2} (\vec{V}_x^{n-1} + \vec{V}_x^n) \cdot \delta t \\
 y_n &= y_{n-1} + \frac{1}{2} (\vec{V}_y^{n-1} + \vec{V}_y^n) \cdot \delta t \\
 z_n &= z_{n-1} + \frac{1}{2} (\vec{V}_z^{n-1} + \vec{V}_z^n) \cdot \delta t
 \end{aligned} \tag{3.23}$$

where \vec{V}_x^n , \vec{V}_y^n , and \vec{V}_z^n are the total velocities in the x , y , and z directions respectively at the n th strip of the wake sheet in Cartesian coordinate system.

6. Update the key wake and save it at the current time step location. The saved wake will be used at the later time step when any of the blades including the key blade is located at the saved location.

7. Solve the BVP problem with the updated key wake. Update and save the trailing wake strength $\Delta\phi_w(t)$ of the key wake and the dipole strength $\phi(t)$ on the key blade at the current time step location (Figure 3.32 through 3.34).

8. Advance to the next time step ($t + \delta t$) and update the wake geometries of all blades from the previously saved data. The trailing wake strength $\Delta\phi_w(t + \delta t)$, and the dipole strength $\phi(t + \delta t)$

of the other blades (excluding the key blade and its wake) are also updated from the previously saved data.

9. Repeat from step 2 to step 8 until the key wake geometries at all time step locations converge.

❖ *MODE 3: fully unsteady mode ($t \geq 0$):* this mode does not perform wake alignment, but uses the aligned wake geometry from the unsteady alignment mode.

1. Update the wake geometries, which correspond to the time step t , of all blades from the saved results in the previous mode.

2. Update $\Delta\phi_w(t)$ and $\phi(t)$ of the other wakes and blades at the time step t .

3. Solve BVP for the solutions on the key blade and update $\Delta\phi_w(t)$ and $\phi(t)$.

4. Advance to the next time step ($t + \delta t$) and repeat from step 1 until the last revolution.

To obtain the converged propeller performance, the unsteady alignment mode is repeated up to 2 revolutions, and the fully unsteady mode is solved at least up to 4 revolutions.

Chapter 4

Application to Ducted Propeller

4.1 Ducted Propeller with Square Blade Tip and Sharp Trailing Edge Duct

In this section, FWA is applied to a square-tip ducted propeller to investigate the effects of the blade wake on the predicted propeller performance. For this application, KA4-70 ducted propeller (Figure 3.8) is adopted. The design advance ratio of this propeller is $J_s=0.5$ and zero gap is assumed between the duct inner side and the blade tip. As shown in Figure 4.4, velocity vectors are plotted on the blade/duct wake to visualize the total velocity vectors induced at each nodal point. This visual checking is done based on the assumption that the velocity vectors are the local flow velocity with which the wake panels are supposed to be aligned. Also, the magnitude of the cross products between the vortex segment and the velocity vector is calculated to check the validity of FWA in a numerical way. The better wake panels are aligned to the local velocities, the closer the magnitude of cross products approaches to zero with iterations in FWA.

The predicted force performance from the panel method are compared with the results from the experiments, done by MARIN [Bosschers 2008]. Also, the results from panel method with the two repaneling options are compared with those from full-blown RANS simulations and the experiments for a range of the advance ratios from $J_s=0.3$ to $J_s=0.7$. The effect of the repaneling options to the convergence history of the blade forces, particularly at the low advance ratio is investigated.

Toward the end, the emphasis of this chapter is shifted to the distribution of the wake panels behind the duct and blade trailing edge. As mentioned in the earlier section, wake panels represent

the concentrated shedding vortex behind the trailing edge of the blade and duct. These are intensively correlated with the two-dimensional plots of the vortex magnitude from full-blown RANS simulations.

4.1.1 Lower Order Panel Method

To discretize the propeller geometry, 60×20 (chordwise\timesspanwise) panels are used for the blade and 160×20 (chordwise\timescircumferential) panels are used for the duct geometry, respectively. Convergence study of the blade forces with different panels numbers are also conducted and the corresponding results are shown in Figure 4.1. As shown, panel method is invariant of the number of panels that are used to discretize the ducted propeller. The infinite hub is assumed, and the radius of the hub is set to be the same as the inner most radius of the blade. For the blade/duct wake, panel numbers are equal to the spanwise and circumferential panel numbers of the blade and duct respectively. The wake geometries are generated for the advance ratios ranging from $J_s=0.3$ to $J_s=0.7$ as shown in Figure 4.2. In this case, FWA is applied to both the blade wake and the duct wake.

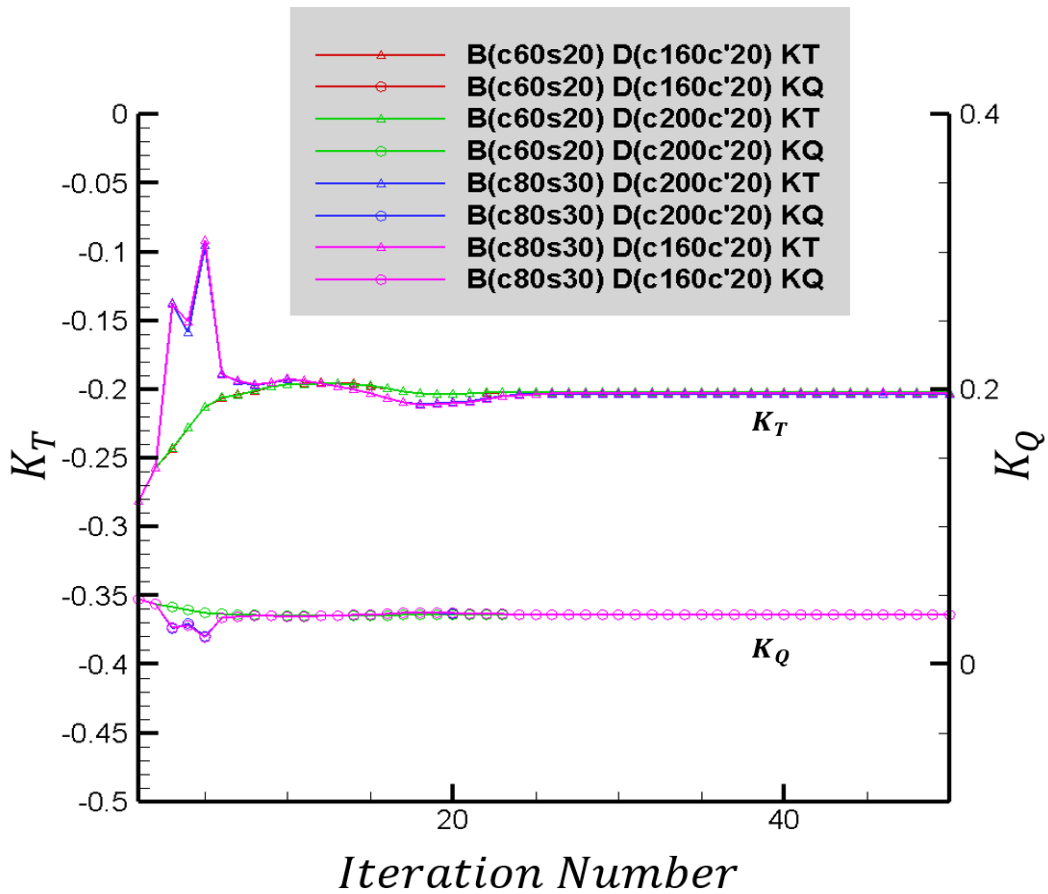
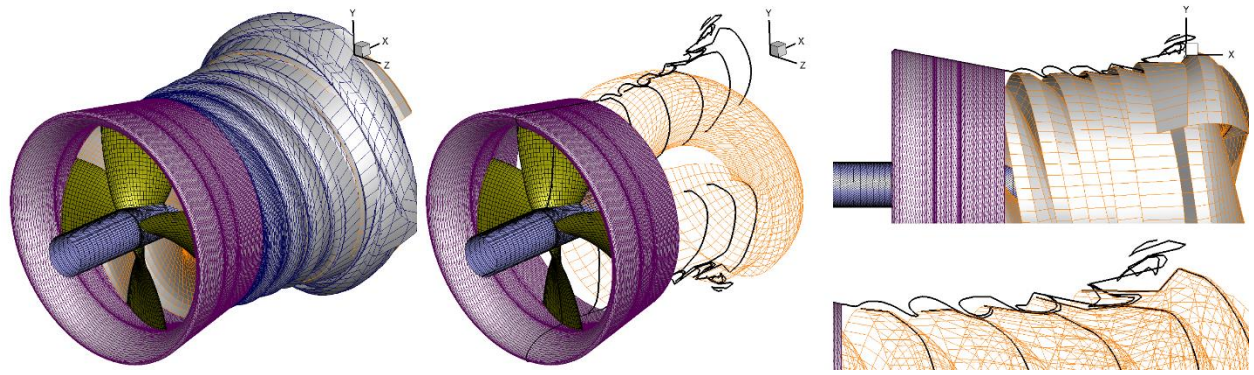
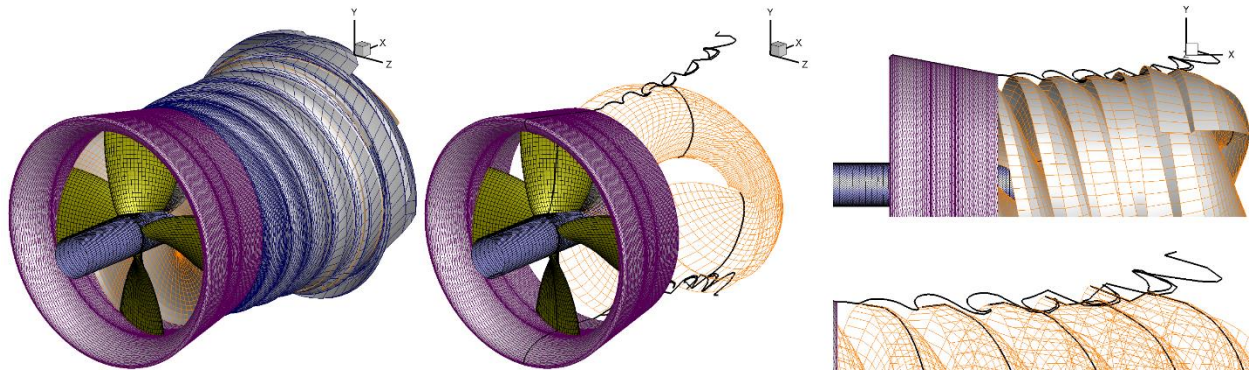


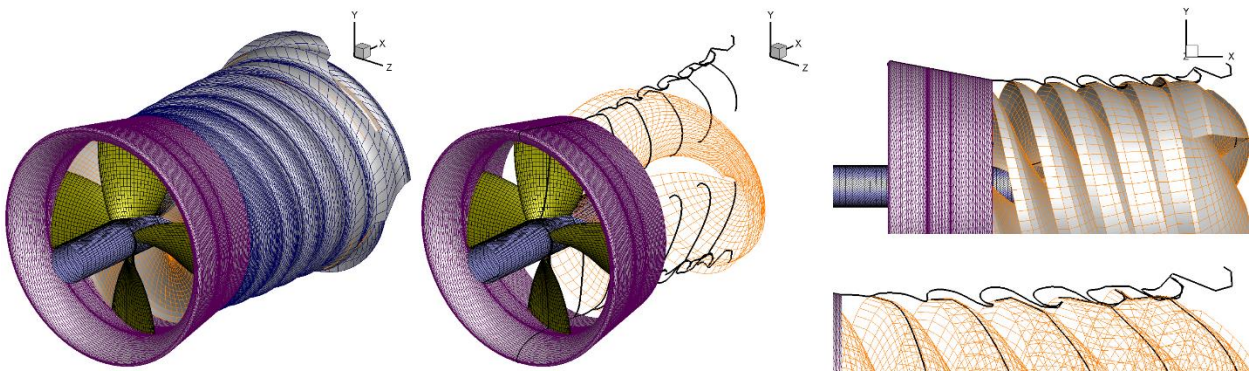
Figure 4.1 Convergence study of the predicted blade thrust and torque coefficients with a number of panels on the blade and duct. B(c60s20) and D(c160c'20), for example, represent 60×20 (chordwise×spanwise) panels on blade and 160×20 (chordwise×circumferentially) panels on the duct.



(a)



(b)



(c)

Figure 4.2 (Continued next page).

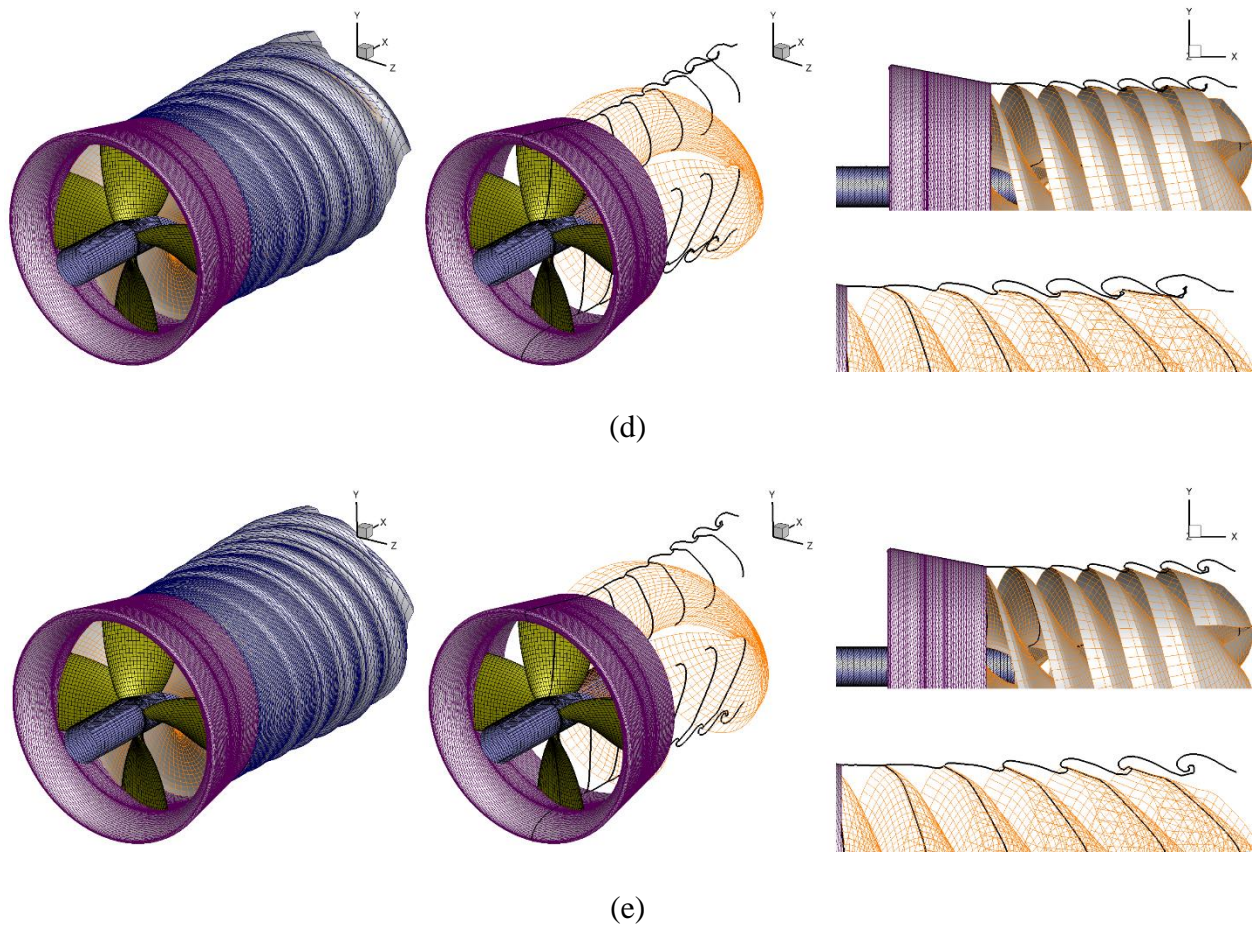


Figure 4.2 Blade and duct wake geometries from FWA at (a) $J_s = 0.3$, (b) $J_s = 0.4$, (c) $J_s = 0.5$, (d) $J_s = 0.6$, and (e) $J_s = 0.7$. 100 panels are used to discretize both the blade wake and the duct wake. KA4-70 ducted propeller is tested.

Figure 4.4 through 4.7 present the convergence history of the wake panels during the wake alignment scheme applied on both the duct/blade wake using 100 panels at design advance ratio, $J_s = 0.5$. Concentrated shedding vortex is plotted on the planes which cut through the center of propeller geometry to show the detailed distribution of the wake panels. FWA starts its first iteration based on the helical and cylindrical shapes for the blade wake and duct wake respectively. Then, the solutions based on these initial geometries are used for the next iteration until the predicted thrust and torque converge. Figure 4.4 also shows the contour plots of the magnitude of

cross product between the direction of vortex segment and that of the total velocity induced on the segment. The velocity vectors are also shown on the wake panels to visualize the relative directions of the two vector quantities, i.e. velocity vector and wake panel (vortex segment). The value of zero for the cross product magnitude means the wake panels are fully aligned to the local velocity based on the following equation:

$$\text{Cross Product} = \mathbf{V}_{total,i} \times \mathbf{s}_i. \quad (4.1)$$

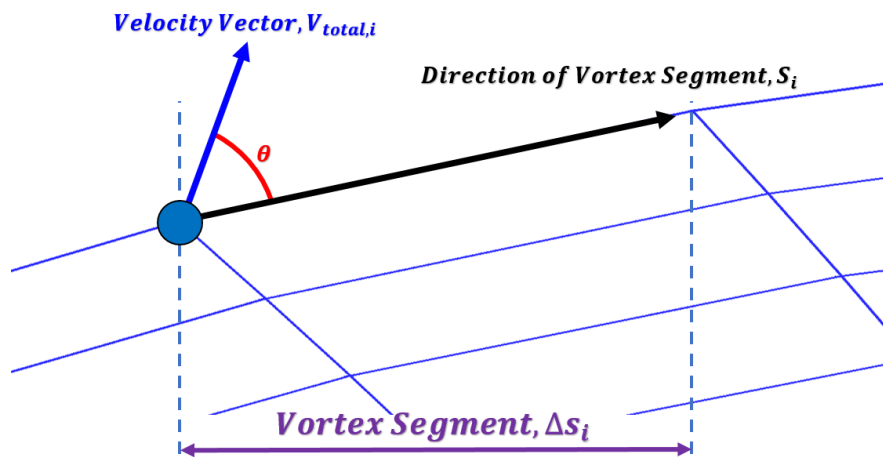


Figure 4.3 Unit direction vector of vortex segment and the velocity vector that is used to align the vortex segment. The angle between the two vector quantities are denoted as θ .

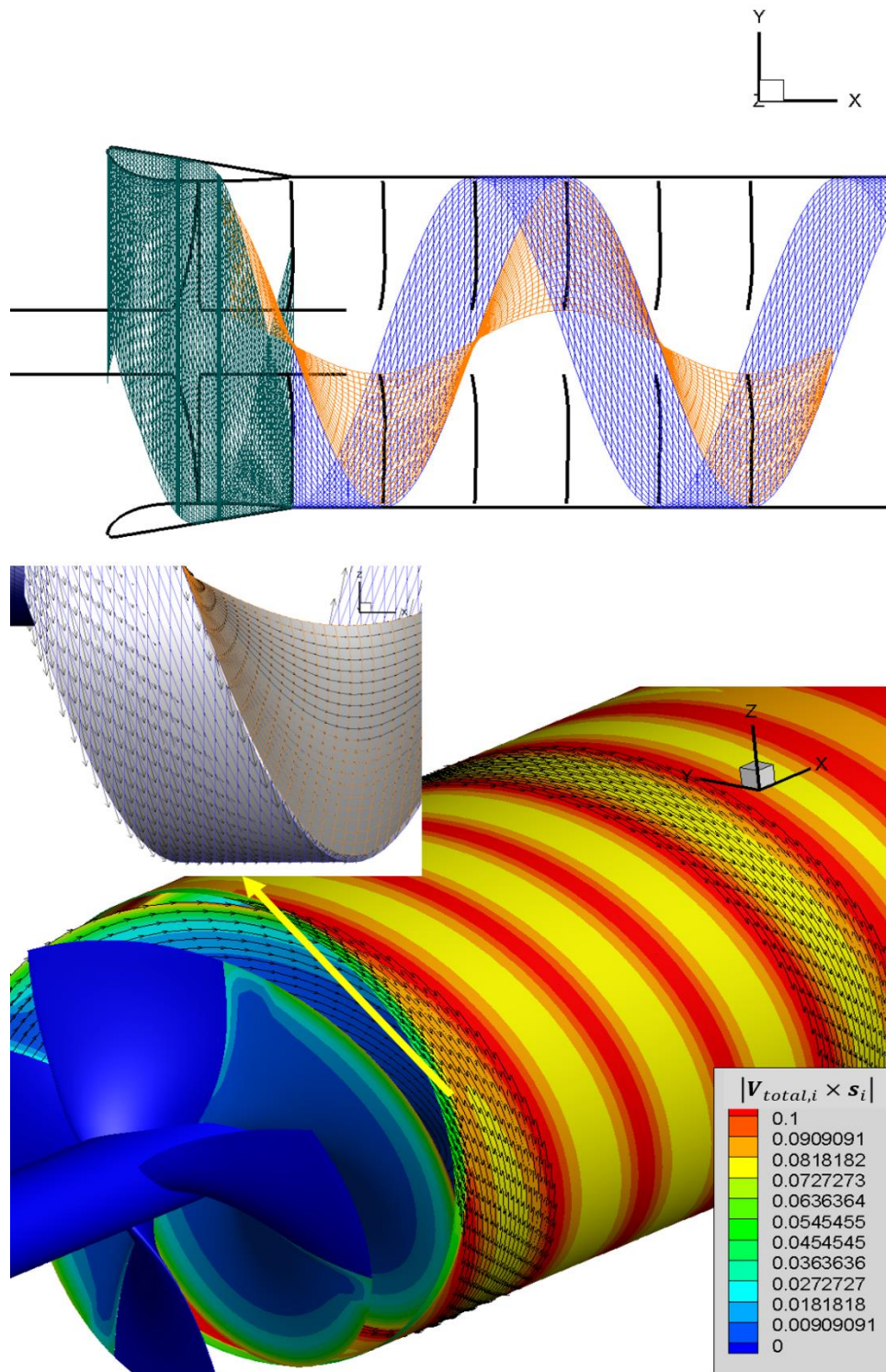


Figure 4.4 Convergence of the blade/duct wake using 100 wake panels (streamwise direction) at the first iteration: KA4-70 ducted propeller, $J_s=0.5$, and $\Delta t = 6^\circ$. Velocity vectors are plotted on the wake panels (upper) with the contour plots of the cross product magnitude, $|V_{total,i} \times s_i|$ (lower). Only parts of wakes are plotted for clarity.

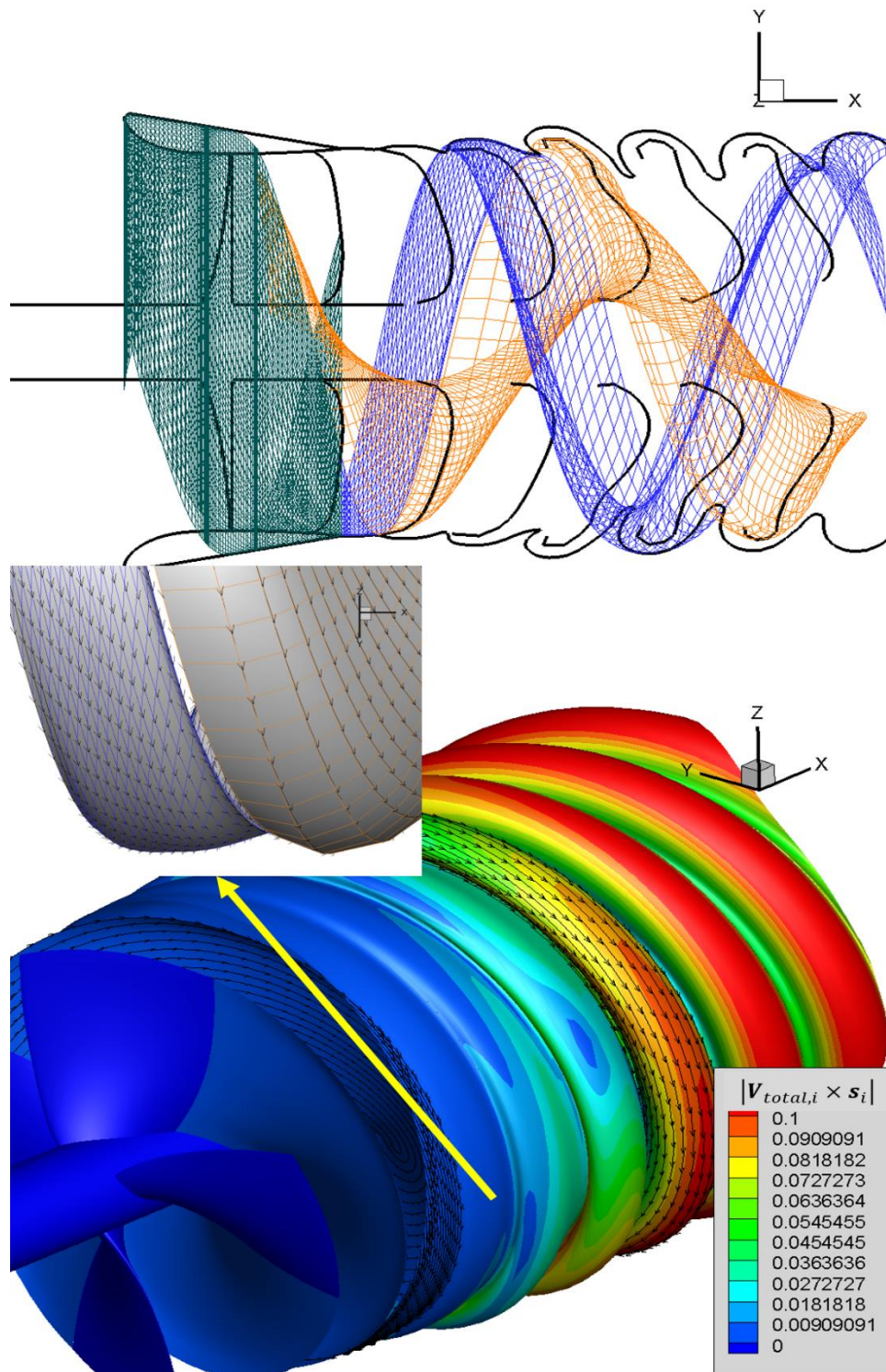


Figure 4.5 Convergence of the blade/duct wake using 100 wake panels (streamwise direction) at the 10th iteration: KA4-70 ducted propeller, $J_s=0.5$, and $\Delta t = 6^\circ$. Velocity vectors are plotted on the wake panels (upper) with the contour plots of the cross product magnitude, $|V_{total,i} \times S_i|$ (lower). Only parts of wakes are plotted for clarity.

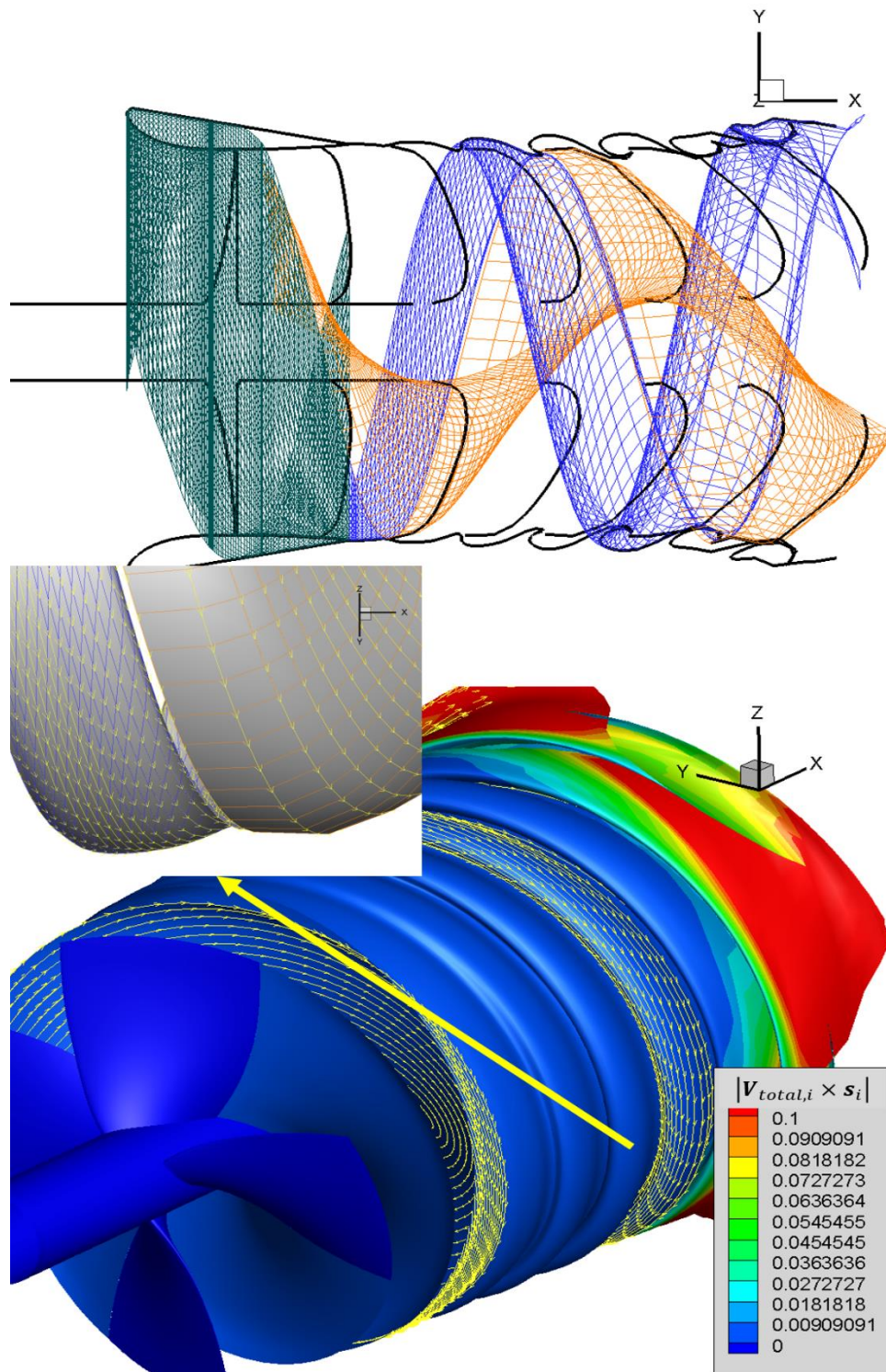


Figure 4.6 Convergence of the blade/duct wake using 100 wake panels (streamwise direction) at the 20th iteration: KA4-70 ducted propeller, $J_s=0.5$, and $\Delta t = 6^\circ$. Velocity vectors are plotted on the wake panels (upper) with the contour plots of the cross product magnitude, $|V_{total,i} \times s_i|$ (lower). Only parts of wakes are plotted for clarity.

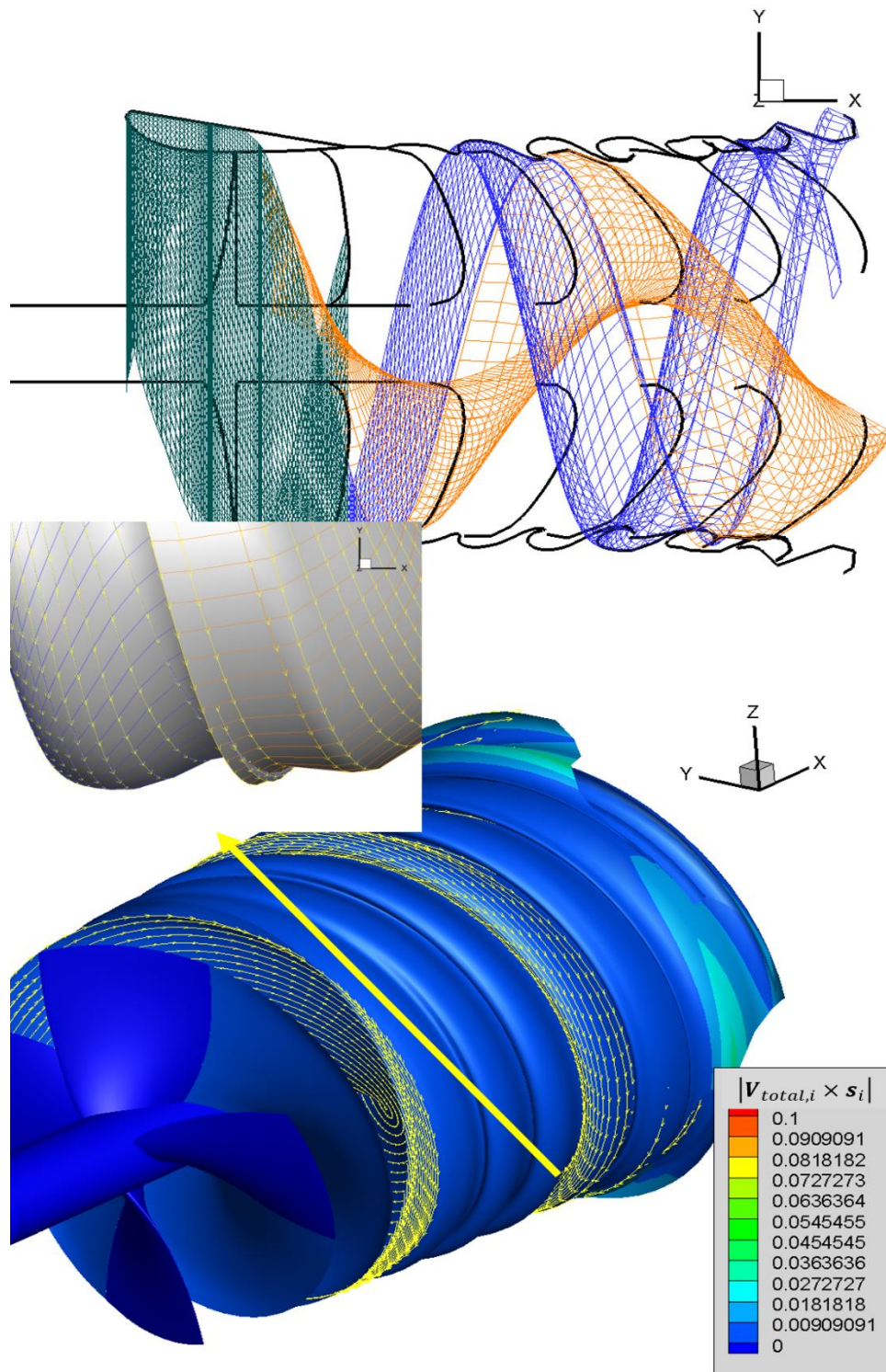


Figure 4.7 Convergence of the blade/duct wake using 100 wake panels (streamwise direction) at the 30th iteration: KA4-70 ducted propeller, $J_s=0.5$, and $\Delta t = 6^\circ$. Velocity vectors are plotted on the wake panels (upper) with the contour plots of the cross product magnitude, $|\mathbf{V}_{total,i} \times \mathbf{s}_i|$ (lower). Only parts of wakes are plotted for clarity.

As it can be seen, the first iteration of FWA starts with the velocity vector and the vortex segments, which are diverging into totally different directions. However, with iterations, the vortex segment starts to be aligned to the velocity vector making the magnitude of the cross products fall close to zero. It is interesting to observe that the convergence starts from the region close to the blade and advances toward downstream.

4.1.2 Full Blown RANS Simulation

Full Blown RANS simulations are conducted using ANSYS/Fluent with periodic interface, which requires only a quarter of the whole fluid domain to simulate the four-bladed ducted propeller. For a better resolution of the boundary layer structures along the propeller surface, structured meshing model is adopted. To reduce the possible artificial diffusivity, structured meshing model is used for both the blade wake and duct wake.

Detailed description of the calculation parameters is presented in [H. Fan 2015], so the summary is presented in this section. As listed in Table 4.1, $\kappa - \omega$ SST turbulent model is adopted. QUICK scheme and SIMPLEC scheme are used for the spatial discretization and the pressure correction respectively. Over 6 million polyhedral cells are used to calculate the domain with periodic boundary condition. It took over 32 hours on 32 Intel Xeon 2.54 GHz CPUs to make the residuals fall below 1.0E-6.

Table 4.1 Parameter settings in RANS simulations and the computational time, adjusted from Table 4.1 of [H. Fan 2015]

Cell Number	Over 6 million
Reynolds Number	1.0E+6
Turbulent Model	<i>k-ω SST</i>
Pressure Correction Scheme	<i>SIMPLEC</i>
Spatial Discretization	<i>QUICK</i>
CPU Type	Intel Xeon 2.54 GHz CPU
Total Time for Calculation (32 CPUs)	Over 32 Hours

Figure 4.8 shows the mesh gridding of KA4-70 ducted propeller. Only a quarter of the whole geometry is presented since the periodic boundary condition is applied. Also, a plane in the $x - y$ direction is used to show the two-dimensional contour plots of shedding vortex magnitude. These plots are compared to the aligned wake sheets, which are also plotted on a plane in the $x - y$ direction, from the panel method as shown in Figure 4.9.

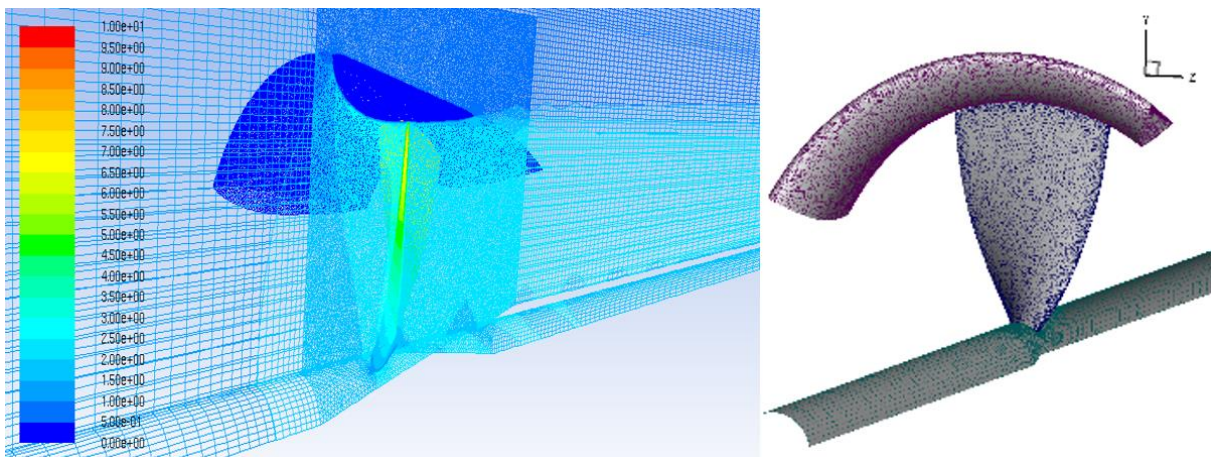


Figure 4.8 Gridding of blade, hub, and duct in RANS simulation (right) and the two-dimensional plane cutting through the propeller geometry with an angle of zero degree (left).

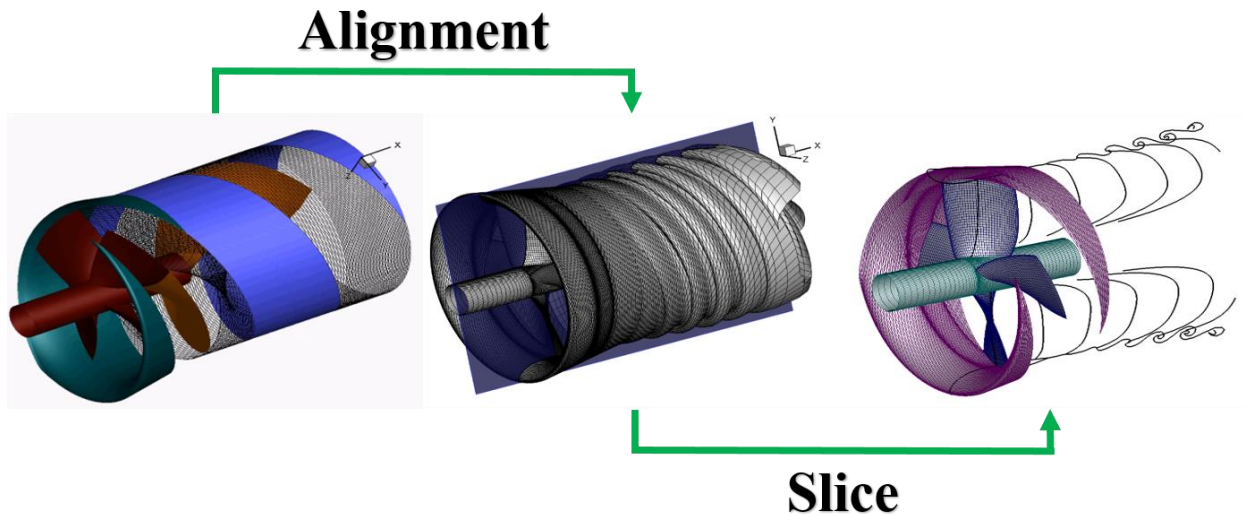
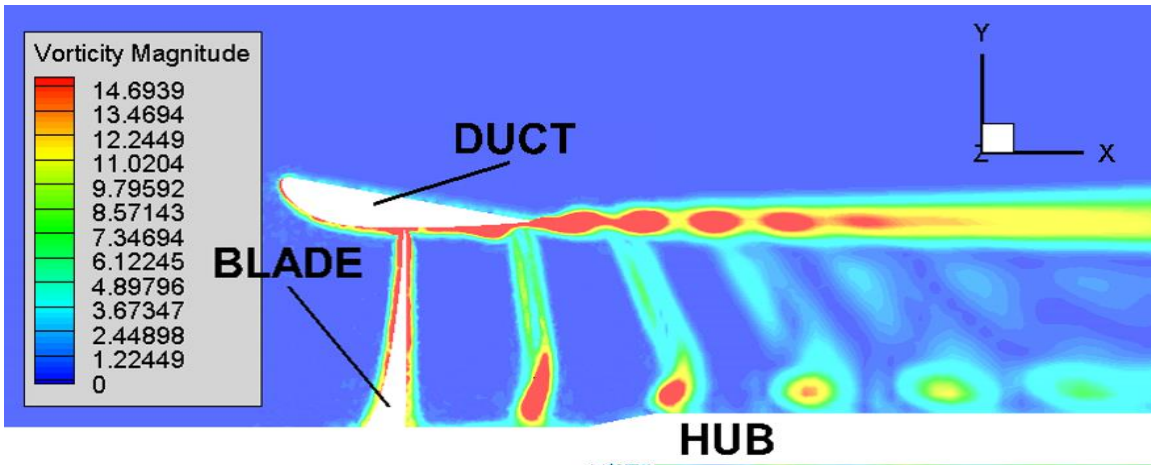


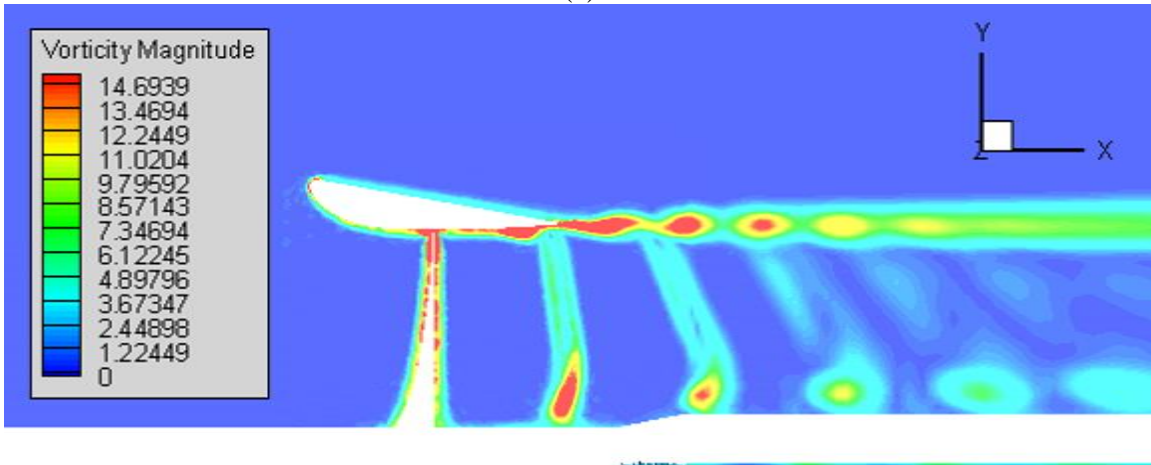
Figure 4.9 Schematic view of plotting wake sheet from the panel method on two-dimensional plane, which slices the center of propeller geometry in the $x - y$ direction.

4.1.3 Correlations

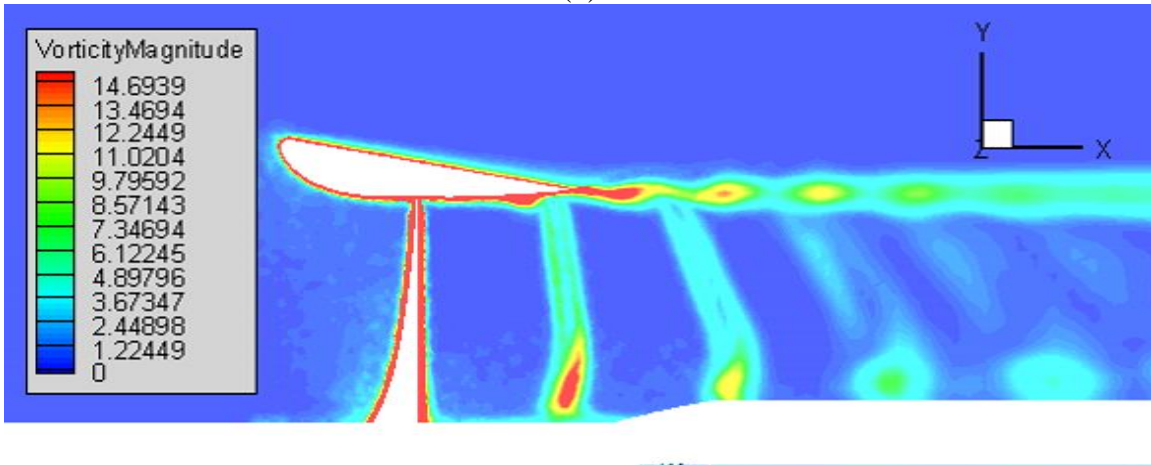
Two-dimensional contour plots from RANS simulations are presented in Figure 4.10 for a range of advance ratios from 0.3 to 0.5. As it can be seen, the higher the advance ratio is, the more shedding vortex behind blade and duct trailing edge diffuses. Also, the case with the lower advance ratio shows stronger shedding vortex near the trailing edge of duct than the case with the higher advance ratio. The shedding vortex gradually diffuses as it flows into downstream with local flow.



(a)



(b)



(c)

Figure 4.10 Two-dimensional contour plots of KA4-70 ducted propeller and shedding vortex with diffusion for advance ratios of (a) 0.3, (b) 0.4, and (c) 0.5.

Now, Figure 4.11 and 4.12 show the correlations of the wake distribution between the results from panel method and RANS simulations. The range of the investigated advance ratio is 0.4 to 0.5. The locations of the concentrated vortex from panel method are in good agreement with those of the shedding vortex predicted by RANS simulations. These agreement are more addressed especially near the duct trailing edge. Also, the curling behavior of duct wake due to its close distance to the tip of blade wake is well predicted by both methods with good agreement. This curling comes from the strong tip vortex, which is shed from the blade tip and therefore located at the tip of the blade wake. As shown in the same figures, the strength of the curling gets weaker as the shedding vortex flows into downstream due to diffusion. The same happens to the shedding vortex from the blade as it flows along with the local flow.

The curling behavior of the wake panels is well represented near duct trailing edge where the shedding vortex starts to leave. However, in the region where the shedding vortex gets spread far downstream, distribution of the wake panels by panel method with FWA cannot well represent the diffusion effects. Due to this drawback, the predicted thrust and torque on the blade are over predicted compared to the experiments especially at the lower advance ratios, as shown in Figure 4.13.

On the other hand, cylindrical shape of duct wake produces better correlations with the experiments. It is because of a constant distribution of duct wake, which is somewhat artificial and requires radius control on the aligned blade wake to avoid penetration. As shown in Figure 4.13, cylindrical duct wake with the two repaneling options shows very good agreement with the experiments over the most advance ratios down to $J_s=0.30$, while Option 2 under predicts the blade torque, even though not considerably.

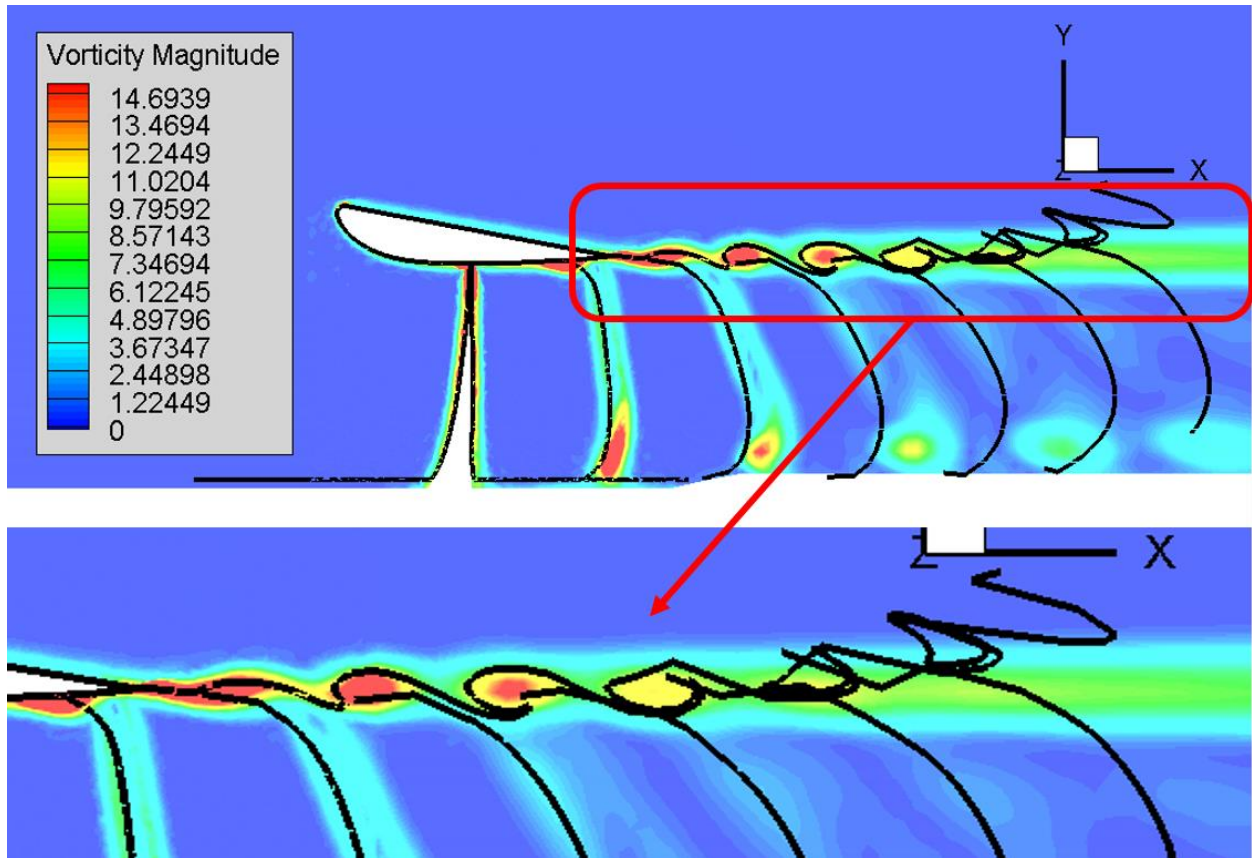


Figure 4.11 Correlations of two-dimensional contour plots of the shedding between the results from RANS simulations and panel method (black solid line) for the advance ratios of 0.4.

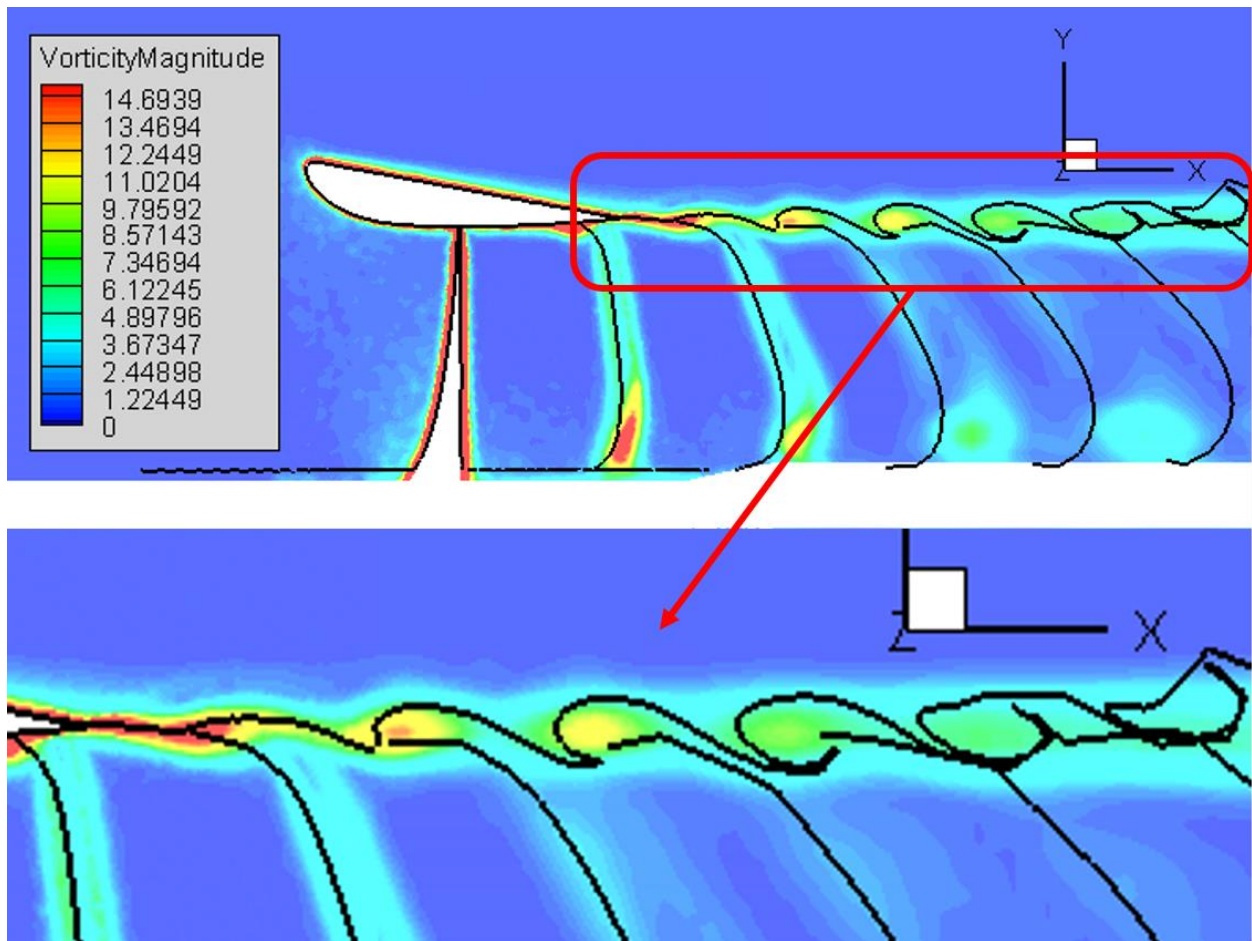


Figure 4.12 Correlations of two-dimensional contour plots of the shedding between the results from RANS simulations and panel method (black solid line) for the advance ratios of 0.5.

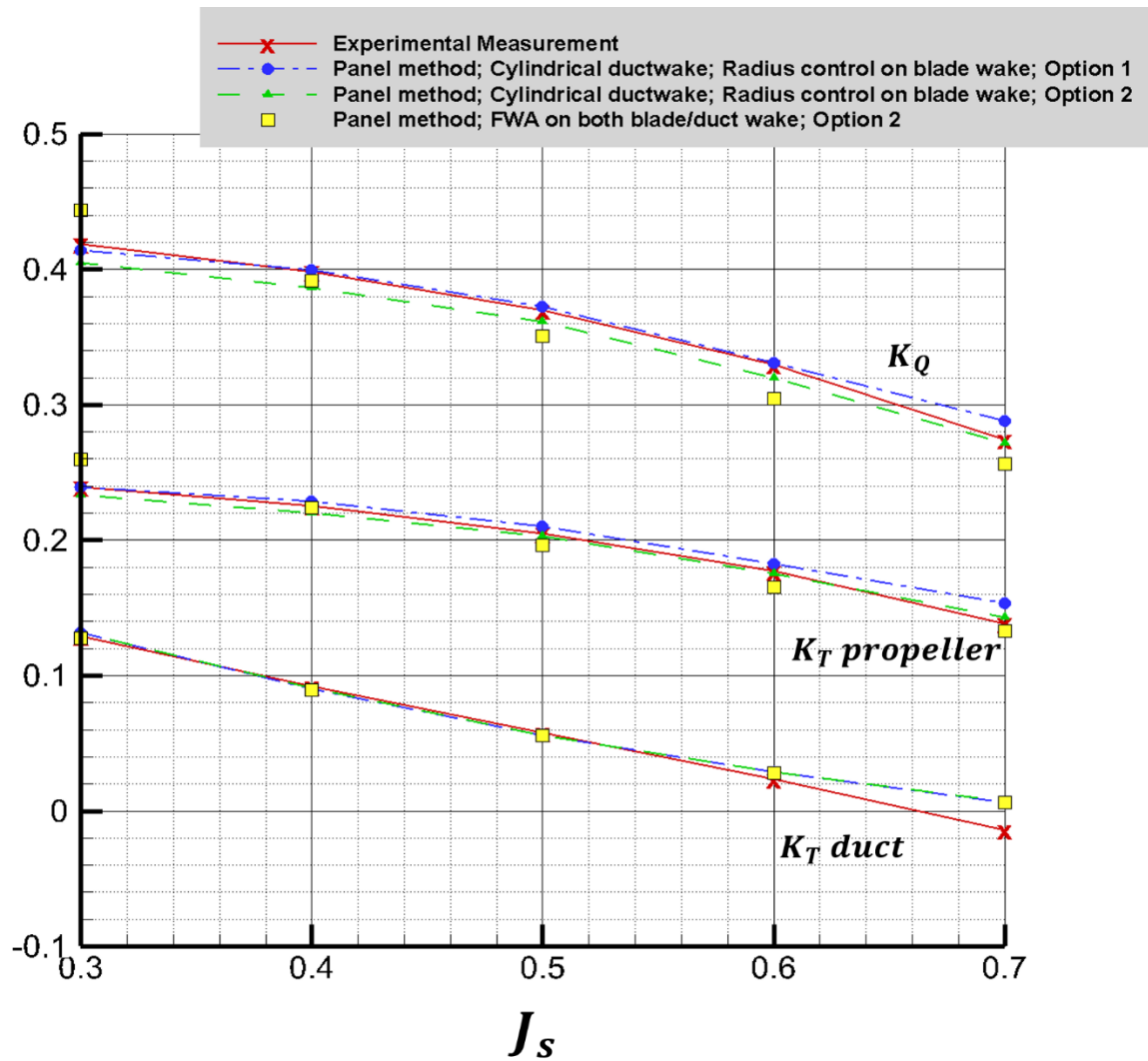


Figure 4.13 Predicted force performance of KA4-70 ducted propeller from the experiments and panel method. FWA is applied to both the duct/blade wake, but a cylindrical duct wake is assumed when the repaneling options are adopted.

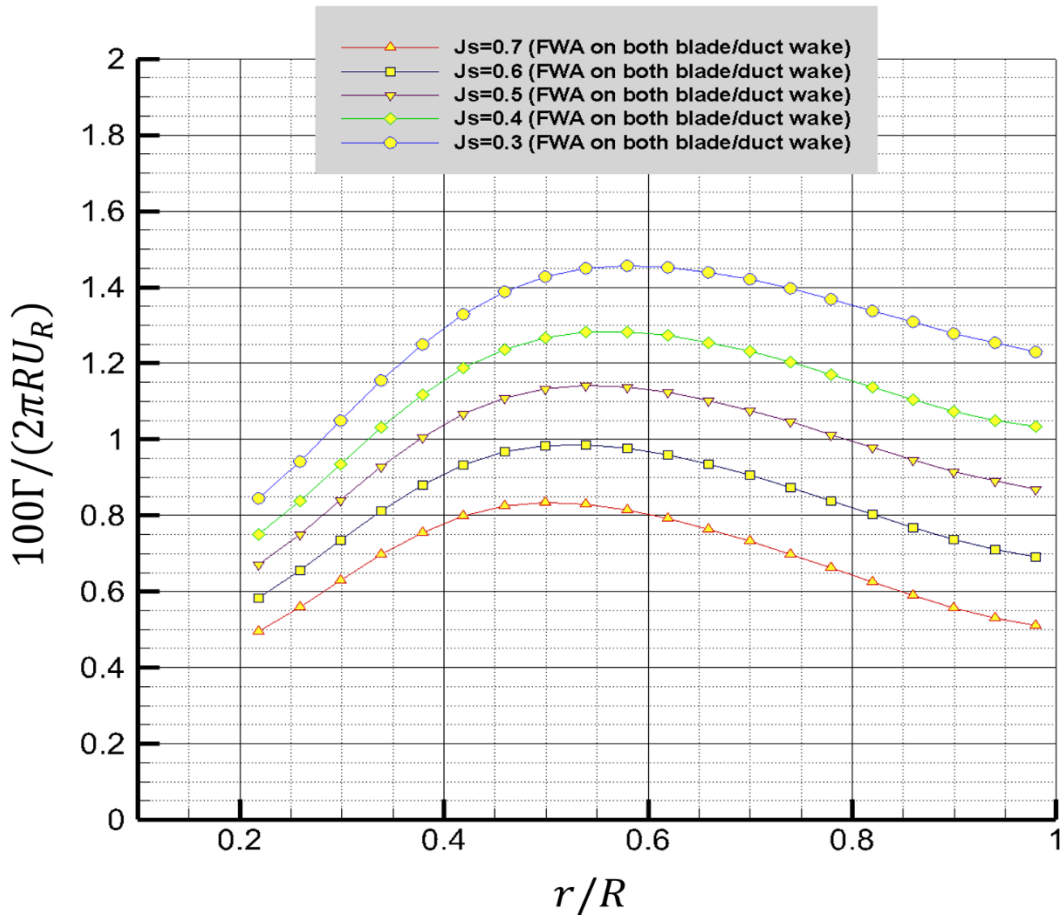


Figure 4.14 Circulation distributions of KA4-70 ducted propeller from panel method with FWA on both blade wake and duct wake for the advance ratios from 0.3 to 0.7. Repaneling Option 2 is adopted here.

Given that the current FWA scheme is based on the iterative manner as introduced previously, convergence history which shows not only the accurate but also the stable results is essential. Figure 4.16 and 4.17 show the convergence history of the predicted thrust and torque coefficients using the two repaneling options, and duct wake here is assumed to be cylinder. As it can be seen, both options show stable convergence histories not only at the high advance ratios but also at the low advance ratios, even though only Option 2 keeps stable at very high loading condition, i.e.

$J_s=0.2$. This is due to the fact that the wake panels, which do not advance farther to downstream become very compact near blade and duct inner side. The unmatched panels (Figure 4.15 (a)) between the duct inner side and the outer edge of blade wake in Option 1, thus cause the unstably-induced velocities on the wake panels. On the other hand, the matched panels (Figure 4.15 (b)) in Option 2 produce relatively stable convergence histories even at the very high loading condition.

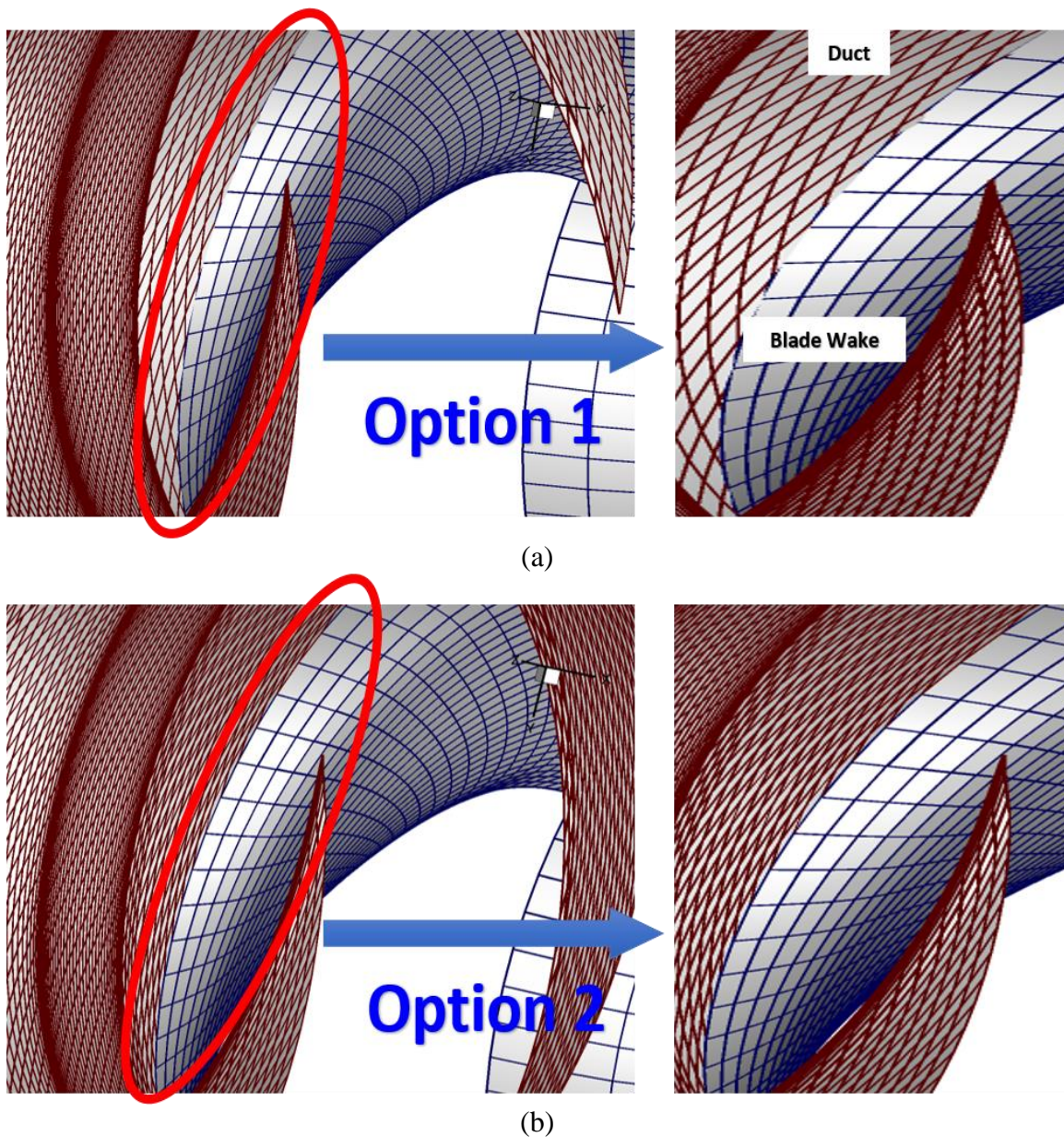


Figure 4.15 Matched (a) and Unmatched (b) panels between the duct inner side and the outer edge of blade wake from Option 1 and 2, respectively.

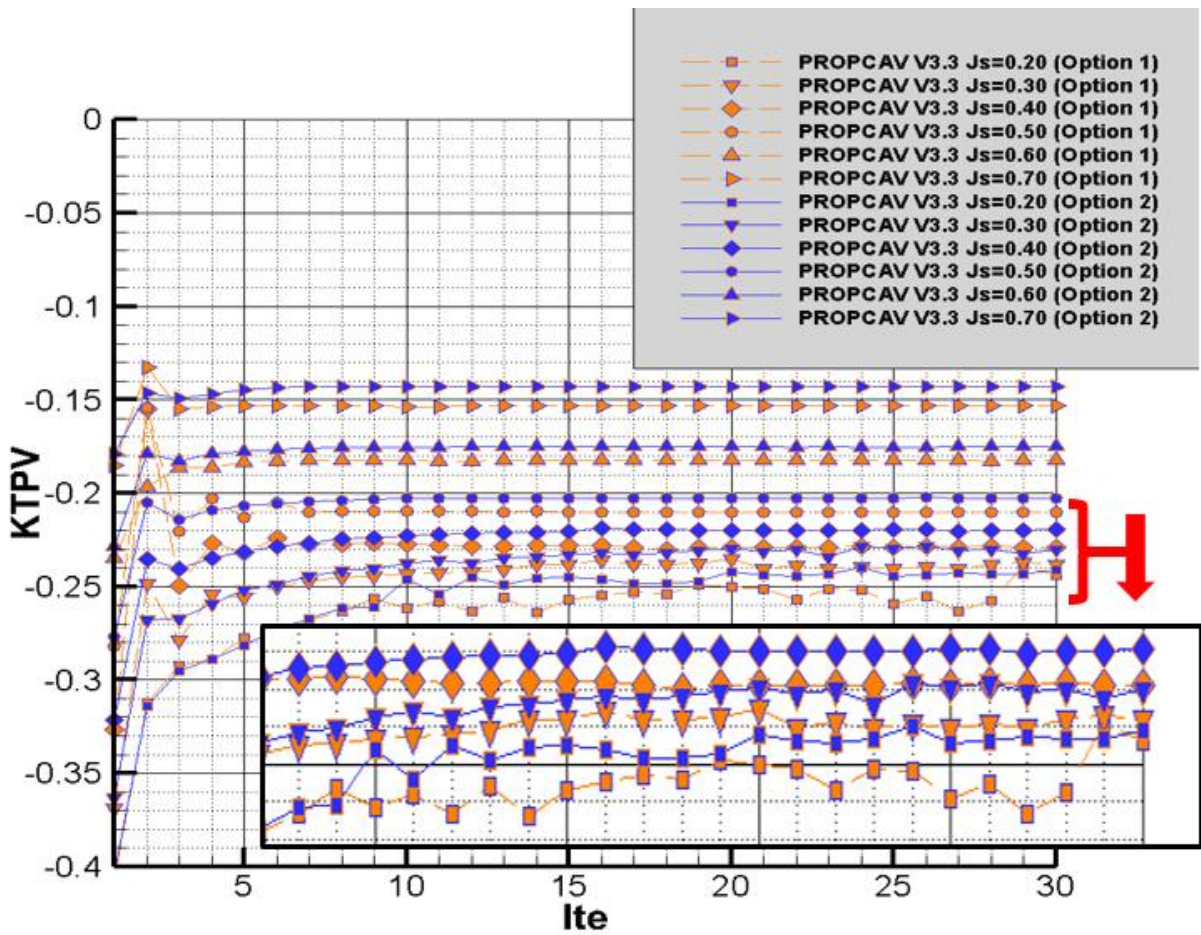


Figure 4.16 Convergence histories of the predicted thrust coefficients on the blade using FWA with the two repaneling options. The horizontal axis indicates the number of iterations in FWA.

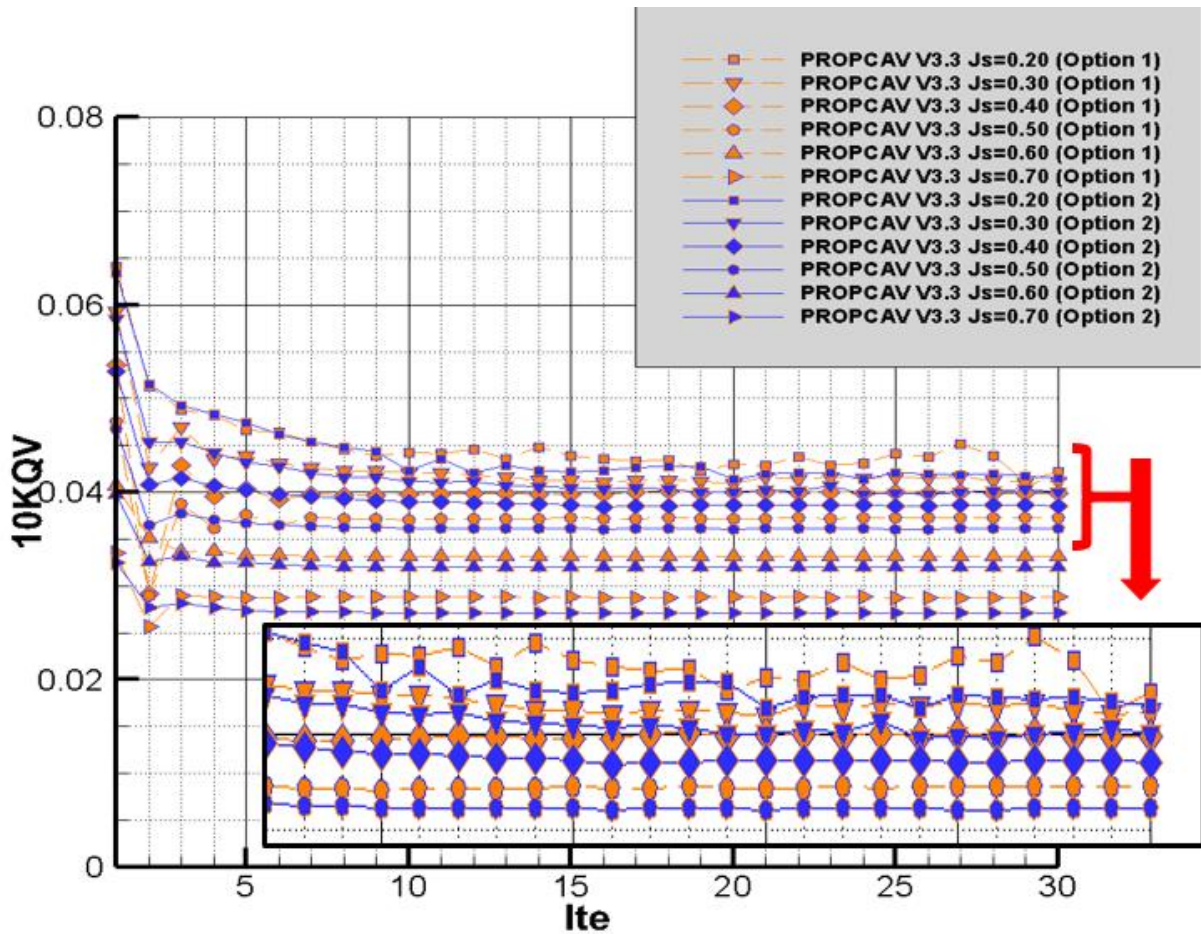


Figure 4.17 Convergence histories of the predicted torque coefficients on the blade using FWA with the two repaneling options. The horizontal axis indicates the number of iterations in FWA.

Figure 4.18 presents the pressure distribution along the several blade sections at design advance ratio, $J_s=0.5$. Correlations are made between the results from RANS and panel method. The predicted results show that panel method in general shows very good agreement with RANS simulations over the most blade sections. Only the result from RANS at the section near the blade tip ($r/R=0.958$) seems to wiggle due to the unstructured mesh around the thin blade tip. Panel method, however, shows the reasonable results which are consistent with the other results evaluated at inner sections.

Now, the pressure distribution over duct is investigated by correlating the results predicted by panel method, RANS, and RANS/VLM coupling method [Kinnas et al. 2013]. The RANS/VLM coupling method, developed by Ocean Engineering Group at UT-Asutin, couples a potential flow based vortex-lattice method with an axisymmetric-swirl RANS solver for the analysis of propulsion system. More details of the coupling method are left aside in this thesis and can be found in [Kinnas et al. 2013]. As shown in Figure 4.21, the prediction of the circumferentially averaged pressure distribution by panel method is in good agreement with the result from RANS/VLM coupling method. The result from RANS slightly deviates from the other two methods, even though not significantly.

It is worthwhile to compare the results from panel method with Option 1 and Option 2. Both are in good agreement along the suction side and around front and mid part (Figure 4.19 depicts the subdivision on the duct) on the pressure side of the duct. However, they show apparent deviation at the after part on the pressure side. In this region, the predicted duct pressure by Option 1 shows the unnatural protrusion, while Option 2 shows the consistent pressure distribution as the other parts on the pressure side. It is because the duct panels which are very close to the outer edge of the blade wake are effectively avoided in Option 2 when evaluating the duct pressure due to the panel alignment between the wake and the duct, as shown in Figure 4.20. However, if those panels are not aligned as in the case of Option 1, the singular behaviors coming from the close distance between the wake and the duct are inevitably included in the evaluation of the duct pressure. These unnatural pressure peaks in Option 1 are more addressed in Figure 4.22 which shows the pressure distribution along the chordwise strips on the duct. This result clearly shows that the repaneling Option 2 should be used when the accurate evaluation of the duct pressure is required.

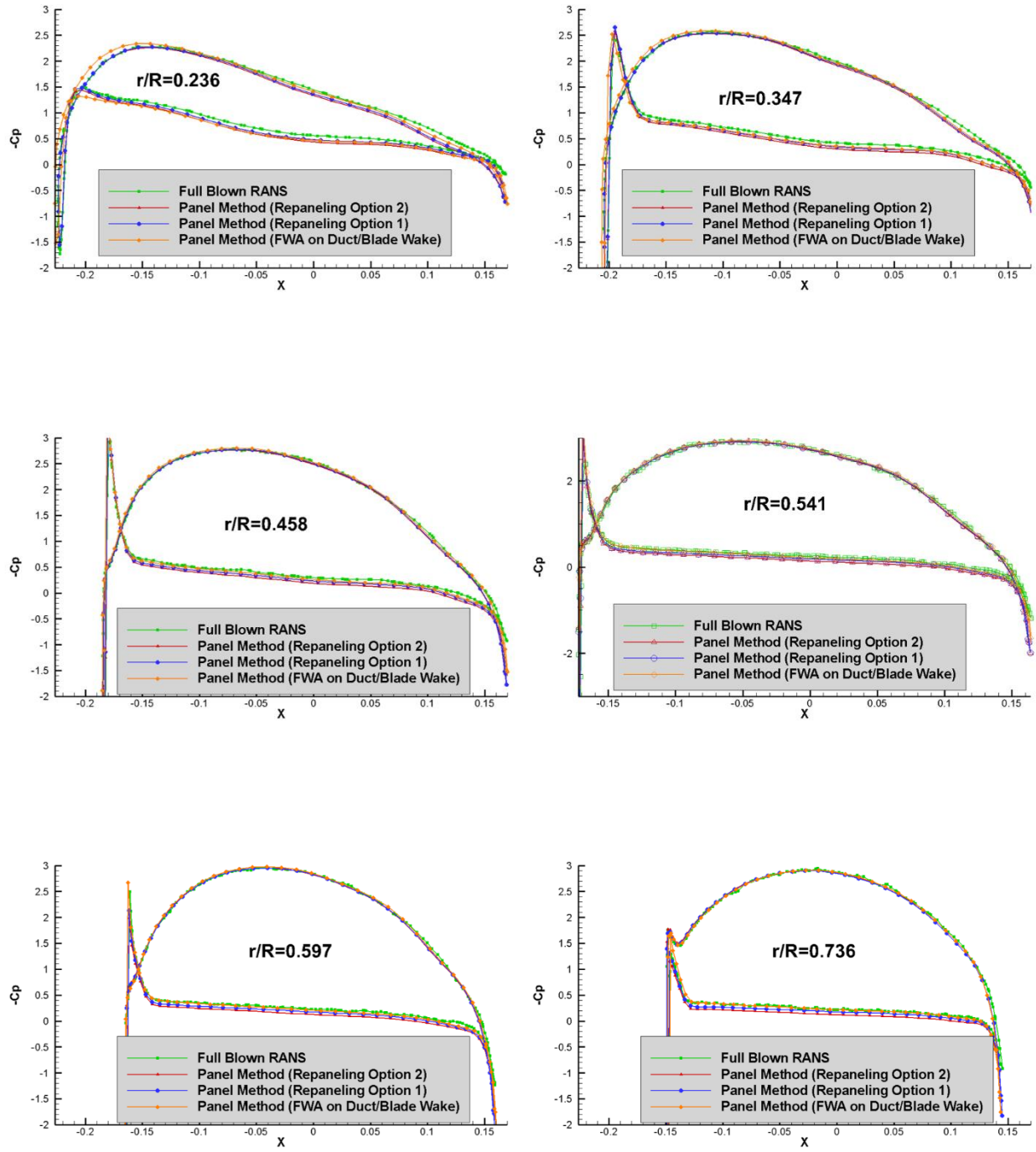


Figure 4.18 (Continued next page).

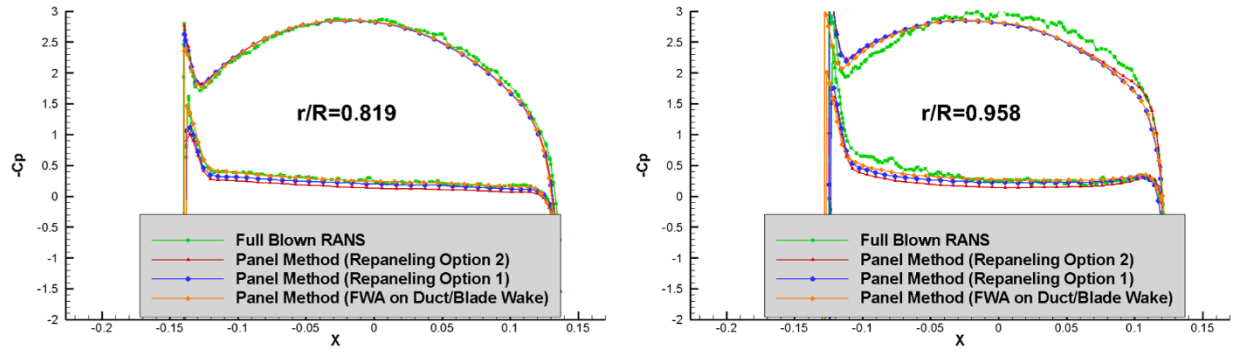


Figure 4.18 Correlation of the pressure distributions between the results from RANS and panel method at several blade sections. The radial location of each section is indicated in the figure.

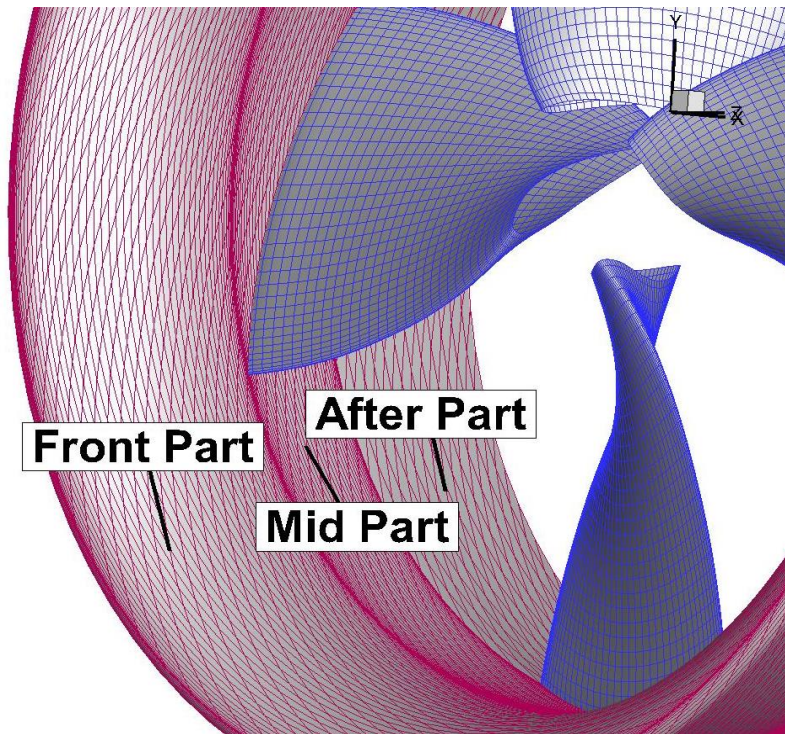


Figure 4.19 Description of subdivided parts on duct. Hub geometry is not included in this figure.

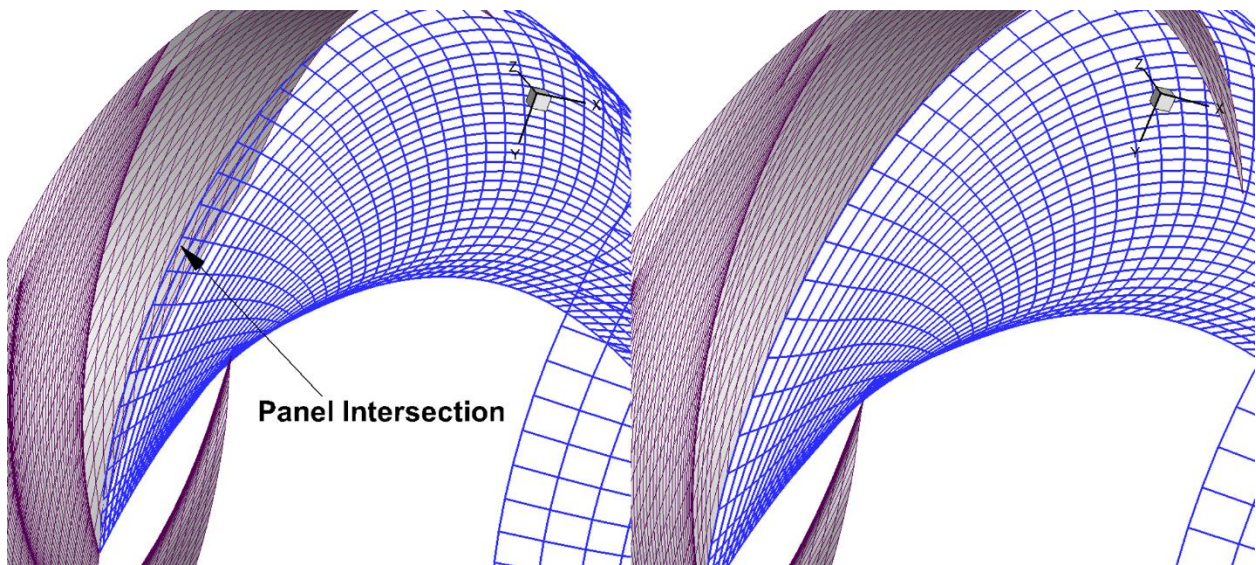


Figure 4.20 Relative distribution of the blade wake and duct panels. Very close distance between those panels might cause the singular behavior in Option 1 (left) unless they are aligned as in Option 2 (right).

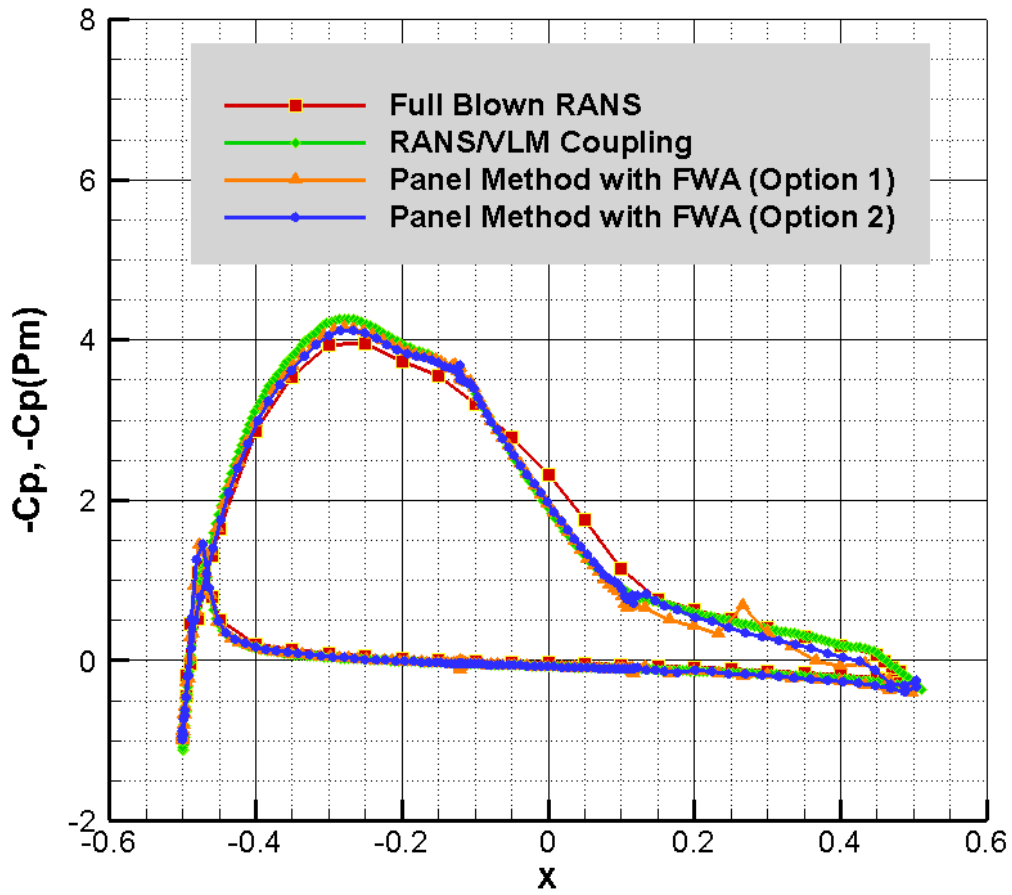


Figure 4.21 Correlation of the predicted circumferentially averaged pressure distribution on the duct between panel method (Option 1 and 2), RANS/VLM coupling method, and RANS simulation at $J_s=0.50$.

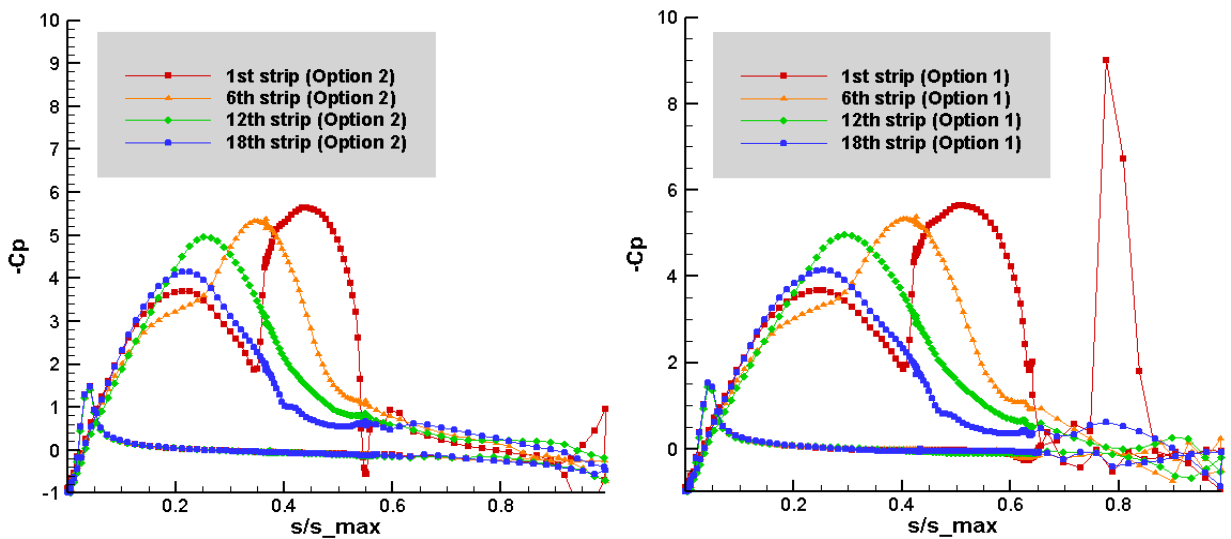
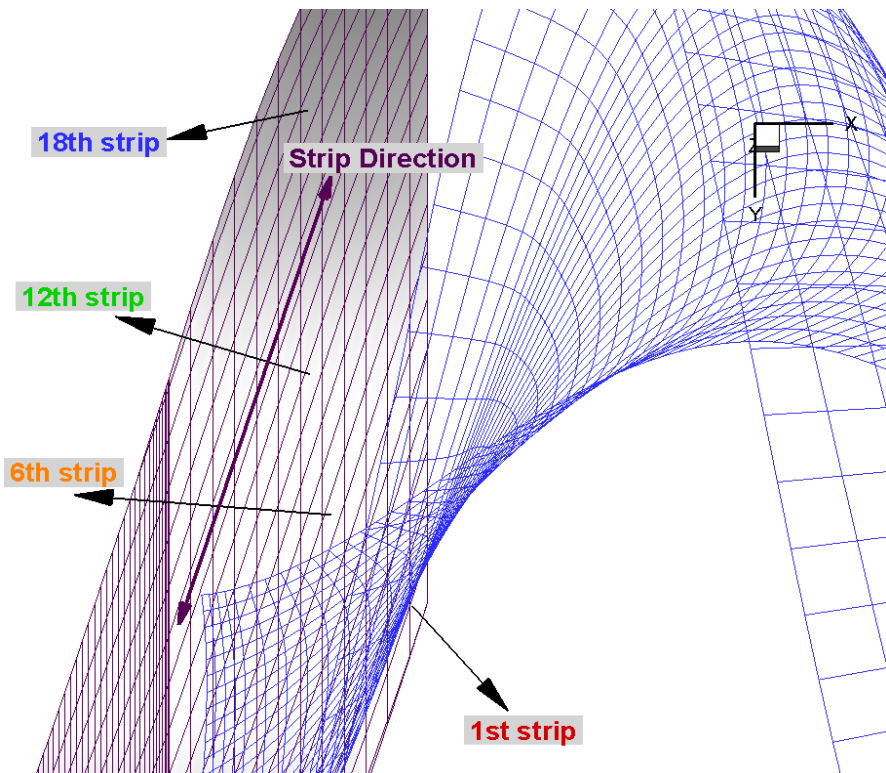


Figure 4.22 Description of the strips which are adopted for the pressure plotting on the duct (upper) and the corresponding pressure distributions on each strip from Option 2 (lower left) and Option 1 (lower right).

Chapter 5

Application to Open Propeller

This chapter will investigate the predicted performance of open propeller in uniform, non-uniform, and inclined flow. For the first two steady cases, FWA is applied to evaluate steady performance, while unsteady performance in inclined flow is evaluated using unsteady alignment model. DTMB 4661 propeller is adopted for a test model as shown in Figure 5.1. DTMB 4661 propeller is a five-bladed propeller with a high skew distribution, and the design advance ratio is $J_s = 1.14$.

[Boswell et al. 1984] conducted experiments using DTMB 4661 propeller in 10° and 20° inclined flow. Also, [Kinnas and Pyo 1997] evaluated the performance of DTMB 4661 propeller using VLM, based on the geometrical inclination. In other words, the trailing wake sheet was inclined by the inflow angle. The results from the experiment and VLM method are correlated with those from current method. On the other hand, panel method with unsteady alignment model was also applied to DTMB 4661 propeller by [H. Lee 2002], in which tip cavitation model is included, and the Euler-explicit scheme is used to align the wake sheet.

In section 5.1, first, DTMB propeller will be placed in uniform and non-uniform flow to predict its performance in steady state. Convergence study is made on the predicted forces with number of wake panels. Then, unsteady wake alignment model will be used in uniform flow case to correlate its results with what is from the steady alignment model. The aim of this test is at validating the results from unsteady alignment model and steady alignment model correspond to each other in the case of steady flow.

In section 5.2, unsteady performance of DTMB 4661 propeller is evaluated using panel method in 10° inclined shaft flow. The predicted unsteady performance of the thrusts and torques

coefficients on the blade are correlated with those from the two different methods, i.e. experiments and VLM. The numerical calculation is performed at the design advance ratio, $J_s = 1.14$.

5.1 Steady Wake Alignment

5.1.1 Uniform Inflow

Figure 5.1 through 5.5 show DTMB 4661 propeller with fully aligned wake sheet with different number of wake panels. Two-dimensional plots showing the shedding vortex after the trailing edge of blade are also presented. As shown in the figures, the shedding vortex from blade tip curls as it flows into downstream, while that from the root of the blade does not because of the wall effect from hub geometry. 80×30 (chordwise \times spanwise) panels are used to discretize blade, and infinite hub is assumed with the radius same as the inner most radius of the blade. No tip cavity model is assumed in this case. The convergence of loading on the blade with number of wake panels is shown in Figure 5.6. It shows the independency of panel method on the panel numbers of the wake, and based on this, only the case with 80 wake panels is used for the rest of investigation.

Convergence history of full wake alignment is shown in Figure 5.7 through 5.10 with the cross products magnitude plotted. As similar to the ducted propeller case, the magnitude of the cross products gets closer to zero from near blade to downstream. Note that the smaller the magnitude is, the further wake panel is aligned to the local velocity (yellow arrows, in Figure 5.7). The wake sheets are fully aligned up to one before the last strip with magnitude of cross products less than 0.01 after the 8th iteration. Discontinuity (colored in red) at the last strip is due to the truncation of wake sheet, although it does not affect the final results.

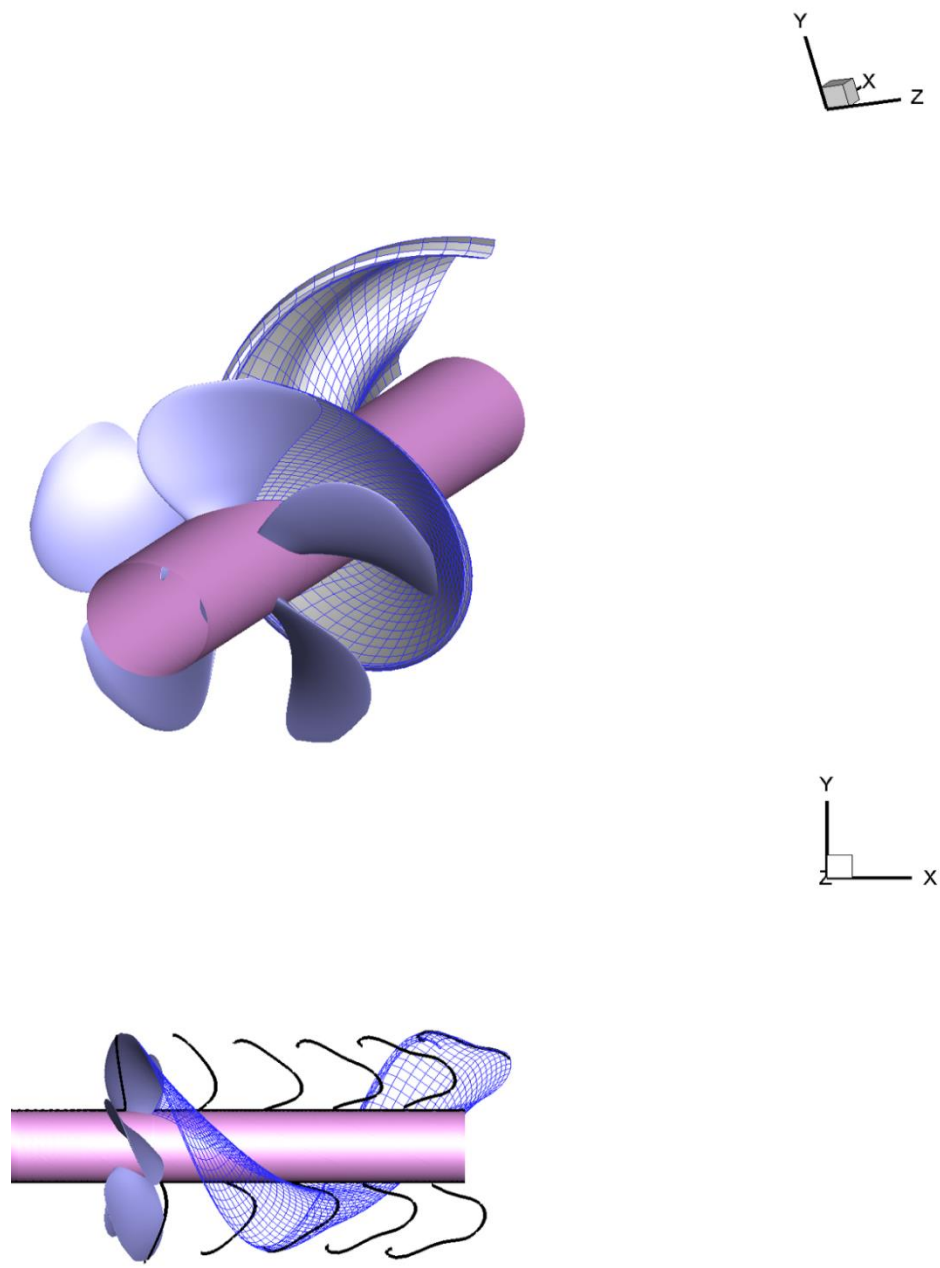


Figure 5.1 Wake geometries aligned using FWA with 60 wake panels in uniform flow: $J_S = 1.14$.

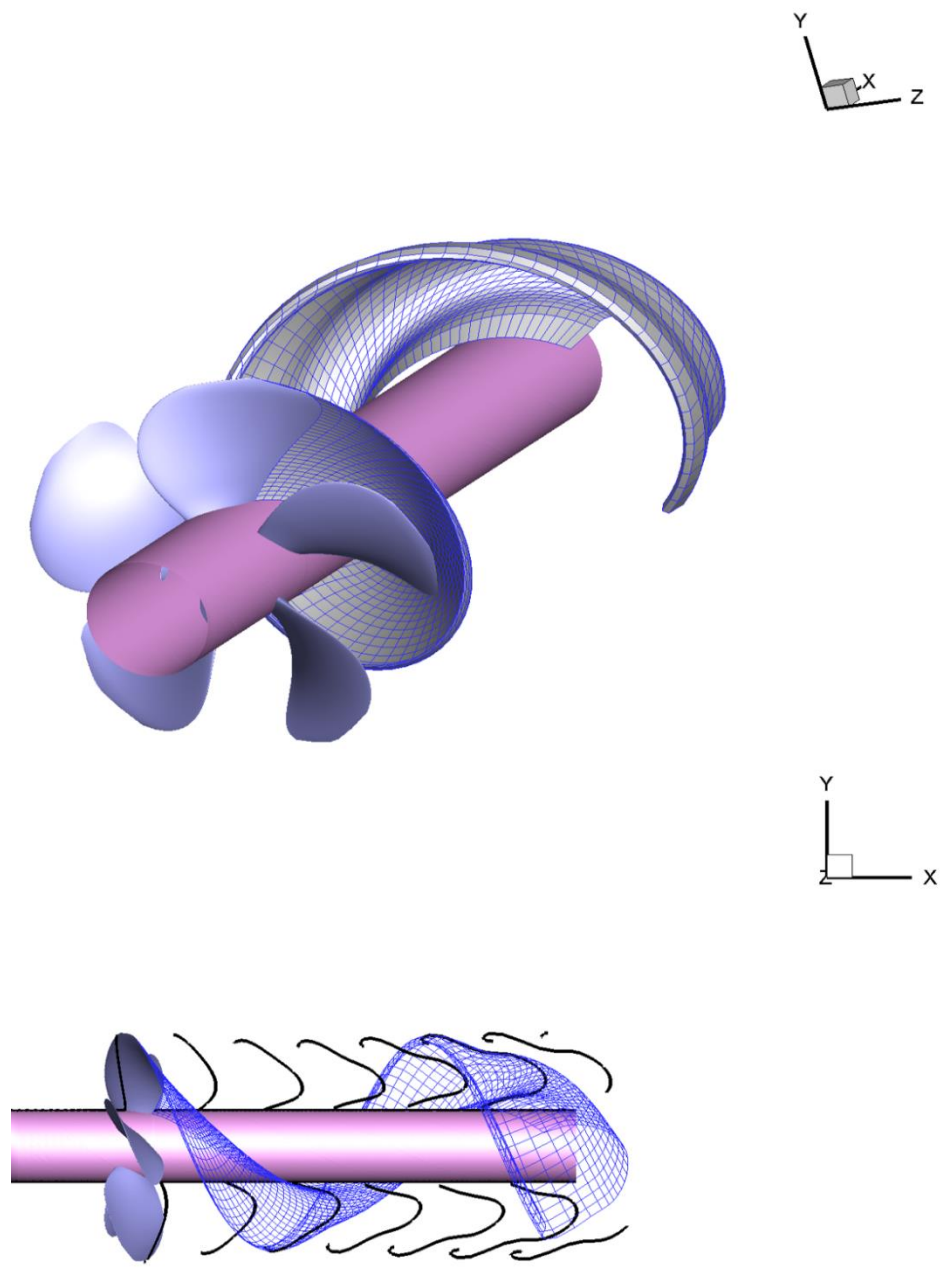


Figure 5.2 Wake geometries aligned using FWA with 80 wake panels in uniform flow: $J_s = 1.14$.

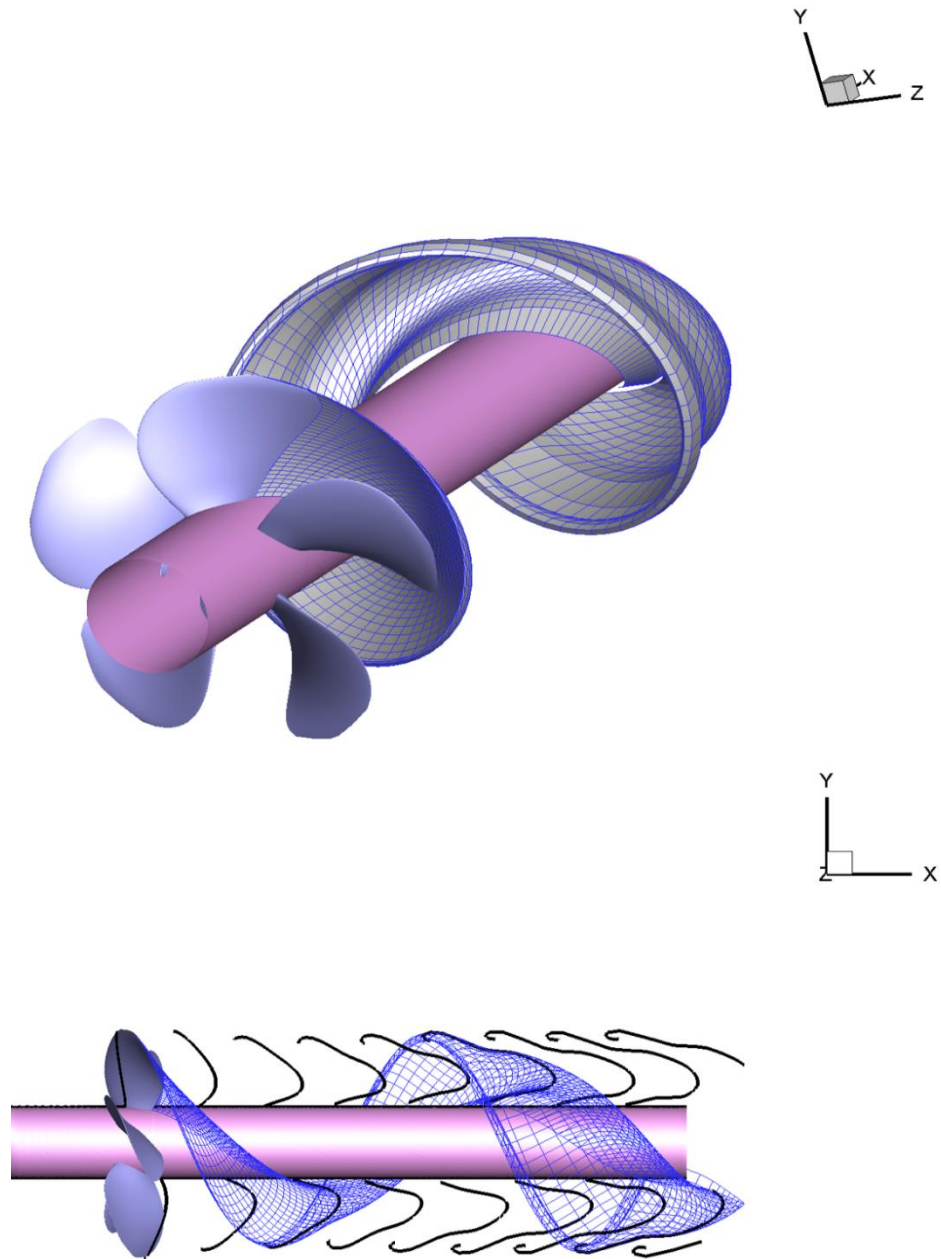


Figure 5.3 Wake geometries aligned using FWA with 100 wake panels in uniform flow: $J_s = 1.14$.

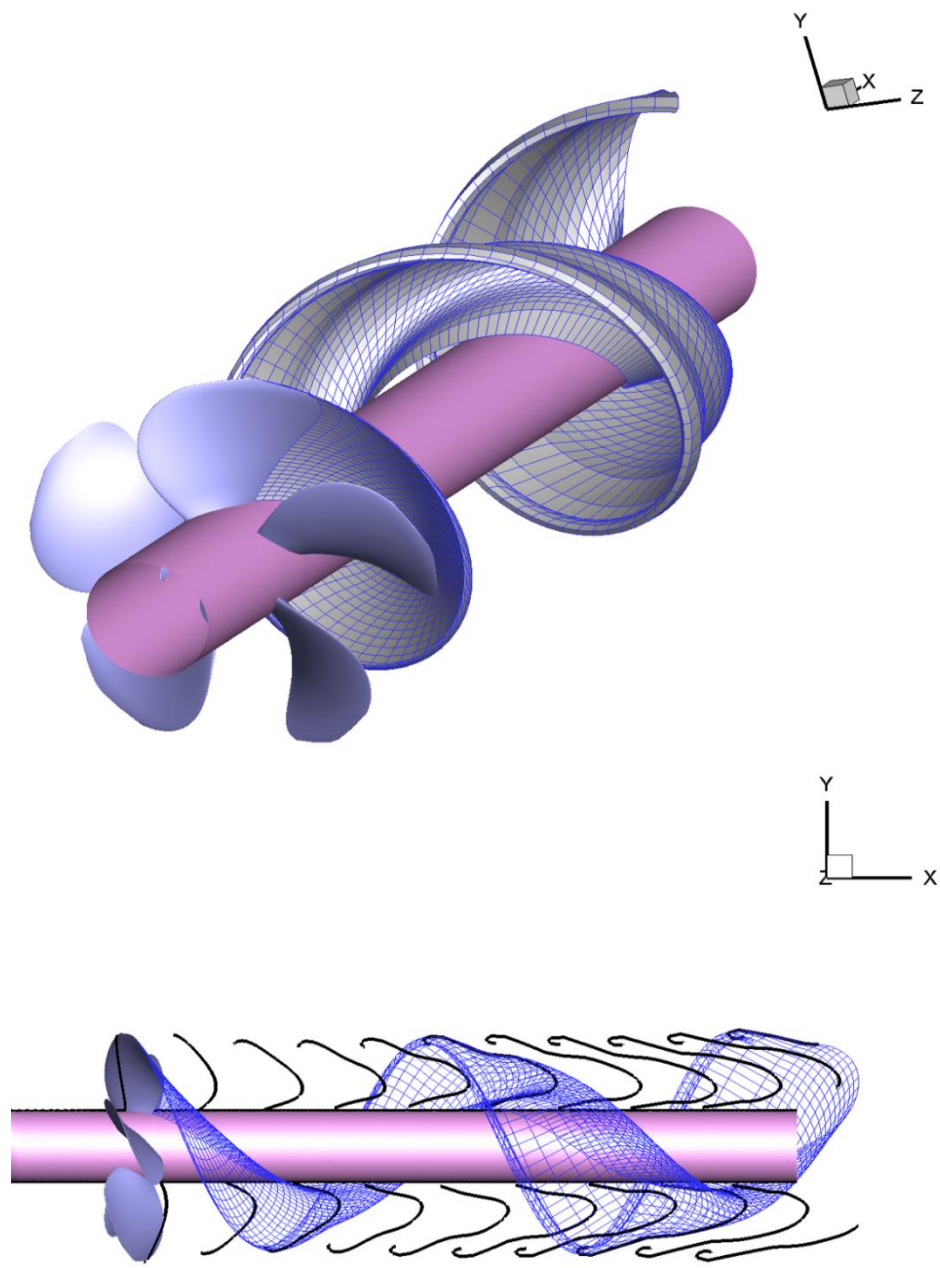


Figure 5. 4 Wake geometries aligned using FWA with 120 wake panels in uniform flow: $J_s = 1.14$.

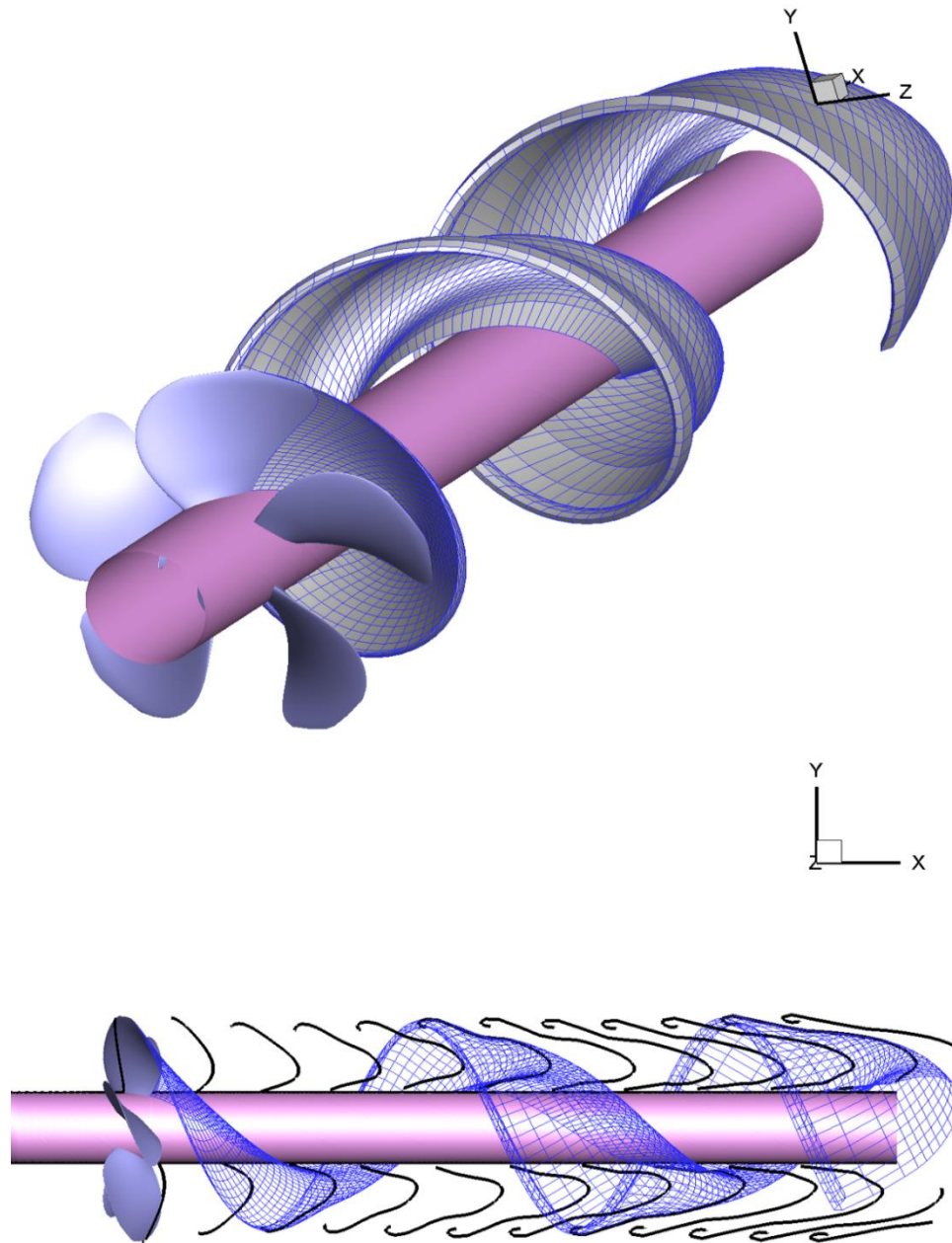


Figure 5.5 Wake geometries aligned using FWA with 140 wake panels in uniform flow: $J_s = 1.14$.

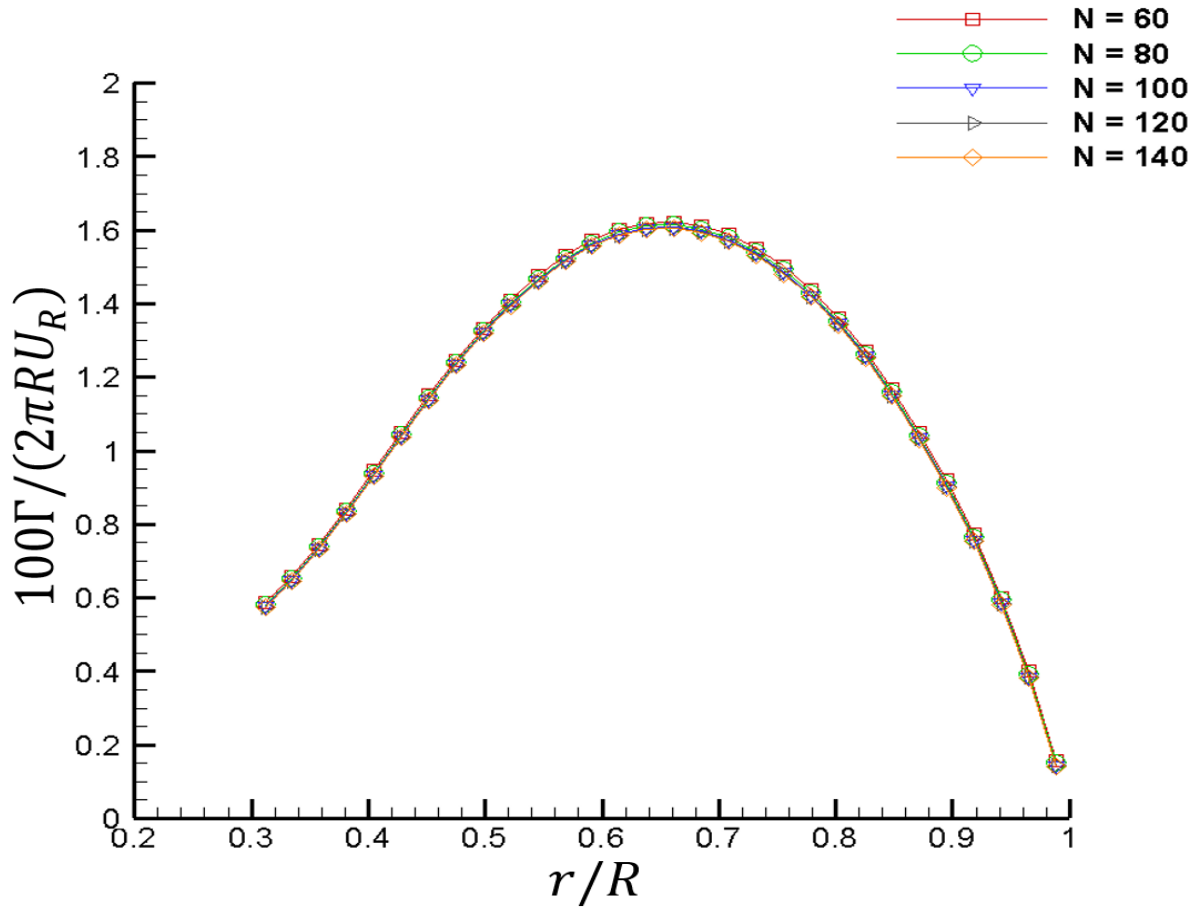


Figure 5.6 Convergence of circulation distribution over blade with number of wake panels for DTMB 4661 propeller: $\Delta t = 6^\circ$ and $J_s = 1.14$, $U_R = \sqrt{V_s^2 + (0.7n\pi D)^2}$.

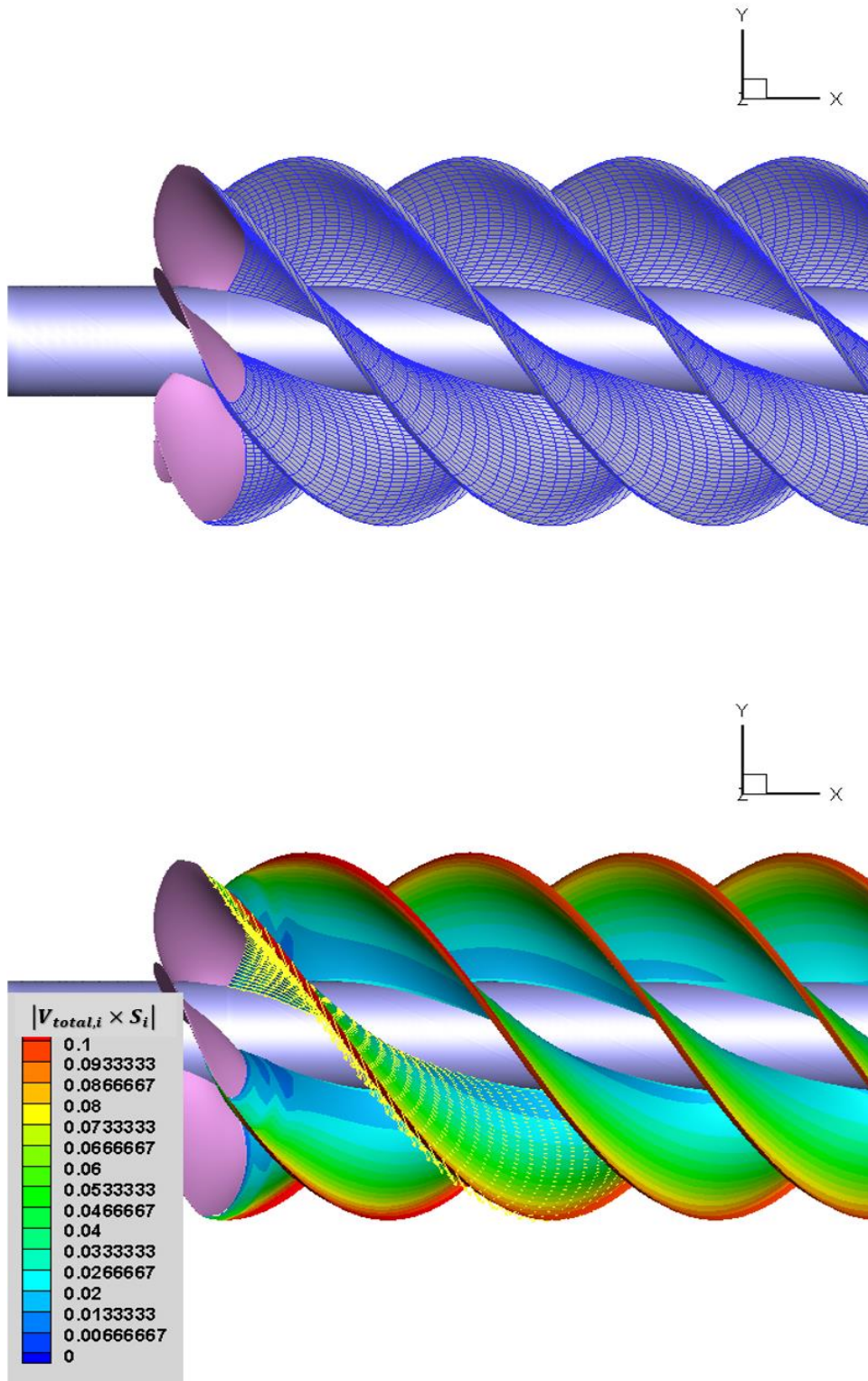


Figure 5.7 Convergence of wake panels at the first iteration in full wake alignment with 80 panels.

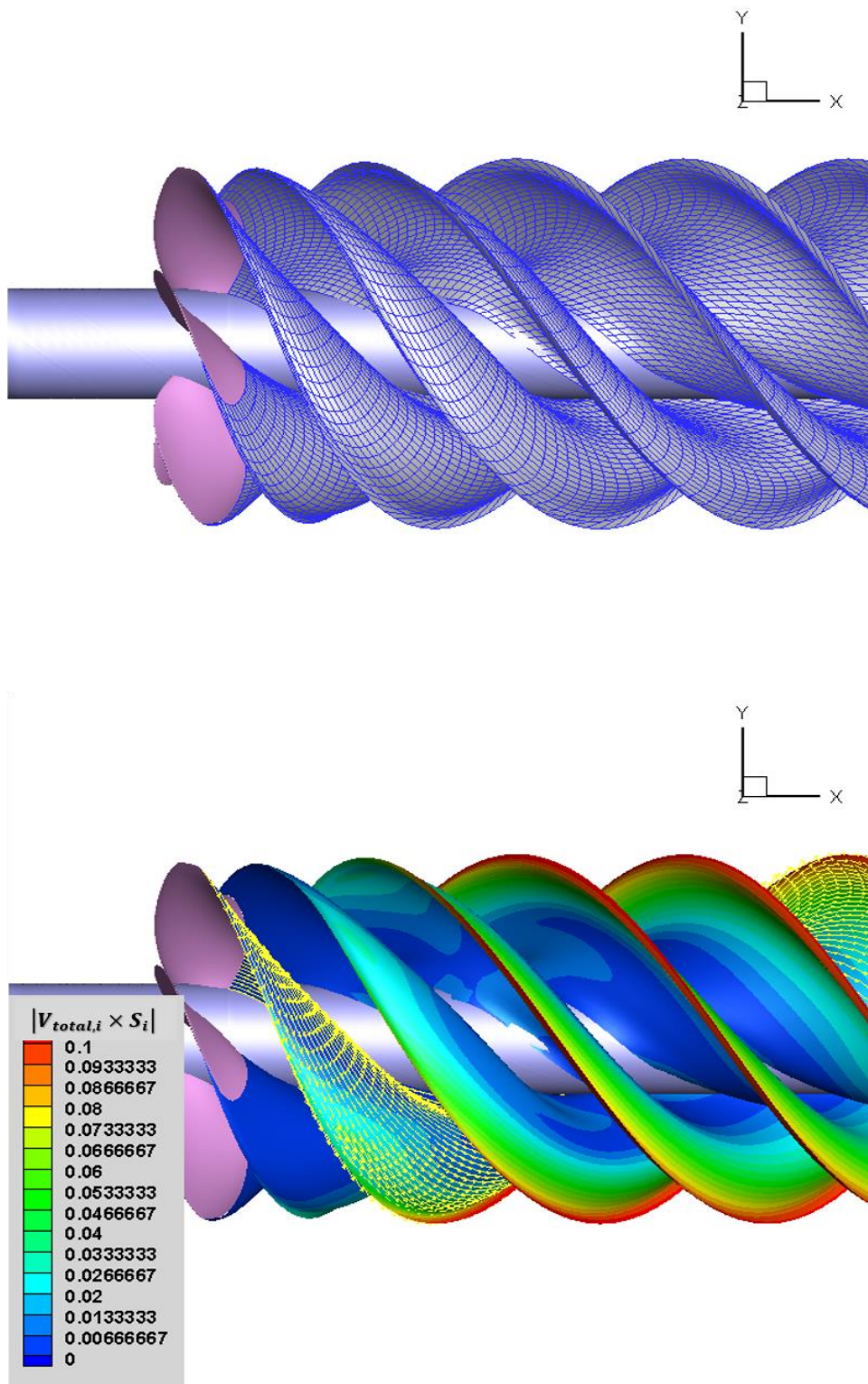


Figure 5.8 Convergence of wake panels at the second iteration in full wake alignment with 80 panels.

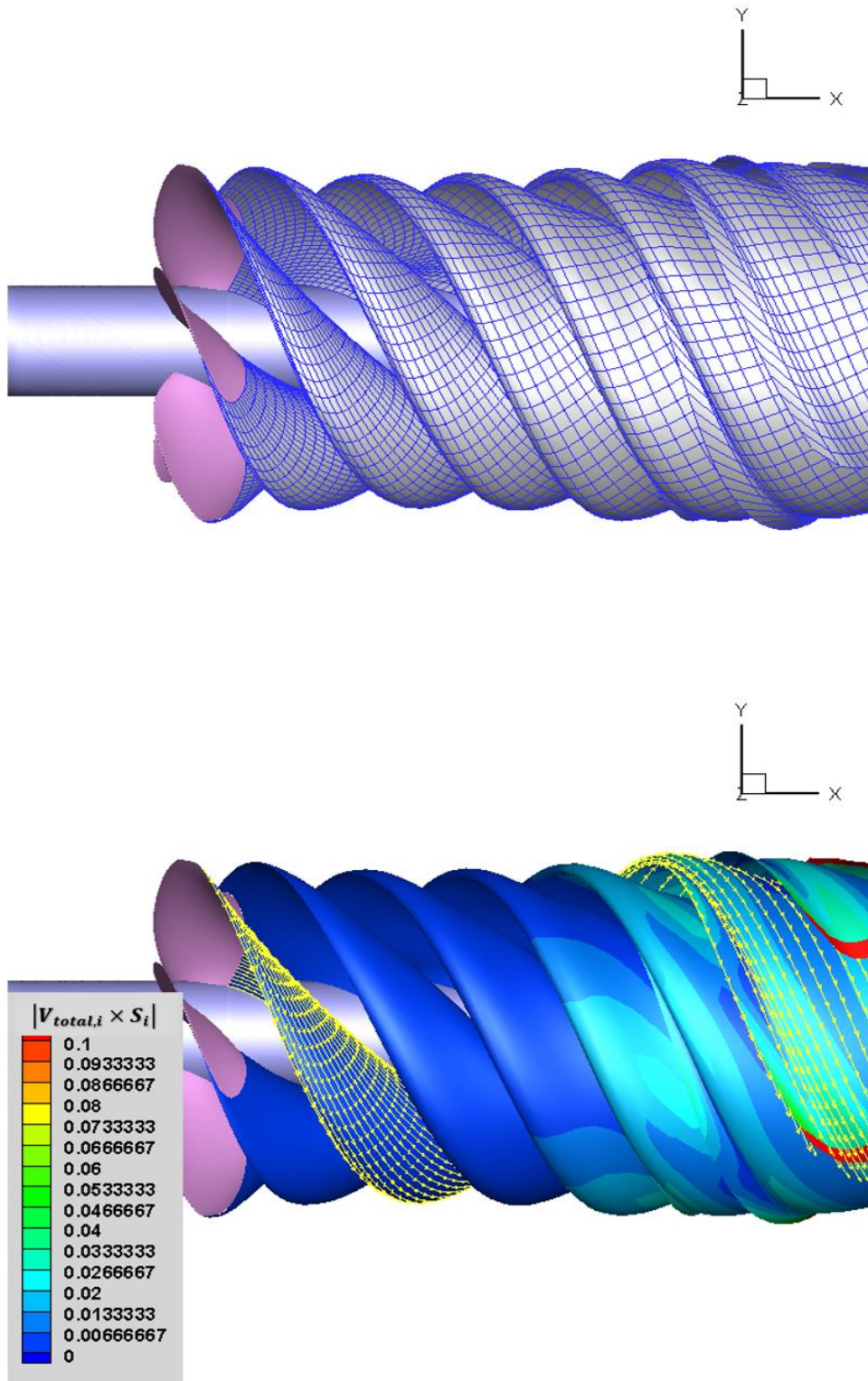


Figure 5.9 Convergence of wake panels at the fifth iteration in full wake alignment with 80 panels.

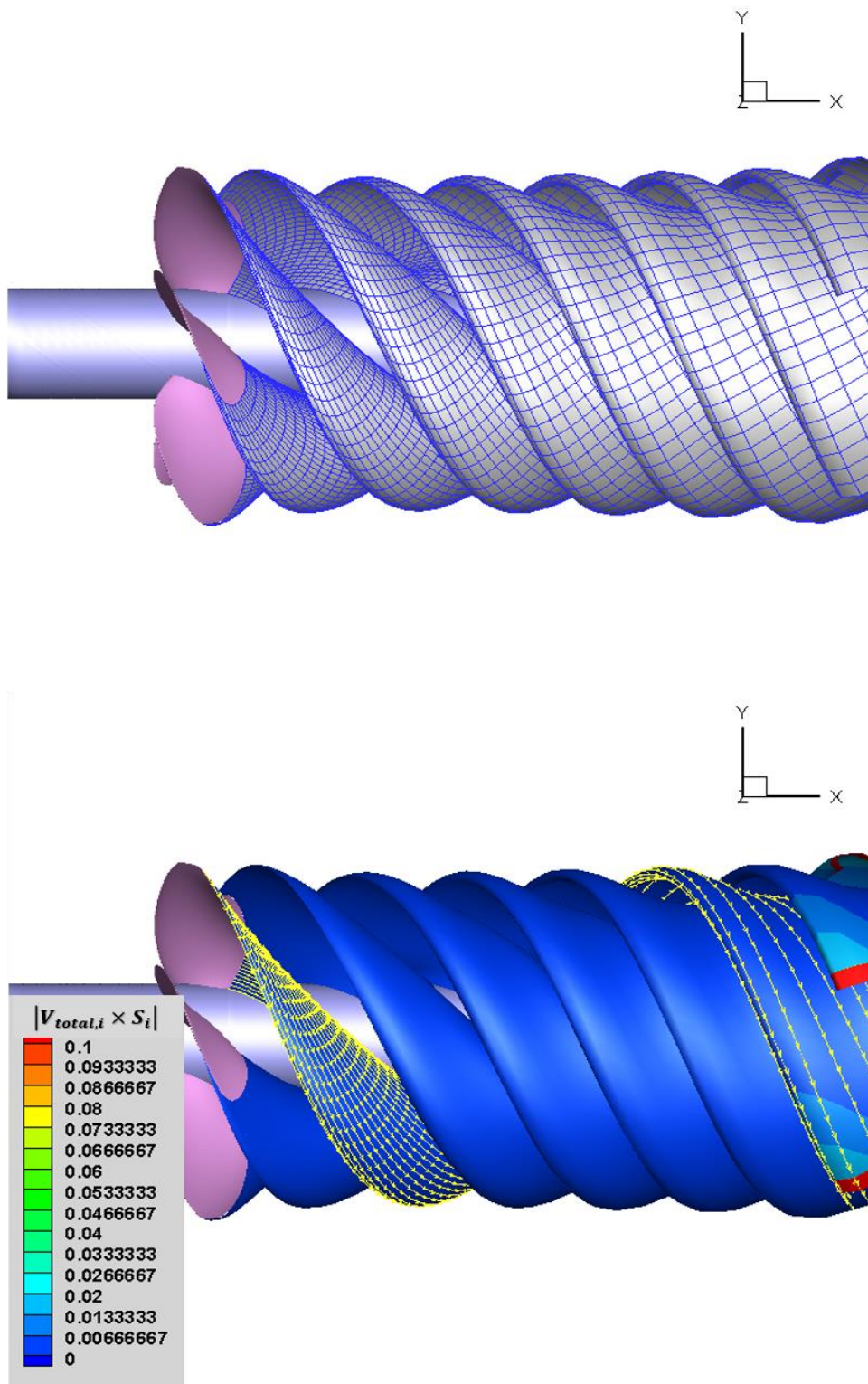


Figure 5.10 Convergence of wake panels at the eighth iteration in full wake alignment with 80 panels.

5.1.2 Non-uniform Inflow

Now, DTMB 4661 propeller is subject to the circumferentially averaged mean inflow, which is not uniform along the radial direction. Two extreme cases, i.e. one with its lowest and highest velocity near hub and blade tip respectively, and the other with the opposite composition, are adopted for this test. The numerical calculation is performed at design advance ratio, $J_s = 1.14$ and $F_n = 4.0$. Variations of the incoming velocity along the radial direction for each case are shown in Figure 5.11 and Figure 5.14.

As discussed in Chapter 3, the FWA has been modified such that it can consider the variation of incoming flow in steady state. Based on the modification, the emphasis of this test is on generating reasonable wake geometries, which correspond to the profiles of the circumferentially averaged mean inflow. Comparison of circulation distributions on blade between the three cases, i.e. uniform and two extreme cases, is presented in Figure 5.17. Apparently, peak value of the circulation is shifted toward the region where the velocity is minimum. Axisymmetric inflow *case II* (denotations are defined below) shows the lower peak value of circulation than *case I* since the minimum inflow velocity of *case II* is faster than that of *case I*.

Axisymmetric inflow case I

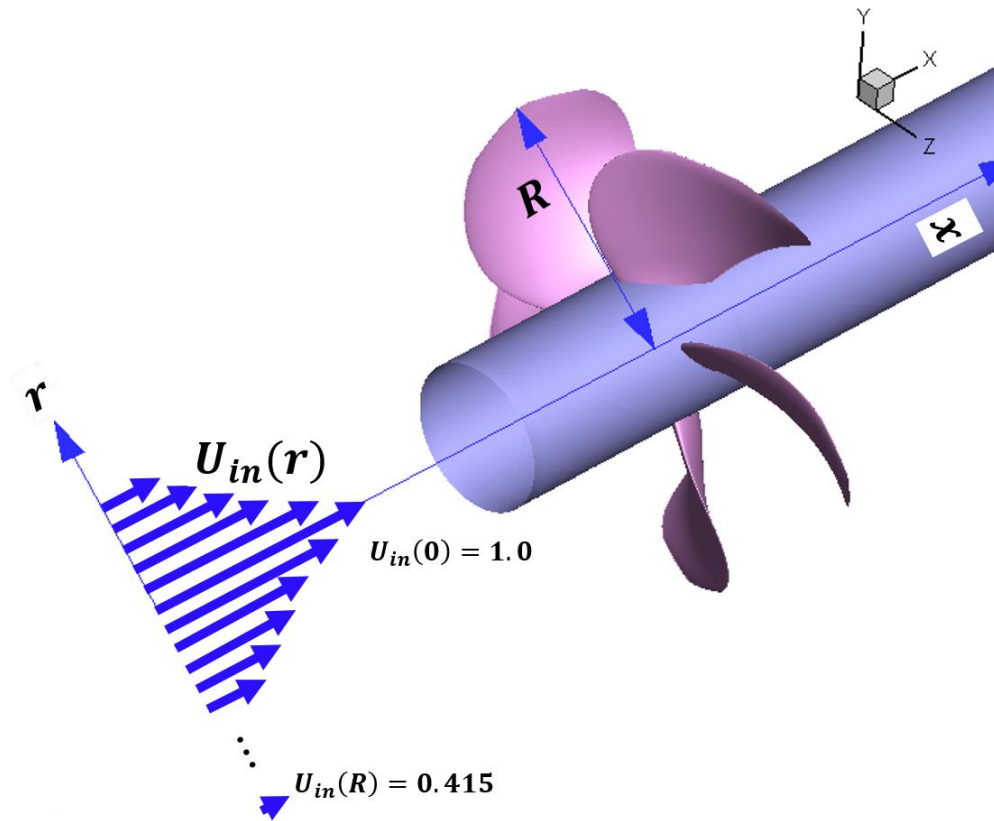


Figure 5.11 DTMB 4661 propeller in axisymmetric inflow, which has its highest and lowest velocity at near hub and blade tip, respectively.

Convergence history of full wake alignment is shown in Figure 5.12 and 5.13 with the cross products magnitude plotted. Only the key wake is presented and the other wakes are plotted on two-dimensional slices for clear view of the wake profile. The wake sheets are fully aligned up to one before the last strip with the magnitude of cross products less than 0.01 after the 13th iteration.

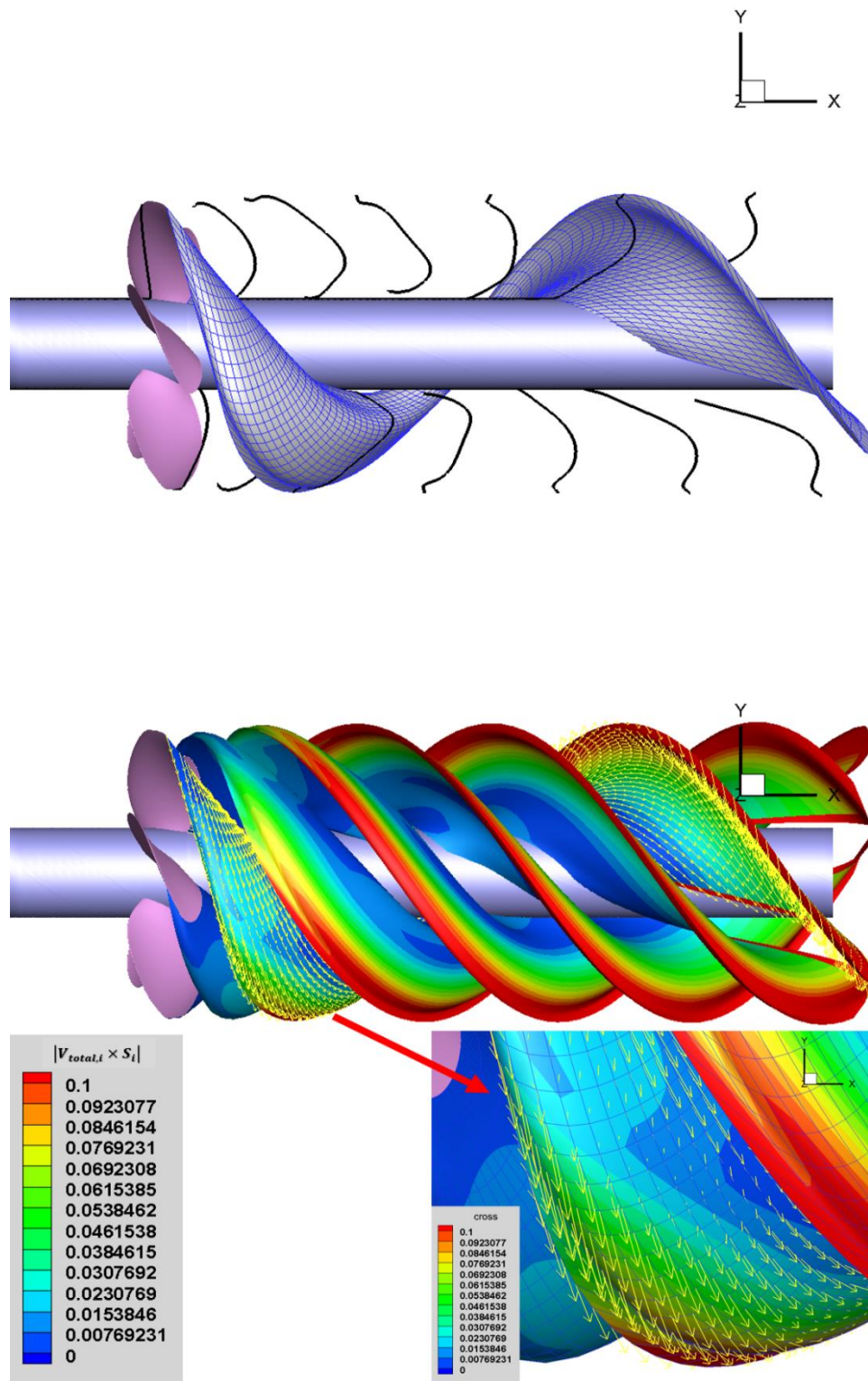


Figure 5.12 Convergence of wake panels at the second iteration in full wake alignment in axisymmetric inflow. Yellow arrow denotes the total velocity induced on the wake panel.

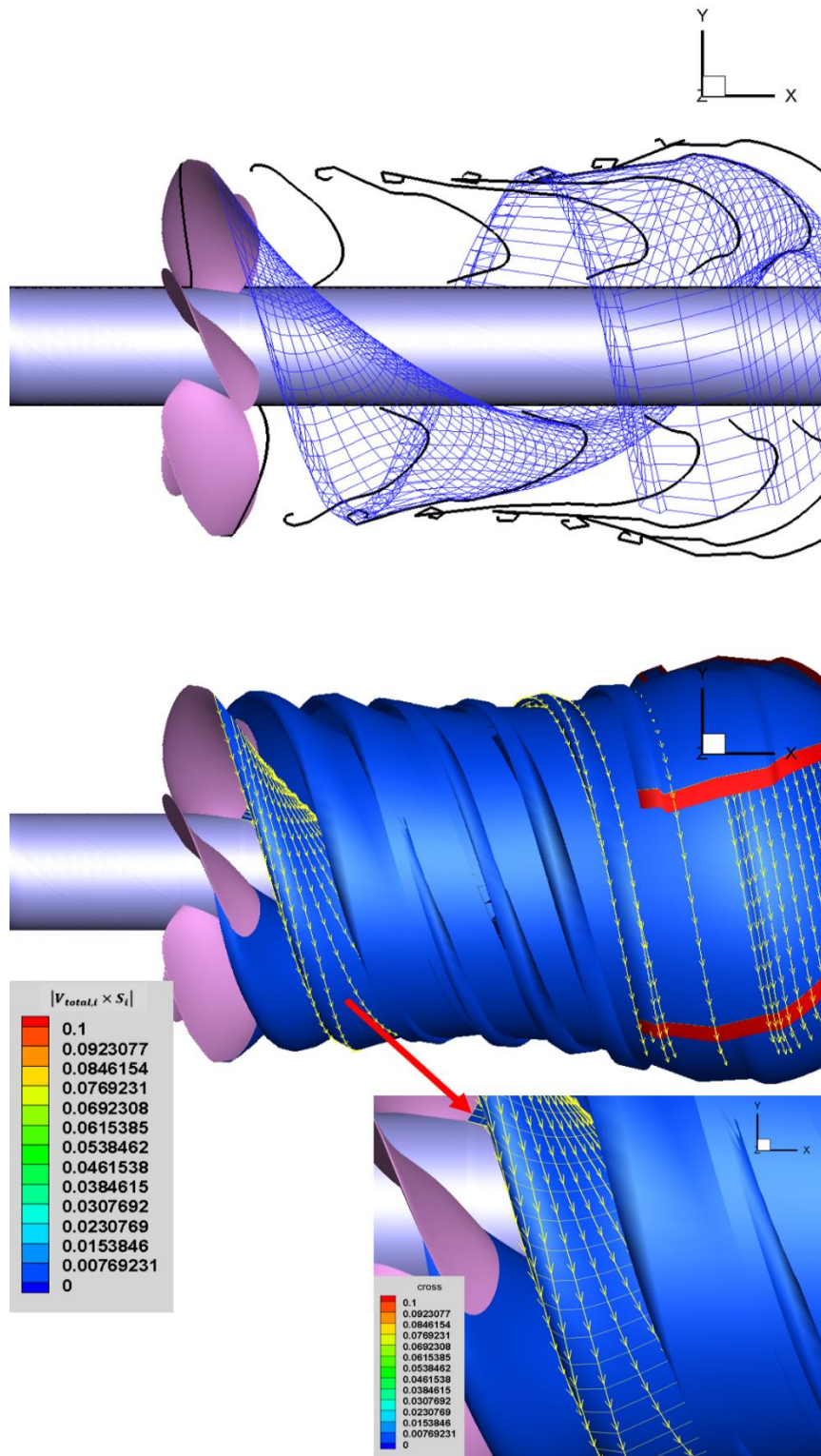


Figure 5.13 Convergence of wake panels at the 13th iteration in full wake alignment in axisymmetric inflow. Yellow arrow denotes the total velocity induced on the wake panel.

Axisymmetric inflow case II

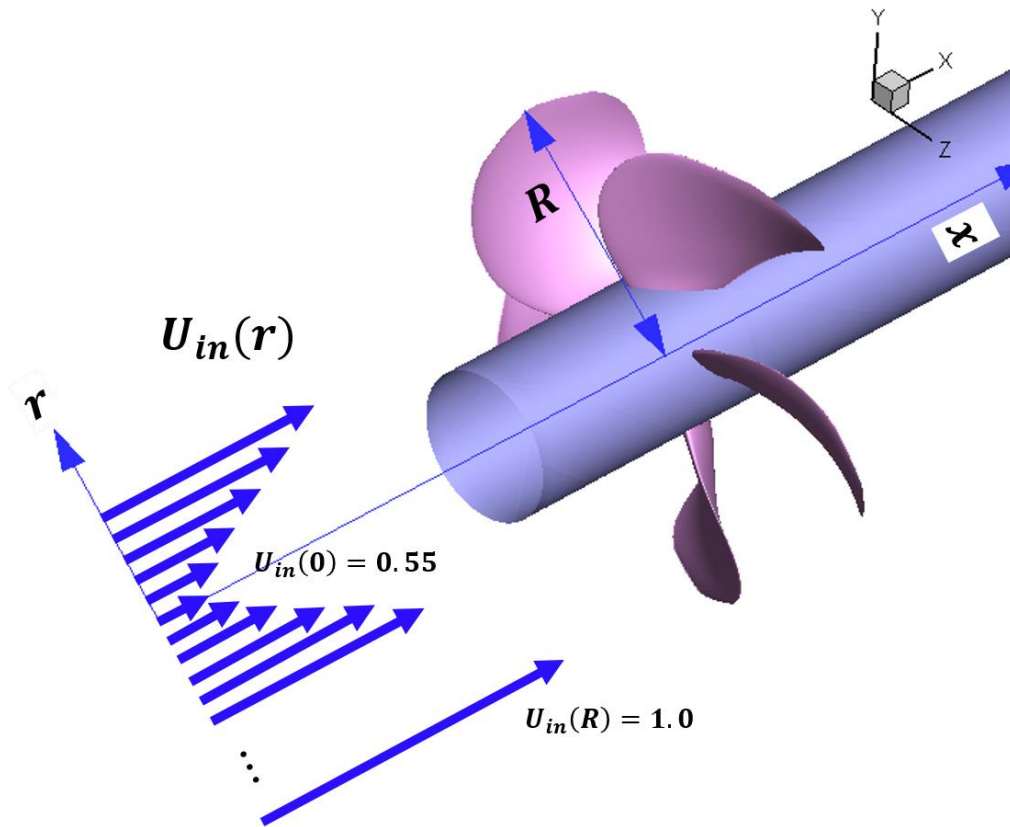


Figure 5.14 DTMB 4661 propeller in axisymmetric inflow, which has its highest and lowest velocity at the blade tip and near hub, respectively.

Convergence history of full wake alignment is shown in Figure 5.15 and 5.16 with the cross products magnitude plotted. Only the key wake is presented and the other wakes are plotted on two-dimensional slices for clear view of wake profile. The wake sheets are fully aligned up to one before the last strip with the magnitude of cross products less than 0.01 after the 19th iteration.

Compared to *case I*, *case II* went through more iterations before satisfying the convergence criterion. It is because of the wake panels with the low inflow velocities around hub. As shown in Figure 5.15, wake panels which have the low inflow velocities stay closer to hub surface. This

allows the perturbation velocities from hub to intensively perturb the wake panels in close distance, requiring FWA to go through more iterations to fully account for those velocities. Eventually, it is shown that the wake panels are fully aligned to the local velocity after the 19th iteration.

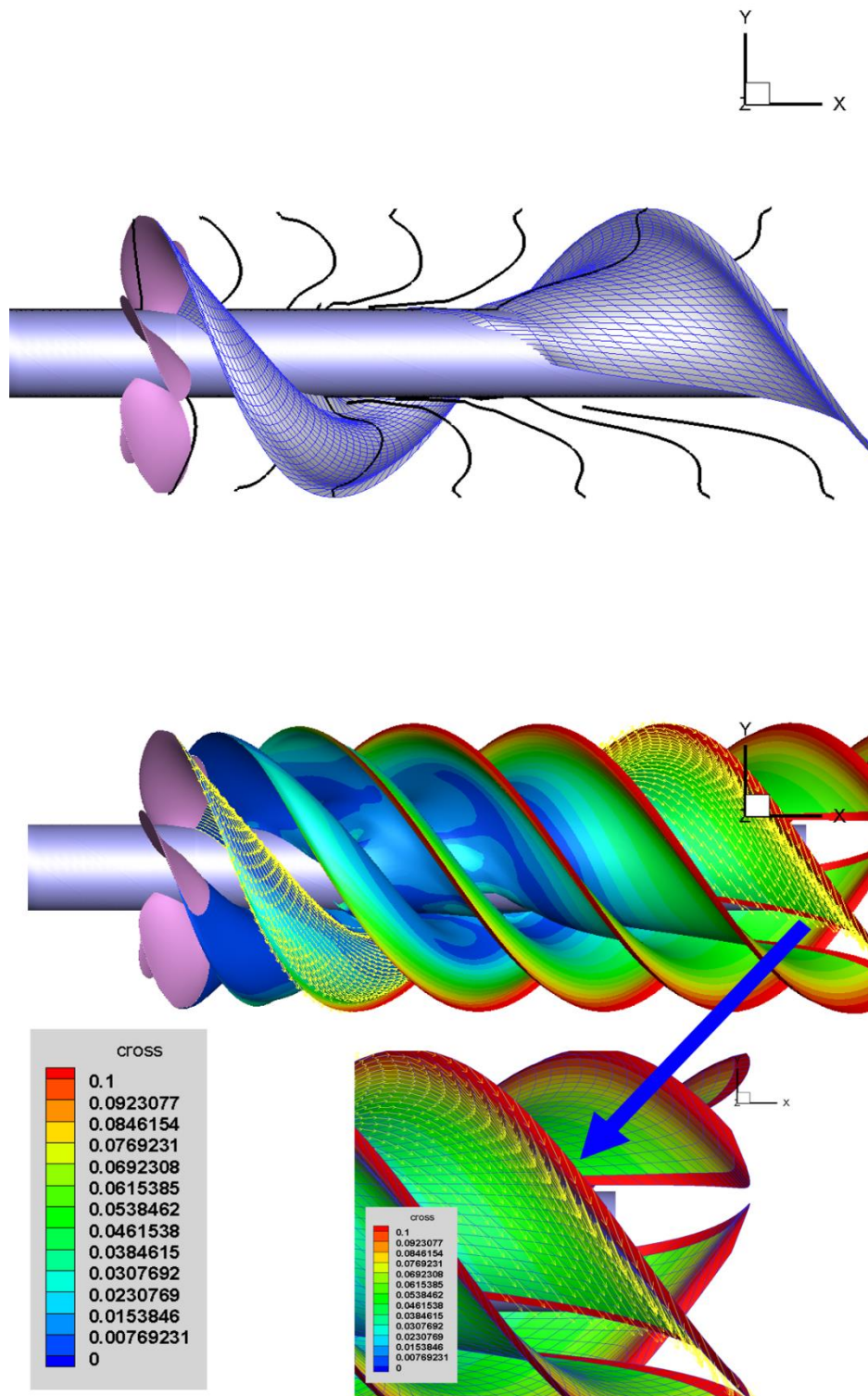


Figure 5.15 Convergence of wake panels at the second iteration in full wake alignment in axisymmetric inflow. Yellow arrow denotes the total velocity induced on the wake panel.

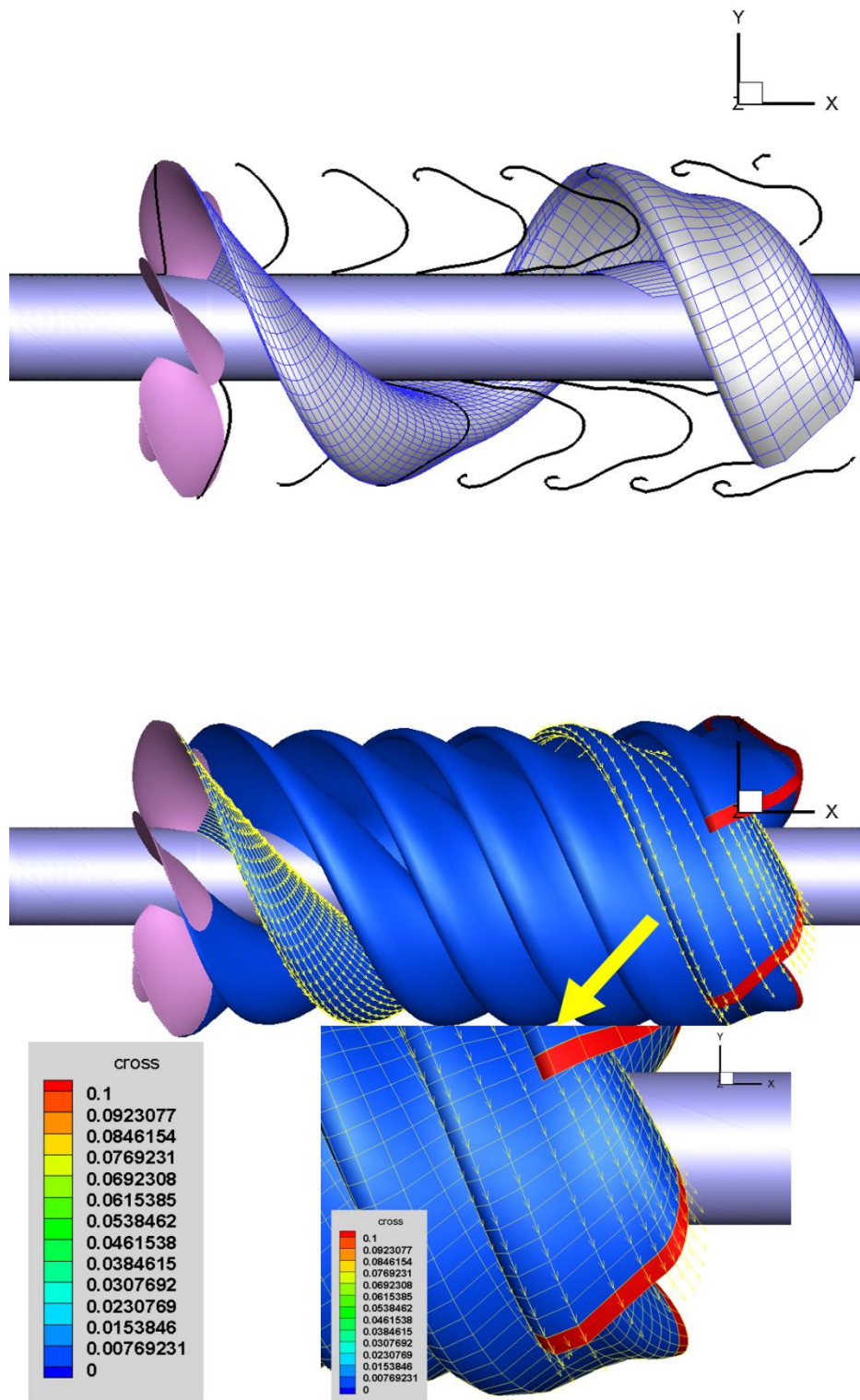


Figure 5.16 Convergence of wake panels at the 19th iteration in full wake alignment in axisymmetric inflow. Yellow arrow denotes the total velocity induced on the wake panel.

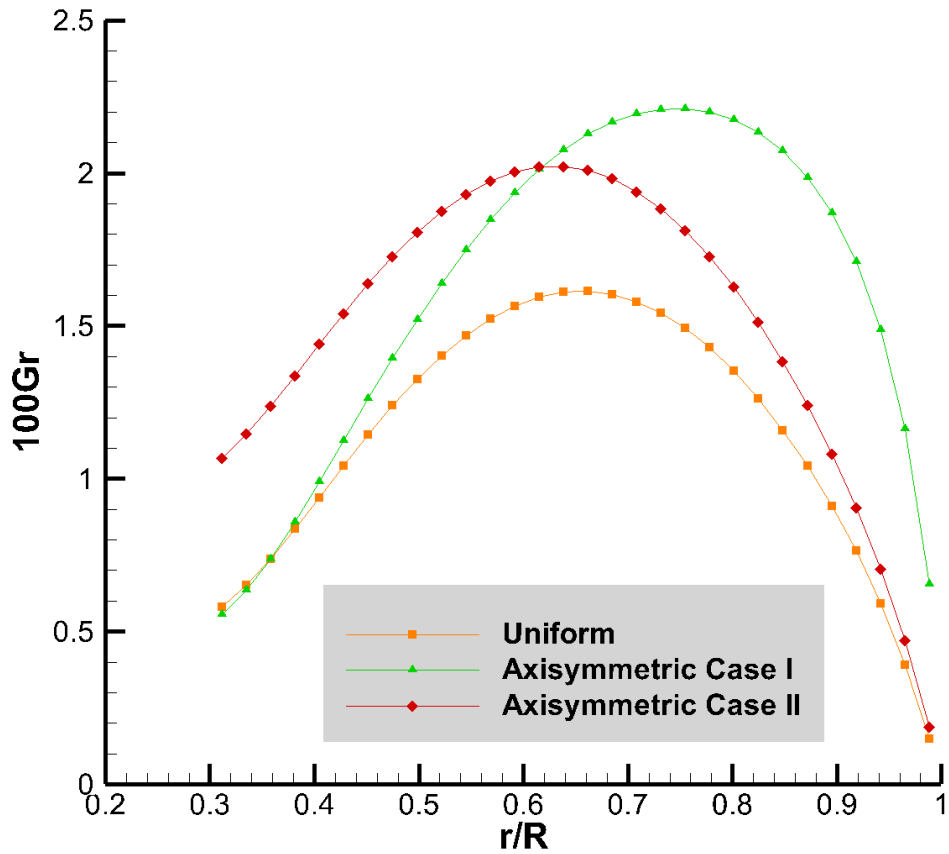


Figure 5.17 Circulation distribution over blade using uniform and non-uniform inflow for DTMB 4661 propeller: $\Delta t = 6^\circ$ and $J_s = 1.14$, $U_R = \sqrt{V_s^2 + (0.7n\pi D)^2}$. Cases I & II correspond to non-uniform inflows as described in the text.

5.2 Unsteady Wake Alignment

5.2.1 Uniform Inflow

Before moving to unsteady alignment in 10° inclined shaft flow, unsteady alignment model is firstly applied in uniform flow. Figure 5.18 shows the circulation on the blade from steady and unsteady mode calculations. Unsteady mean circulation corresponds very well to unsteady circulations from 60-time steps (one time step is equal to 6°), as expected. Steady circulation is in good agreement with unsteady circulation in general, although very little deviation is detected toward the blade tip. It is because of the difference in alignment algorithm between the two different modes (FWA for steady calculation and trapezoidal rule (Equation (3.22)) for unsteady calculation). The same trend can be found in Figure 5.19, which shows that the thrust and torque coefficients from steady mode are slightly underpredicted than those from unsteady mode, even though not considerably.

Wake geometries in unsteady mode are identical between each time step in uniform flow. Therefore, time step at zero angle is adopted for a comparison with steady result in Figure 5.20. As it can be seen, wake geometries are in good agreement.

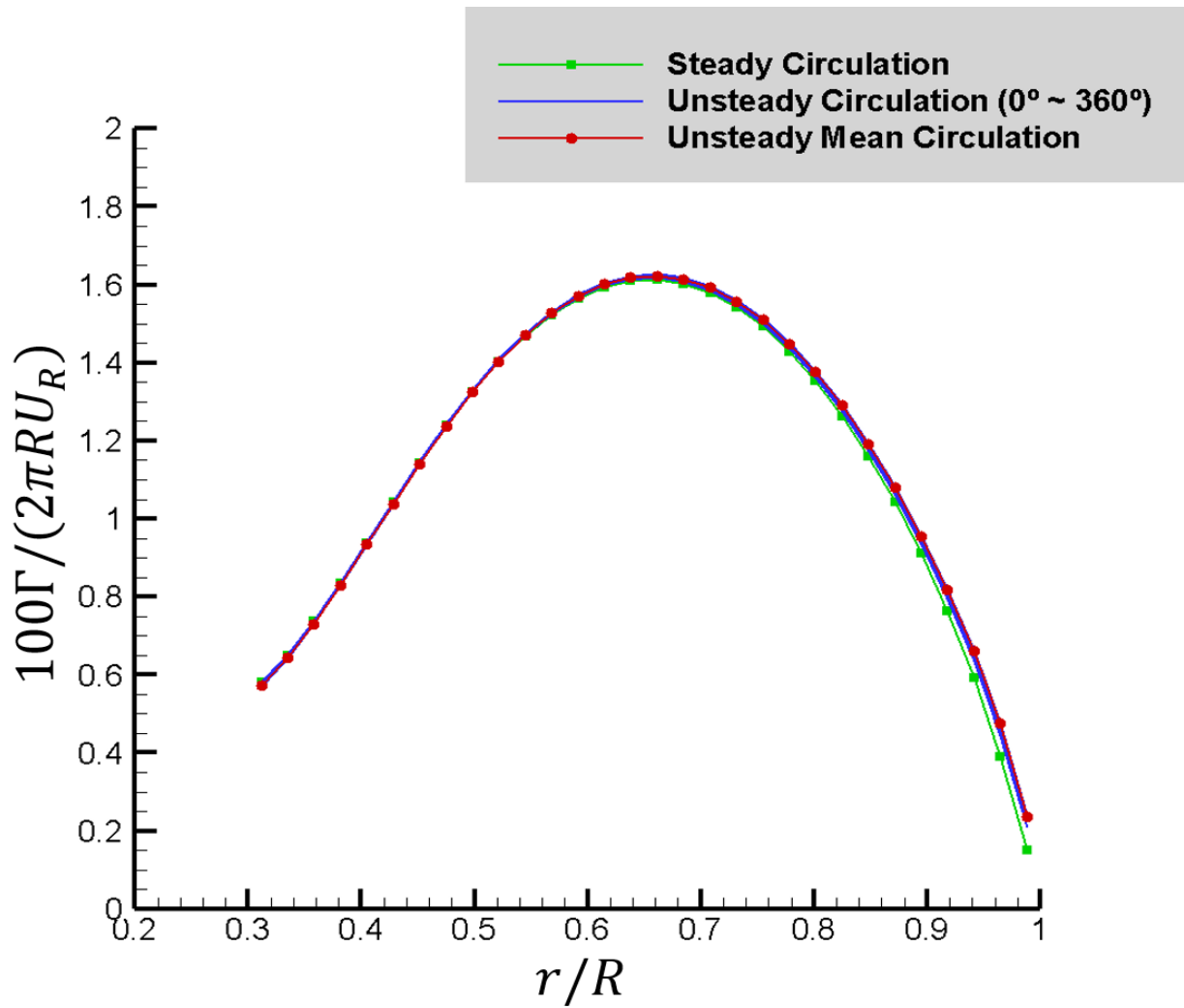


Figure 5.18 Circulation distribution on the blade predicted by steady and unsteady mode using DTMB 4661 propeller with 80 wake panels: $\Delta t = 6^\circ$ and $J_s = 1.14$.

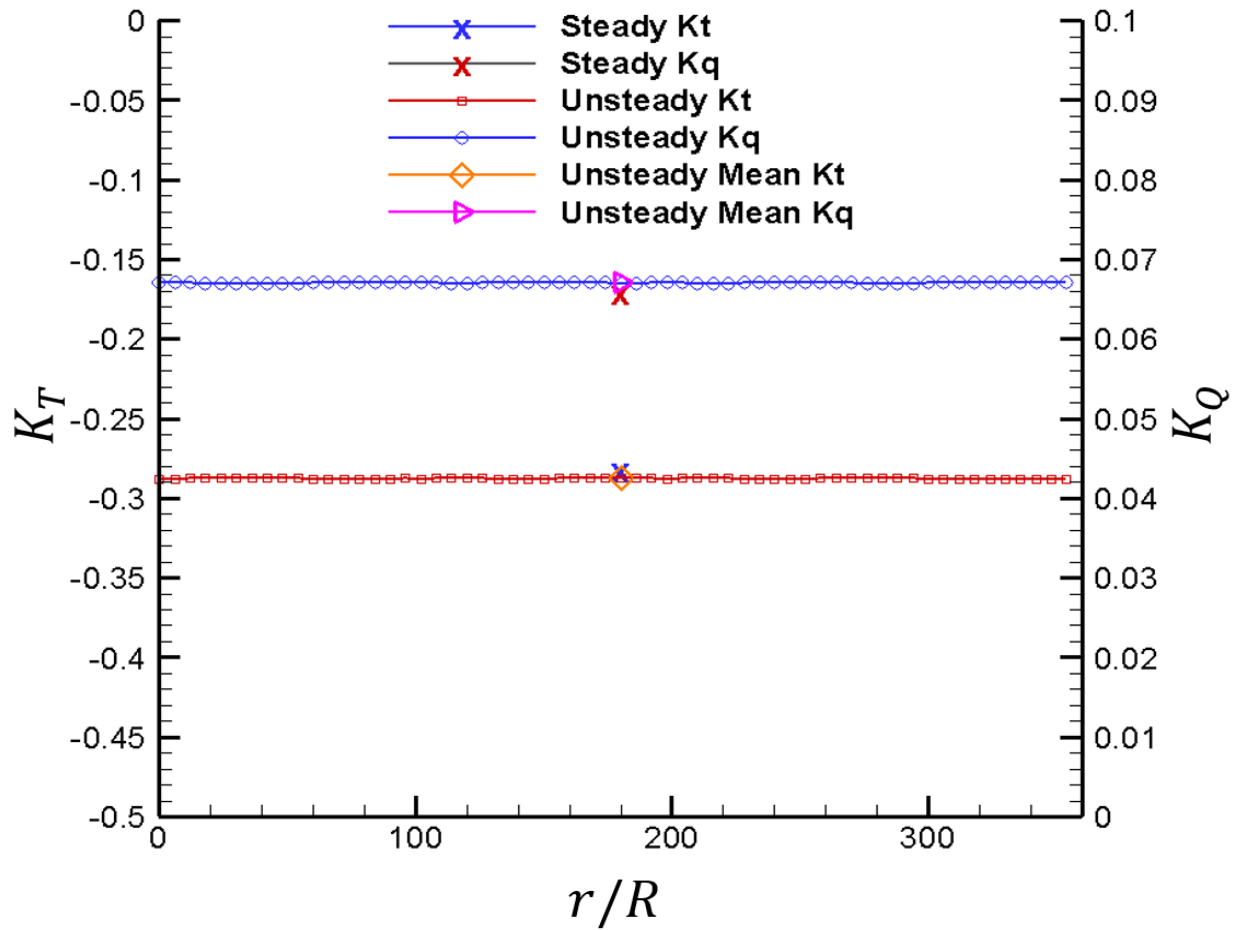


Figure 5.19 Thrust and torque coefficients predicted by steady and unsteady modes using DTMB 4661 propeller with 80 wake panels: $\Delta t = 6^\circ$ and $J_s = 1.14$.

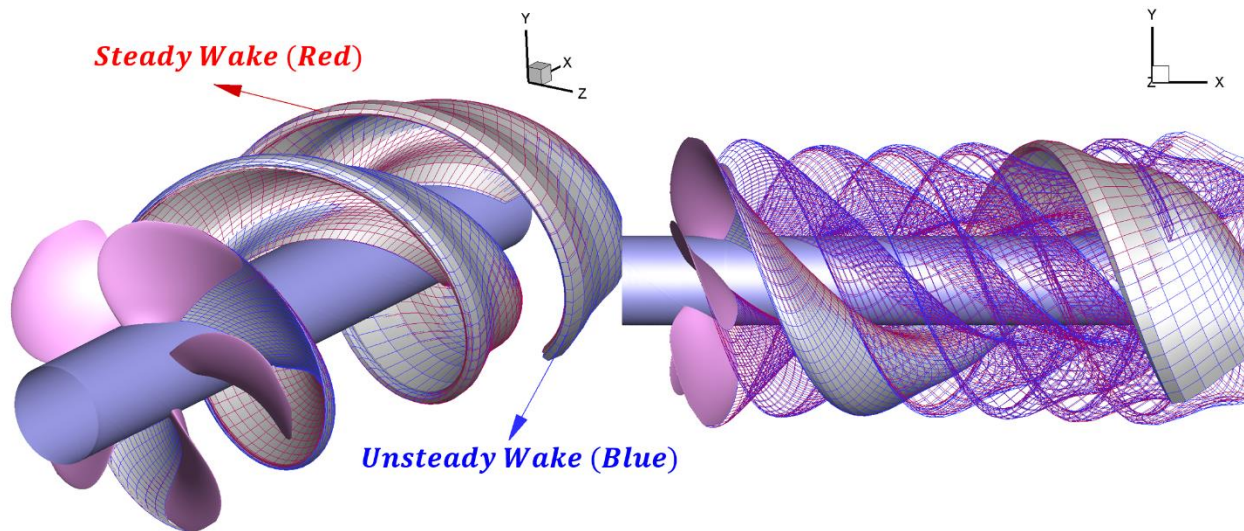


Figure 5.20 Wake geometry predicted by steady (red) and unsteady (blue) alignment modes using DTMB 4661 propeller with 80 wake panels: $\Delta t = 6^\circ$ and $J_s = 1.14$. Only the two wake sheets are presented for clarity in the left figure.

5.2.2 Inclined Shaft Flow

The geometrical arrangement in the experiments [Boswell et al. 1984] is presented in Figure 5.21. As shown, the direction of incoming flow is in horizontal direction, and the shaft is inclined with a certain angle. In panel method, however, the axis of shaft is horizontal, and the inflow comes into the propeller plane through the inclined angle. Quadratic hub that closes upstream, and cylindrical hub that has the increasing radius into downstream are used in the experiments.

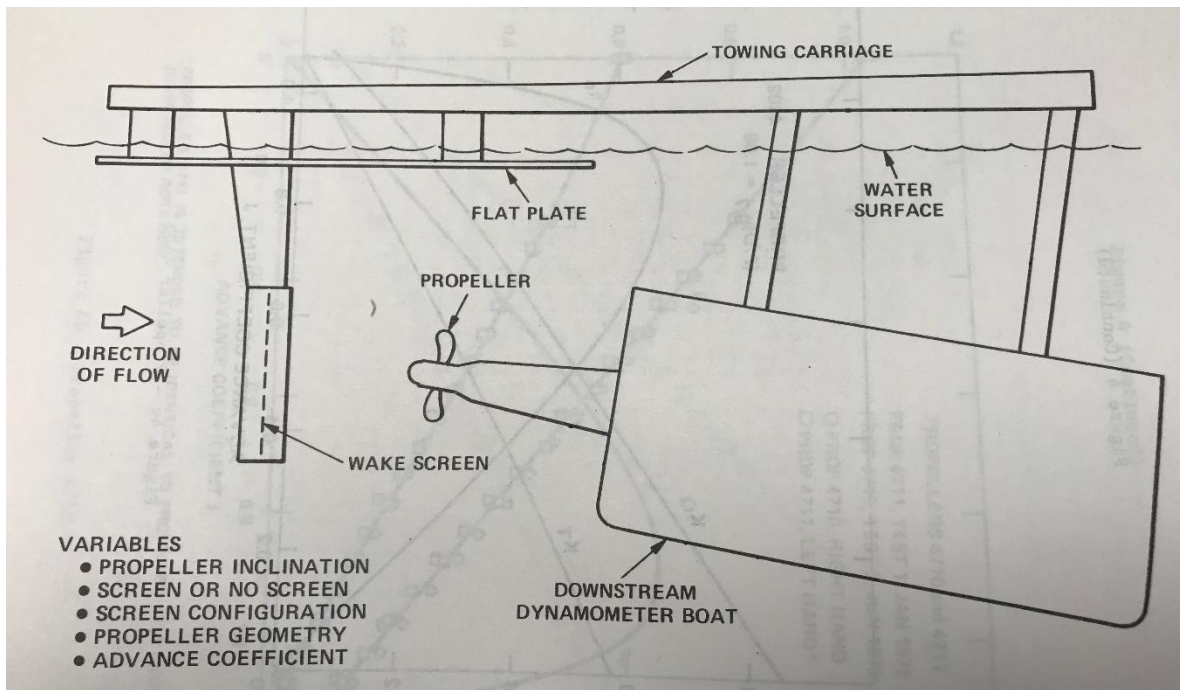


Figure 5.21 Experimental arrangement of 4661 propeller in inclined shaft flow, taken from Figure 5 of [Boswell et al. 1984].

Different from the axisymmetric inflow, inclined shaft flow inherently accompanies the interaction between the inclined shaft and wake sheets. Therefore, the predicted propeller performance might differ depending on the hub geometry. In the case of the inclined shaft with infinite length, especially, penetration of wake panels might occur on the hub surface. Modeling wake sheet around the inclined shaft might use the same algorithm, which was used for the numerical simulation of propeller/rudder interaction [L. He 2010].

In the real case, even short hub with conical ends might require a numerical modeling of hub vortex cavitation, which needs to be handled as extended hub geometry as shown in Figure 5.22. Hub vortex cavity is a vortex type cavitation, which occurs around rear part of hub due to shedding vortex from the blade roots. The detachment point where vortex cavity starts to leave from hub might be determined by the algorithm, which was introduced by [Kinnas et al. 1997;

Mueller and Kinnas 1997; Mueller 1998; Mueller and Kinnas 1999; Young and Kinnas 1999b, 2001a].

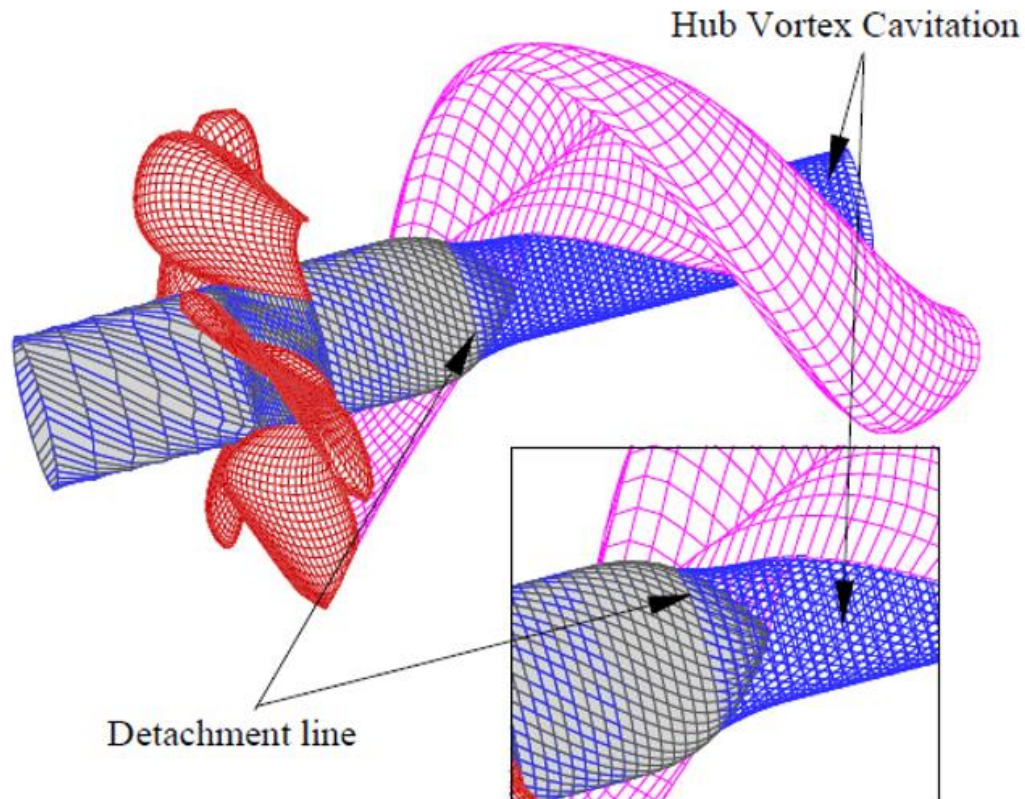


Figure 5.22 Modeling of hub vortex cavitation, taken from Figure 5.1 of [H. Lee 2002].

In this thesis, four different hub geometries are adopted to investigate the effect of hub geometry on the unsteady performance of 4661 propeller as follows:

- (a) Hub 1: Quadratic hub that closes downstream but opens upstream.
- (b) Hub 2: Elliptic hub that closes both upstream and downstream.
- (c) Hub 4: Quadratic hub that closes upstream but opens downstream.
- (d) Hub 5: Infinite hub that has both ends opened.

When the penetration occurs, the radial distance of wake panels which are inside hub surface is controlled to be the same as that of hub radius in this thesis. Wake panels behind the short hub are

free from a physical barrier, which exists if infinite hub is used. However, the influence of the short hub on wake sheets is still considered in terms of the perturbation velocity. The projected views of the aligned wakes with each hub geometry are shown in Figure 5.23, which clearly shows the inclination of the wake sheets.

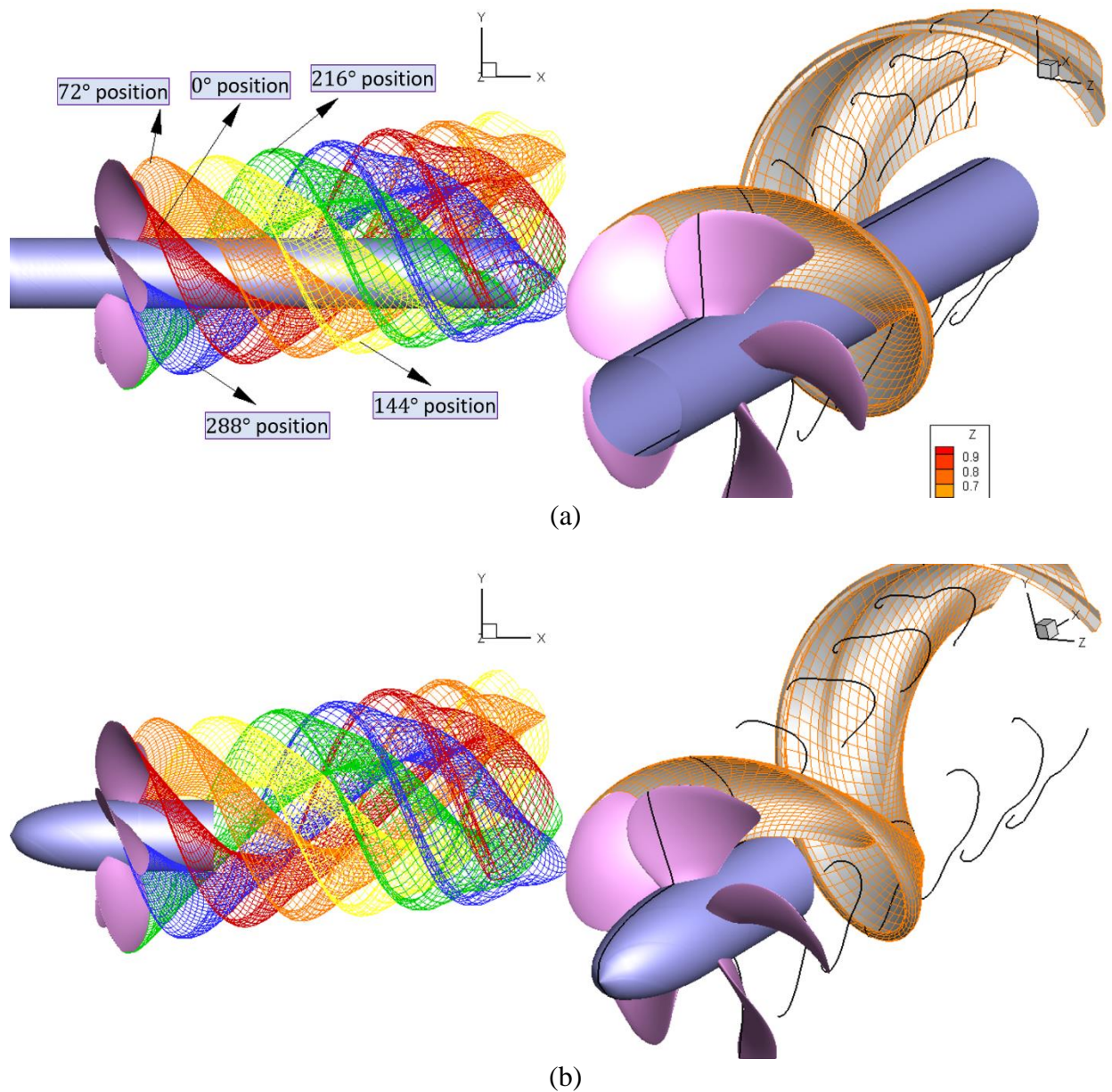


Figure 5.23 (Continued next page).

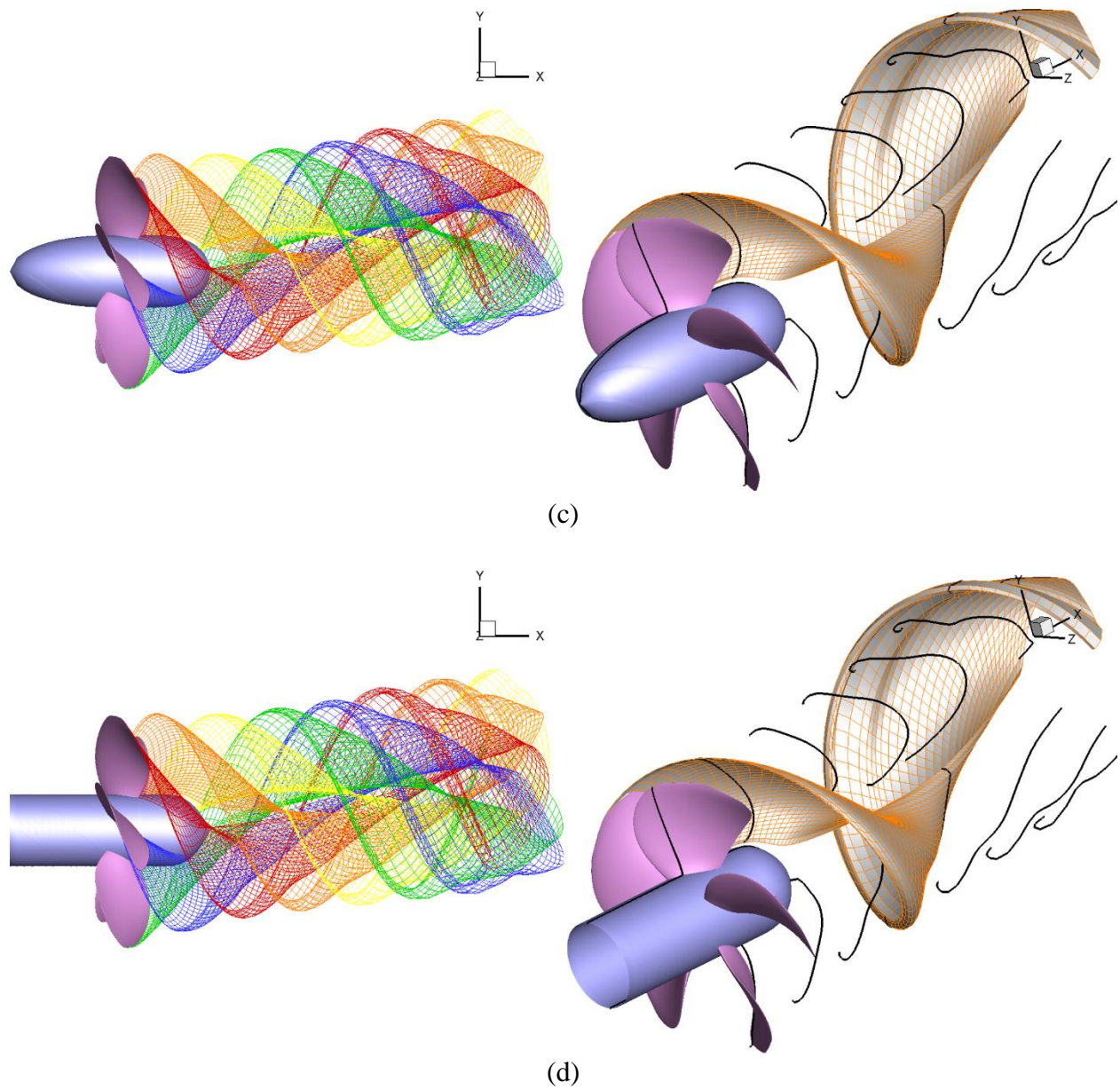


Figure 5.23 The projected view of aligned wake geometries for DTMB 4661 propeller with (a) Hub 5, (b) Hub 4, (c) Hub 2, and (d) Hub 1: $J_s = 1.14$ and $\alpha = 10^\circ$.

Convergence study is performed on the predicted thrust and torque coefficients with number of wake panels in Figure 5.24. As shown, steady forces for all hub geometries seem to converge with sufficient panel numbers more than 100. Based on this result, wake sheet with 100 panels is used for the correlation with the experiments and other methods. The predicted K_T and

K_Q from Hub 5 and Hub 2 show the biggest difference, and those from Hub 1 and Hub 4 are located in between with about the same values each other. Unsteady and unsteady mean forces are also shown in Figure 5.25. Their magnitudes show the same trend as the steady forces.

Figure 5.26 shows the first harmonic amplitudes of the forces and moments acting on one the blade of DTMB 4661 propeller in inclined angle of $\alpha = 10^\circ$. The evaluated values are from the panel method (indicated by Current Method in the legend of figure), experiments by [Boswell et al. 1984], and the vortex lattice method (VLM) by [Kinnas and Pyo 1997]. As shown, the axial forces predicted by VLM shows very good correlations with those from the experiments, although VLM overpredicts at lower advance ratios. The panel method overpredicts axial forces and tangential moments compared to the experimental values. However, the panel method predicts better the tangential force and the axial moment than VLM. Among the hub geometries that panel method used, HUB 2 shows the best correlation of the force and moments with the experiments, although the predicted values using the other hub geometries are not significantly different from those using HUB 2. For the lowest advance ratio, the forces and moment predicted by panel method show better correlations with the experiments than those predicted by VLM. Now that the panel method in this study considers the incoming velocity as a constant with 10° of inclination, the detailed variation on the inflow due to the experimental environment might not be fully considered. The deviation observed here, therefore, might be further improved by taking into account the experimental conditions as mentioned in [Boswell et al. 1984] more accurately.

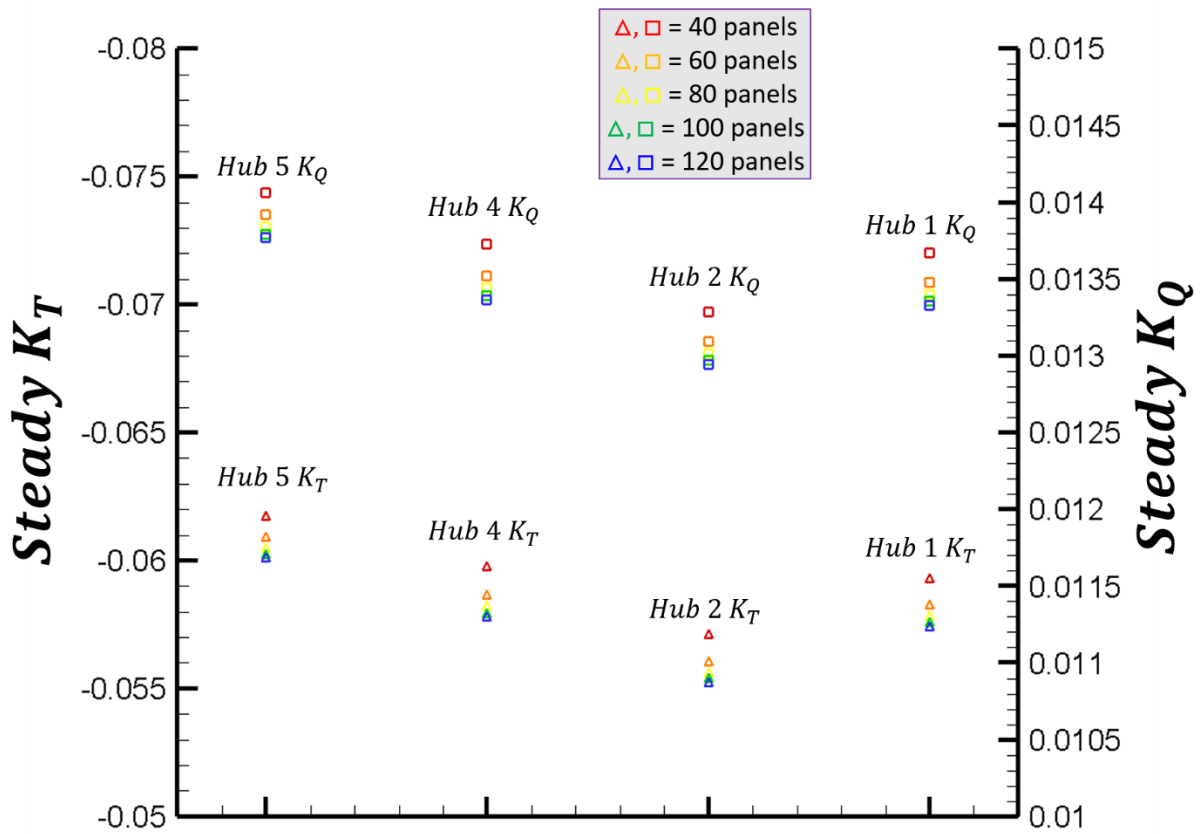


Figure 5.24 Convergence of the predicted steady thrust and torque coefficients using DTMB 4661 propeller with number of wake panels for four different hub geometries: $\Delta t = 6^\circ$ and $J_s = 1.14$.

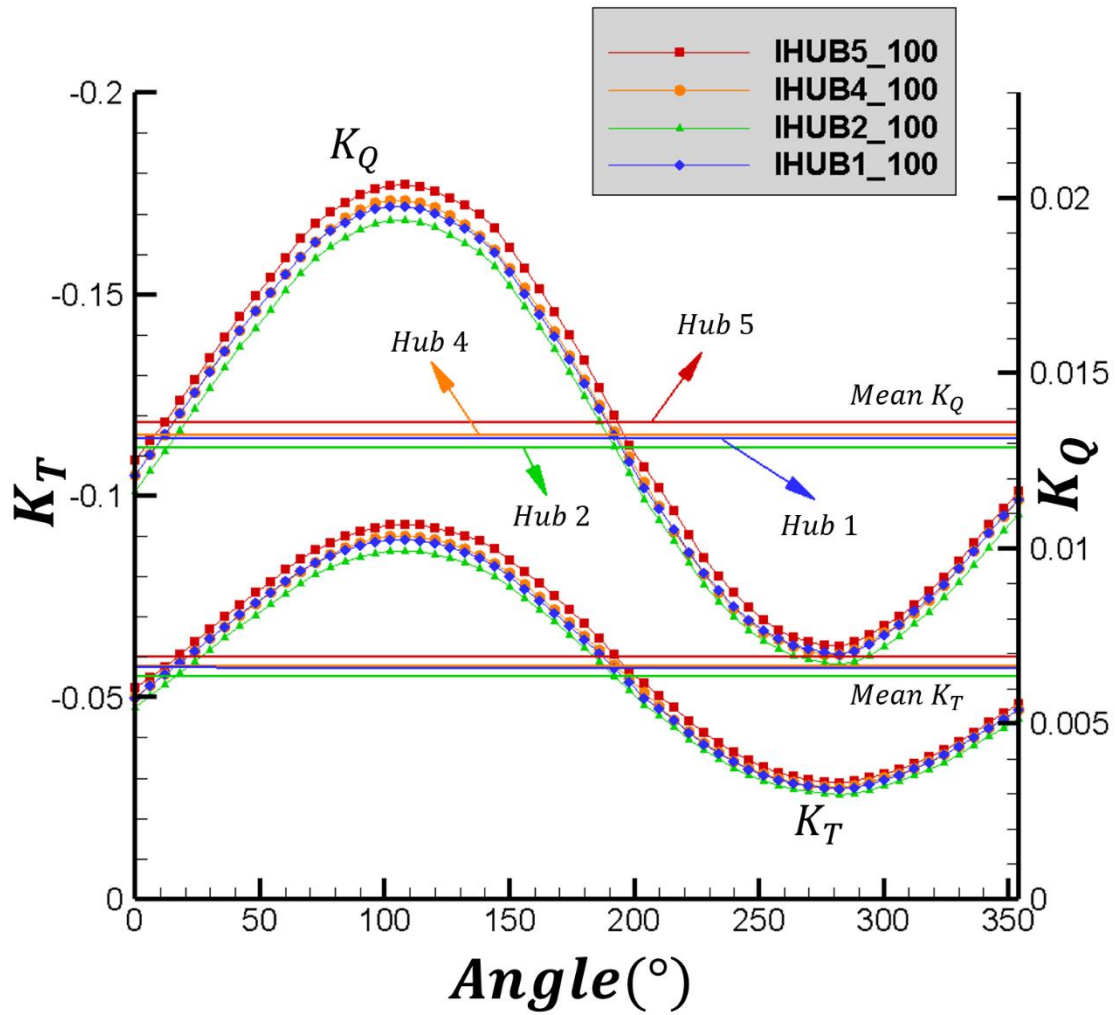


Figure 5.25 Unsteady and mean thrust and torque coefficients using DTMB 4661 propeller using four different hub geometries: $\Delta t = 6^\circ$ and $J_s = 1.0$.

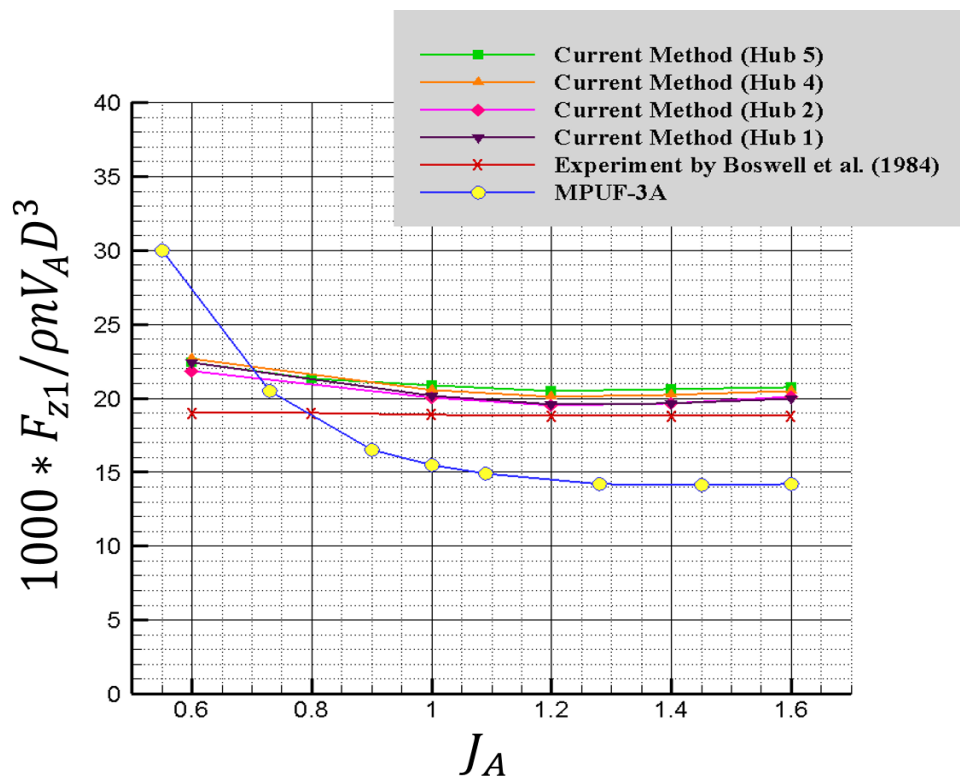
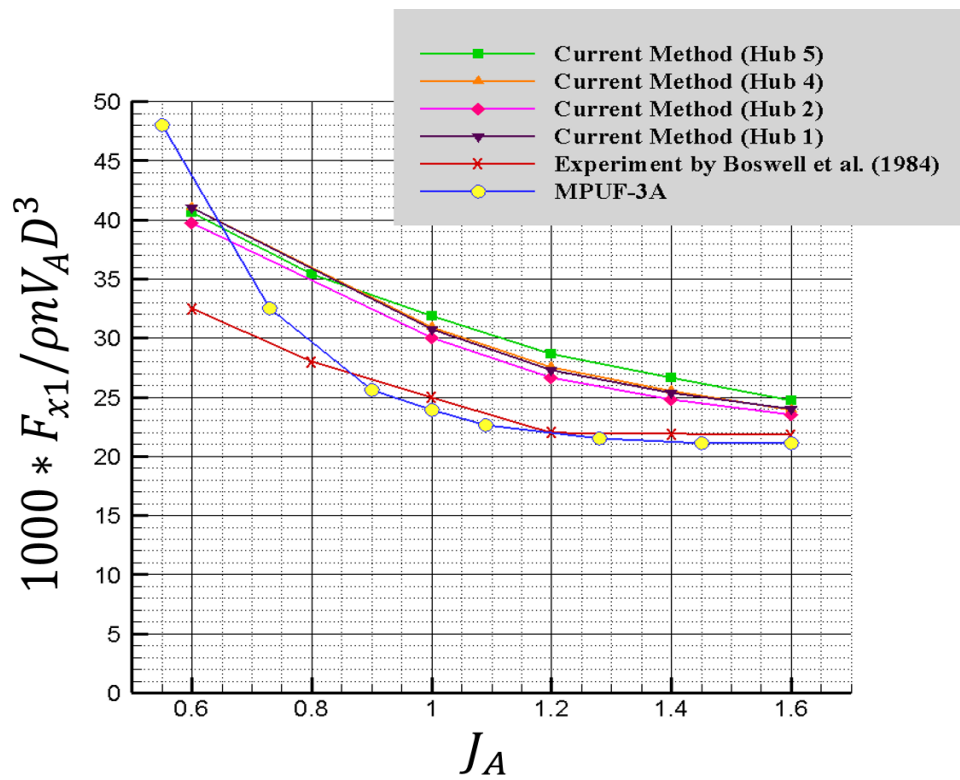


Figure 5.26 (Continued next page).

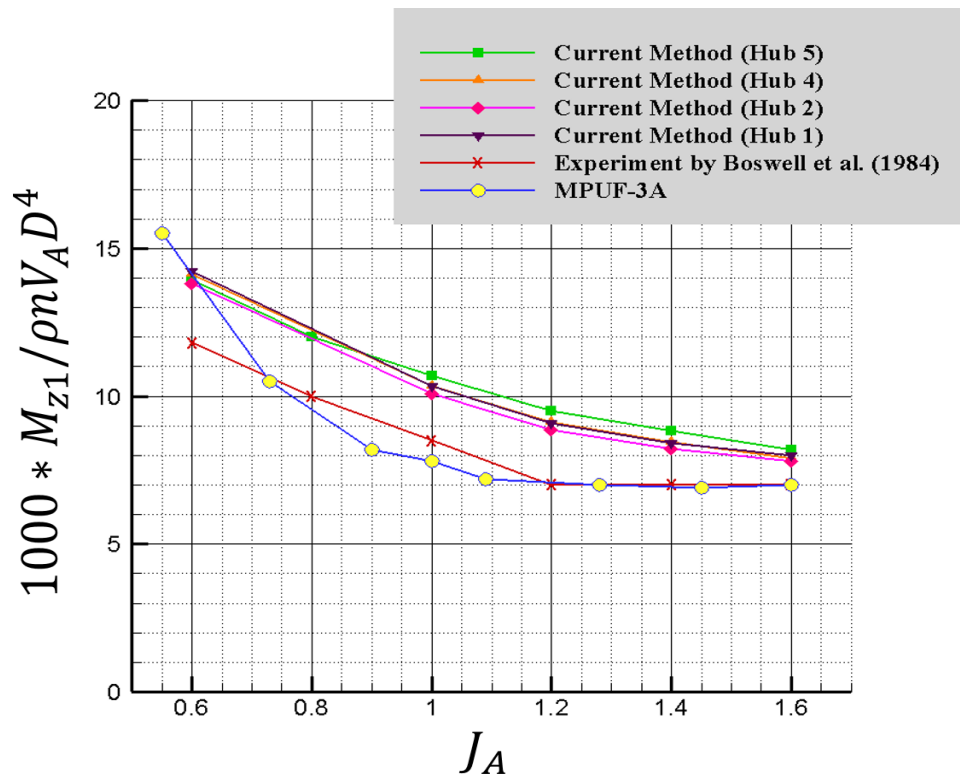
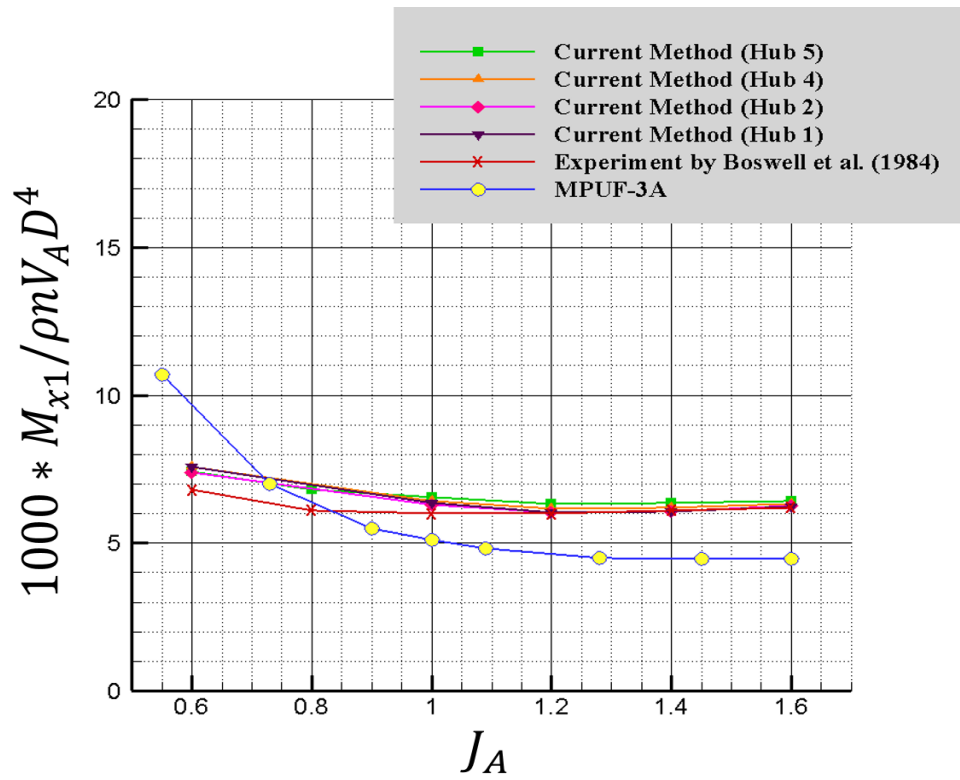


Figure 5.26 The first harmonic of the forces and moments acting on one blade for DTMB 4661 propeller.

Chapter 6

Conclusions and Recommendations

6.1 Conclusions

In this thesis, several improvements are made on the full wake alignment (FWA) scheme so that it can be applied to open and ducted propellers in steady and unsteady state. Since the alignment algorithm in FWA aligns the trailing vortices to the local velocity, one of the modifications was to allow for a general wake inflow. Based on that inflow, an iterative alignment algorithm is developed which uses the perturbation velocities to adjust the inflow wake. In addition, special treatments are introduced to the panels on the duct and duct wake.

The two repaneling options, i.e. Option 1 and Option 2 have been applied to a ducted propeller with square tip blade and a sharp trailing edge duct. It is shown that using the duct and duct wake panels which are adapted to the blade tip and its wake improves not only the accuracy but also the convergence rate of the results. The predicted force performance of a square tip ducted propeller with both repaneling options shows very good agreement with the experimental measurements. Especially, Option 2, which repeatedly adapts the duct panels to the blade wake shows stable convergence history even at the very lower advance ratio. Also, the panel matching between the blade tip and duct inner side enables FWA to produce reasonable and more accurate blade circulation toward the blade tip, compared to the case without panel matching.

For Option 2, control points on the duct panels should be readjusted such that the control points have the same radial locations of the control points on stretched panels. To this end, a special treatment is discussed to stretch the twisted panels. This helps Option 2 avoid singular behavior,

which comes from the close distance between the control point and the outer edge of the blade wake. As a result, the abnormally induced velocity on the blade wake is effectively avoided, and therefore the convergence of the panel method has been improved.

Considering that the duct wake is also a material surface, which has to flow along with the local flow, the duct wake is also aligned using FWA. By aligning the duct wake, the current panel method can represent the behavior of the trailing vorticity trajectory behind the duct trailing edge. To validate the predicted results from panel method, distribution of the trailing vorticity in downstream has been correlated with those from RANS simulations. That shows that not only the locations but also the curling behaviors of the wake are in very good agreement with the results from RANS except for the region where the wake diffuses downstream. The predicted performance from panel method with FWA applied on both the blade wake and the duct wake deviates from the experimental values at the high loading. However, when cylindrical duct wake is assumed to duct wake, panel method showed very good agreement with the experiments. What that tells us is that the over prediction of force performance might be attributed to the wake panels which cannot well represent high diffusion of shedding vortex at far downstream, remaining further investigation.

FWA is also applied to DTMB 4661 open propeller in steady and unsteady state. In steady state, convergence history of the panel method showed the predicted circulations on the blade are invariant to number of wake panels, and so are the predicted blade forces. It is also shown that FWA can handle the circumferentially averaged mean inflow. Convergence history of FWA shows that wake panels are fully aligned to the local flow in a progressive manner. Further validation is made by observing that the magnitude of cross product between the vortex segment and the total velocity approaches to zero, ideal state of the alignment.

In uniform flow, the predicted results from both the unsteady wake alignment scheme and steady wake alignment scheme are in good agreement. Distribution of the aligned wakes from the two schemes is also in good agreement, validating both schemes are consistent with each other in steady flow. For the inclined shaft flow, four different hub geometries are adopted to DTMB 4661 propeller to investigate the effects of hub geometry on the predicted propeller performance. It was found that the hub geometry does not cause significant difference on the predicted results. Wake panels for all hub cases seem to follow the local stream, which is inclined by 10° . The predicted thrust and torque on the blade also converged when enough panel numbers are assumed to represent the wakes. First harmonic amplitudes of the forces and moments predicted by panel method are somewhat over predicted compared to the experimental measurements especially the axial force and tangential moment. However, for the lower advance ratios, panel method predicts better correlations with the experiments than VLM.

6.2 Recommendations

For the future work, it is necessary to apply FWA to different propeller geometries, including ducted propellers with round tip blade, as well in the case of cavitating flow. Experimental data in steady state would be a good source of correlation with the panel method.

It is shown that the hub geometry does not bring a significant difference to the predicted propeller performance in unsteady state. However, the numerical problem might happen around the region where hub and wake panels intersect. In this thesis, if the aligned wakes fall inside the hub geometry, the wake panels are redistributed such that the radius of the wake is the same as the hub radius. In the real case, however, there might be significant interactions between the wake and hub, especially in the case of the inclined flow. In the cavitating case, the interaction might become

more significant due to the hub vortex cavitation which flows along with the local flow. This fact should be taken into consideration in FWA to better predict the behavior of shedding vortex in unsteady state.

For the duct wake alignment, although FWA can well represent the trailing vorticity near the trailing edge, when it comes to the region where wakes are truncated in downstream, both the blade wake and the duct wake are unnaturally entangled with each other. This numerical inaccuracy might be attributed to the diffusion, the natural behavior of trailing vorticity. Although FWA aligns the duct wake, and that prevents penetration of the blade wake on the duct wake, curling on both the wakes eventually causes them to penetrate with each other as their curling becomes bigger downstream. The fact that at lower advance ratio more curling is shown compared to the higher advance ratio is consistent with the results of the severe panel penetration at the lower advance ratio. This numerical issue needs to be overcome to better predict the distribution of wake sheets. The force predictions are also expected to be improved once this issue is resolved.

Additionally, the effects of viscosity on the propeller geometry must be examined more extensively, as described in the paper of [Kinnas et al. 2016]. Three-dimensional viscous/inviscid interactive method, introduced by [Yu 2012], [Purohit 2013], and [Kinnas et al. 2012] can be applied to the current panel method to evaluate the viscosity effect on the duct and the blade.

Bibliography

- [1] Hess, J. L. "Calculation of non-lifting potential flow about arbitrary three dimensional bodies." *Journal of Ship Research* 8, no. 2 (1964): 22-44.
- [2] Hess, John L., and Walte O. Valarezo. "Calculation of steady flow about propellers using a surface panel method." *Journal of Propulsion and Power* 1, no. 6 (1985): 470-476.
- [3] K. Koyama, A. Kakugawa, and M. Okamoto. "Experimental investigation of flow around a marine propeller and application of panel method to the propeller theory," In Sixteenth Symposium on Naval Hydrodynamics, (1986).
- [4] Lee, Jin-tae. "A potential based panel method for the analysis of marine propellers in steady flow." PhD diss., Massachusetts Institute of Technology, (1987).
- [5] Fan H. "An Improved Panel Method for the Prediction of Performance of Ducted Propellers." MS thesis, Ocean Engineering Group, CAEE Department, UT Austin, August, (2015) (also UT-OE Report 15-02).
- [6] S. A. Kinnas, Y. Su, W. Du, S. Kim. "A Viscous/Inviscid Interactive Method Applied to Ducted Propellers with Ducts of Sharp or Blunt Trailing Edge." In 31st Symposium on Naval Hydrodynamics, September (2016).
- [7] Kerwin, Justin E., and Chang-Sup Lee. Prediction of steady and unsteady marine propeller performance by numerical lifting-surface theory. No. Paper No. 8. (1978).
- [8] D.S Greely, and J. E. Kerwin. Numerical methods for propeller design and analysis in steady flow. *Trans. SNAME*, 90, (1982).
- [9] Kinnas, S., and S. Pyo. "Propeller wake alignment models in uniform and inclined inflow." In Propellers/Shafting'97 Symposium, Virginia Beach, VA. Soc. Naval Arch. & Marine Engrns. 1997.

- [10] Keenan, D. P. "Marine Propellers in Unsteady Flow." PhD diss., Massachusetts Institute of Technology, (1989).
- [11] Lee, H. "Modeling of Unsteady Wake Alignment and Developed Tip Vortex Cavitation." PhD diss., CAEE, UT Austin, (2002).
- [12] He, L. "Numerical Simulation of Unsteady Rotor/Stator Interaction and Application to Propeller/Rudder Combination." PhD diss., CAEE, UT Austin, (2010).
- [13] Tian, Ye and S. A. Kinnas. "A wake model for the prediction of propeller performance at low advance ratios." *International Journal of Rotating Machinery* (2012).
- [14] Yu, X. "Three dimensional viscous/inviscid interactive method and its application to propeller blades," Master thesis, CAEE, UT Austin, 2012.
- [15] Purohit, J. (2013), "An Improved Viscous-Inviscid Interactive Method and its Application to Ducted Propellers," Master thesis, CAEE, UT Austin, 2013.
- [16] Preliminary Documentation for PBD-10 Computer Program, MIT Department of Ocean Engineering, 1981.
- [17] Loukakis, Theodore A. A new theory for the wake of marine propellers. No. 71-1 DR Thesis. 1971.
- [18] Kinnas, S.A., Fan, H., Tian, Y., "A Panel Method with a Full Wake Alignment Model for the Prediction of the Performance of Ducted Propellers." *Journal of Ship Research*, Vol. 59, No. 4, 2015, pp. 246-257.
- [19] Baltazar, J., Rijpkema, D., Falcao de Campos, J. A. C., and Bosschers, J., "A comparison of panel method and RANS calculations for a ducted propeller system in open-water." *Proceedings of the 3rd International Symposium on Marine Propulsion*, Launceston, Tasmania, Australia, 2013.

- [20] Baltazar, J., Falcao de Campos, J. A. C., and Bosschers, J., "Potential Flow Modeling of Ducted Propellers with a Panel Method," Proceedings of the 4th International Symposium on Marine Propulsors, Austin, Texas, USA, 2015.
- [21] Tian. Y. and S. A. Kinnas., "Modeling of Leading Edge Vortex and its Effects on Propeller Performance." Proceedings of the Second International Symposium on Marine Propulsors, Hamburg, Germany, 2011.
- [22] S. A. Kinnas. And Hsin. C., "A boundary element method for the analysis of the unsteady flow around extreme propeller geometries." AIAA Journal, 30(3):688-696, 199).
- [23] Morino, Luigi, and Ching-Chiang Kuo. "Subsonic potential aerodynamics for complex configurations: a general theory." AIAA journal 12, no. 2 (1974): 191-197.
- [24] Bosschers, J., and R. van der Veecken., "Open water tests for propeller KA4-70 and duct 19A with a sharp trailing edge," MARIN Report 224457-2-VT (2008).
- [25] Boswell, R., Jessup, S., Kim, K., and Dahmer, D. Single-Blade Loads on Propellers in inclined and Axial Flows. Technical Report DTNSRDC-84/084, DTNSRC (1984).
- [26] Kinnas, S., Griffin, P., and Mueller, A., "Computational tools for the analysis and design of high speed propulsors." In the International CFD Conference, Ulsteinvik, Norwage (1997).
- [27] Mueller, A. and Kinnas, S. "Cavitation prediction using a panel method." In ASME Symposium on Marine Hydrodynamics and Ocean Engineering, volume 14, pages 127-137, Dallas, TX (1997).
- [28] Mueller, A., "Development of face and mid-chord cavitation models for the prediction of unsteady cavitation on a propeller." MS thesis, UT Austin, Dept. of Civil Engineering (1998).
- [29] Mueller, A. and Kinnas, S., "Propeller sheet cavitation predictions using a panel method." Journal of Fluids Engineering, 121:282-288 (1999).

- [30] Young, Y. and Kinnas, S., “Numerical and experimental validation of a cavitating propeller BEM code.” In Cavitation and Multiphase Flow Forum, San Fransisco, CA. 3rd ASME/JSME Joint Fluids Engineering Conference (1999b).
- [31] Young, Y. and Kinnas, S., “A BEM for the prediction of unsteady midchord face and/or back propeller cavitation.” Journal of Fluids Engineering, 123 (2001a).
- [32] Dynamic Positioning System (DPS). Digital image. Web 27 July 2017 <https://www.google.com/search?q=ducted+propeller+dps+system&source=lnms&tbm=isch&sa=X&ved=0ahUKEwiLhdL9zZbVAhVh6oMKHeJhCLsQ_AUIBygC&biw=1918&bih=984#tbm=isch&q=dynamic+positioning>
- [33] Ducted propeller with dynamic positioning system. Digital image. Web 27 July 2017 <https://www.google.com/search?q=ducted+propeller+dps+system&source=lnms&tbm=isch&sa=X&ved=0ahUKEwiLhdL9zZbVAhVh6oMKHeJhCLsQ_AUIBygC&biw=1918&bih=984#tbm=isch&q=dynamic+positioning (2)>
- [34] Kinnas, S. “BOUNDARY ELEMENT METHODS.” UT-Austin, Austin. Fall 2016. Lecture Notes.
- [35] Lee, H. S. and Kinnas, S. A., “Application of boundary element method in the prediction of unsteady blade sheet and developed tip vortex cavitation on marine propellers.” Journal of Ship Research, 48(1):15-30 (2004a).
- [36] Lee, H. S. and Kinnas, S. A., “Unsteady wake alignment for propellers in nonaxisymmetric flows.” Journal of Ship Research, 49(3) (2005b).
- [37] S. H. Chang and Kinnas, S. A., “Numerical simulation of Wetted and Cavitating Flows inside Water-jets.” 29th Symposium on Naval Hydrodynamics, Gothenburg, Sweden, August (2012).

[38] Kinnas S. A., Yu, X. and Tian, Y., “Prediction of Propeller Performance under High Loading Conditions with Viscous/Inviscid Interaction and a New Wake Alignment Model.” 29th Symposium on Naval Hydrodynamics, Gothenburg, Sweden, August (2012).

Vita

Seungnam Kim was born in Ulsan, South Korea in 1990. He received the Bachelor of Science degree at the department of Naval Architecture & Ocean Engineering from University of Ulsan in Feb, 2015. He also received the Bachelor of Business Administration from the same university in Feb, 2015. In August 2015, he started his graduate studies as a member of the Ocean Engineering Group at The University of Texas at Austin. At the same time, he started his lifelong drama of becoming a global leader in the shipbuilding & offshore industry with professor Spyros A. Kinnas.

E-mail address: naoestar@utexas.edu | naoestars@gmail.com

This manuscript was typed by Seungnam Kim.